NASA CR-134670
EDD W-06553

STUDY OF 42 AND 85 GHz COUPLED CAVITY TRAVELING-WAVE TUBES FOR SPACE USE

by

J. B. Kennedy, I. Tammaru, and P. S. Wolcott

HUGHES AIRCRAFT COMPANY

Electron Dynamics Division

Prepared for

NATIONAL AERONAUTICS AND SPACE ADMINISTI

NASA Lewis Research Center
Contract NAS 3-19701

Page Intentionally Left Blank

1. Report No.	2. Government Accession No.	3. Recipient's Catalog No.
NASA CR-		

4. Title and Subtitle	5. Report Date
STUDY OF 42 AND 85 GHz COUPLED CAVITY TRAVELING-WAVE TUBES FOR SPACE USE	June 1977
	6. Performing Organization Code

7. Author(s)	8. Performing Organization Report No.
J. B. Kennedy, I. Tammaru, and P. S. Wolcott	W-06553
	10. Work Unit No.

9. Performing Organization Name and Address	11. Contract or Grant No.
Hughes Aircraft Company Electron Dynamics Division Torrance, California 90509	NAS 3-19701
	13. Type of Report and Period Covered
12. Sponsoring Agency Name and Address	Contractor Report
National Aeronautics and Space Administration Washington, D. C. 20546	14. Sponsoring Agency Code

15. Supplementary Notes

Project Manager, D. J. Connolly, NASA Lewis Research Center, Cleveland, Ohio

16. Abstract

Designs were formulated for four CW, millimeter wavelength traveling-wave tubes having high efficiency and long life. Three of these tubes, in the 42 to 44 GHz frequency region, develop power outputs of 100 to 300 watts with overall efficiencies of typically 45 percent. Another tube, which covers the frequency range of 84 to 86 GHz, provides a power output of 200 watts at 25 percent efficiency. The cathode current density in each design was $1 A/cm^2$. Each tube includes: metal-ceramic construction, periodic permanent magnet focusing, a two step velocity taper, an electron beam refocusing section, and a radiation cooled three-stage depressed collector. The electrical and mechanical design for each tube type is discussed in detail. The results of thermal and mechanical analyses are presented.

17. Key Words (Suggested by Author(s))		18. Distribution Statement
Millimeter Wavelength Traveling-Wave Tubes High Efficiency Beam Refocusing	Multi-stage collector, Radiation Cooling	Unclassified - unlimited

19. Security Classif. (of this report)	20. Security Classif. (of this page)	21. No. of Pages	22. Price*
Unclassified	Unclassified	175	

NASA-C-168 (Rev. 10-75)

Page Intentionally Left Blank

FOREWORD

The work described in this report was conducted by the Electron Dynamics Division of Hughes Aircraft Company, under NASA Contract NAS3-19701 with Dr. D. J. Connolly, NASA Lewis Research Center, as project manager. The project manager at Hughes was J. B. Kennedy and the principal contributors were Dr. I. Tammaru and P. S. Wolcott.

Page Intentionally Left Blank

TABLE OF CONTENTS

TABLE OF CONTENTS (CONT'D)

LIST OF ILLUSTRATIONS

LIST OF ILLUSTRATIONS (CONTINUED)

LIST OF ILLUSTRATIONS (CONTINUED)

LIST OF ILLUSTRATIONS (CONTINUED)

LIST OF ILLUSTRATIONS (CONTINUED)

LIST OF ILLUSTRATIONS (CONTINUED)

LIST OF TABLES

Page Intentionally Left Blank

1.0 SUMMARY

This final report describes a study program which culminated in the design of four millimeter wavelength traveling-wave tubes (TWTs). The 942H is a 150 W TWT covering the frequency range of 41.0 to 43.0 GHz; the 943H, 300 W, also 41.0 to 43.0 GHz; the 944H, 100 W over the frequency range 42.0 to 42.5 GHz; and the 985H, 200 W, 84.0 to 86 GHz. All TWTs included a diode electron gun with an impregnated cathode, a three section coupled cavity circuit with a two step velocity taper, periodic permanent magnet (PPM) focusing, an electron beam refocusing section, a radiation cooled three-stage depressed collector, and a package compatible with space environment.

This program, as defined by Contract NAS3-19701, was initially for three TWTs, the 942H, 943H, and the 985H; however, it was later amended to include the 944H. At the beginning of the program, effort was directed towards a definition of important circuit design parameters and dimensions (e.g., cathode voltage, electron gun perveance, beam aperture diameter, etc.). This required approximately one month and enabled the initiation of electron gun design early in the program.

The preliminary circuit designs were extensively analyzed with large signal and small signal computer programs. The analyses resulted in a comprehensive definition of the TWT circuits. Circuit parts, including coupled cavities, RF transformers and terminations, all scaled for C-band, were procured and experimental procedures were initiated. These included:

- Optimization of bandwidth and frequency centering of the ω vs β characteristic for each circuit.

- Test of RF input (output) stepped transformers.

- Simulation and test of the input and output circuit section of each TWT, typically a stepped transformer, hybrid cavity, coupled cavities and RF termination.

Design of the RF input-output window was accomplished by means of an available computer program. The window consists of a half wavelength (thick) ceramic block with irises at either extremity. This kind of window has been used on several millimeter wavelength TWTs at Hughes. Past experience has shown that tests of scaled models are not required.

Electron gun design, started early in the program, entailed different configurations for each tube type. This effort followed a design procedure which has been employed at Hughes for the guns of several successful millimeter wavelength TWTs. This procedure employs an analog electrolytic tank model and several related computer programs.

The periodic permanent magnet (PPM) focusing array design was started early in the program and proceeded in coincidence with the circuit and electron gun design effort. This was necessary because of the mutual dependence of focusing array dimensions and circuit dimensions. A computer program which calculates statistical beam radii as a function of axial distance from the cathode was the principal tool for the focusing array design.

The multi-stage depressed collectors were a major task of the study program. Available computer programs were used for this design. These predict the spent beam energy distribution and the electron trajectories in the collector. The collector design investigations began after the initial circuit and focusing designs were complete and continued throughout the program.

The thermal analysis was principally concerned with the multi-stage depressed collectors. A multi-nodal thermal model was developed for each TWT collector and an available thermal computer program was used for analysis.

Mechanical design of the TWTs began after preliminary dimensions for circuit, electron gun, and collector were established. The design effort first concerned the vacuum envelope; later a package design for each TWT was formulated. Shock and vibration capability was an on-going consideration. Special attention was given to the multi-stage, radiation cooled collectors. Critical assemblies and details were drawn and will be supplied as specified in Contract NAS3-19701.

Page Intentionally Left Blank

2.0 INTRODUCTION

The purpose of the contract effort described in this report was to design four millimeter wavelength TWTs. These tubes were designated 942H, 943H, 944H, and 985H. The principal specifications are summarized in Table 2-1.

In recent years the Electron Dynamics Division (EDD) of Hughes Aircraft Company has been deeply involved in design, development and fabrication of millimeter wavelength TWTs. One of these tubes provides 100 watts RF power output at a minimum efficiency of 34% over a substantial bandwidth in W-band. This device features a velocity tapered coupled cavity circuit and a multi-stage depressed collector. Another similar 50 watt device has been produced in quantity and is space qualified. The experience gained in these and other similar development programs has been applied to the design of the 942H, 943H, 944H, and 985H.

Coupled cavity circuits constrained by the requirement for periodic permanent magnet (PPM) focusing were designed by employing Hughes large signal and small signal computer programs, used in conjunction with RF measurements of scaled coupled cavity circuit models. For each TWT several iterations were required before a suitable design was formulated.

An electron gun for each TWT was designed. These guns are convergent spherial diodes with cathode current density (1.0 amp per square centimeter) which is compatible with long life. The electron guns are of the low perveance type subject to the defocusing effects of transverse thermal electron velocities. Hughes has a very reliable procedure for designing this kind of electron gun. A related computer program accurately evaluates the quality of its focused electron beam.

TABLE 2-1

TWT SPECIFICATIONS

TUBE DESIGNATION	942H	943H	944H	985H
Center Freq. (GHZ)	42.0	42.0	42.25	85.0
Freq. Band (GHZ)	2.0	2.0	.5	2.0
Power Output (W)	100	200	100	200
Gain (dB)	44.0	47.0	44.0	47.0
Gain Variation (dB)	±1.0	±1.0	±1.0	±1.0
Noise Figure (dB)	40.0	40.0	40.0	40.0
General Requirements:	PPM Focusing Velocity Resynchronization Multistage Depressed Collector 25 kV Max Cathode Voltage Stable Into Load VSWR of 1.25:1 2 Years Minimum Life Suitable for Space Application			

Another important task was to insure that a smooth (low reflectance) transition would be provided from input or output wave guide port into the terminated coupled cavity circuit. This was accomplished by fabricating scaled circuit section models which were reflectance tested and empirically adjusted until a low reflectance impedance transition was achieved. A typical input circuit section consisted of the following scaled components: stepped transformer; hybrid transition cavity; ten standard circuit section cavities and circuit termination. An output circuit section included, in addition, special circuit sections which simulated the two-step velocity taper.

Metal-ceramic RF window designs were formulated for the TWTs. These windows are of the "half wavelength block" type, and are designed by

means of a Hughes computer program. Past experience has shown that scaled RF tests are unnecessary since the computer predicted dimensions are reliable.

All TWTs included multi-stage depressed collectors (MDCs) preceded by refocusing sections. Hughes participated in past programs with NASA Lewis which were directly concerned with spent beam refocusing and MDCs. The experience gained in these programs was useful in providing suitable designs for the 942H, 943H, 944H, and 985H.

Mechanical designs were formulated for each TWT and key drawings have been completed. Approximately seventy-five drawings in total were made and reproductions will be forwarded to NASA Lewis. An extensive thermal analysis of the collector region was conducted. This analysis was multi-nodal and was concerned with a number of different operating modes and combinations of modes, e.g., full sun, no sun, full RF drive, no RF drive, .7 screening fraction, .5 screening fraction etc.

In addition, a mechanical analysis of important assemblies was conducted to determine the effects of stress due to thermal cycling and due to vibration.

The purpose of this report is to describe in detail the design, analyses and tests just cited.

Page Intentionally Left Blank

3.0 ELECTRICAL DESIGN

A principal objective for the traveling-wave tube designs under consideration was high efficiency. The methods used for achieving high efficiency included multistage depressed collectors and RF circuits with a phase velocity taper.

In the present type of devices a multi-stage collector improves the overall efficiency very significantly. The study indicates that a triple-depressed collector increases the efficiency by a factor of about three in the 42 GHz tubes, and by as much as five in the 85 GHz tube. The velocity taper technique is similarly very effective. It improves the basic interaction efficiency by nearly a factor of two over that obtainable in a tube with a uniform RF circuit.

For high basic efficiency it is also desirable to have a high intrinsic interaction strength between the RF wave and the electron beam. The first part of the design study was consequently devoted to selecting the operating parameters for maximum interaction strength consistent with other requirements and constraints.

3.1 PARAMETER SELECTION

In the present TWT designs at mm wavelengths a preimary constraint was beam focusing, to be accomplished by periodic permanent magnets. After defining acceptable focusing criteria, the initial task was to establish the operating voltage for highest interaction strength.

3.1.1 Interaction Strength Versus Focusing Constraint

A quantitative measure of the effective interaction strength is Pierce's growth parameter C given by

$$C = \left(\frac{KI_o}{4V_o}\right)^{1/3} \tag{1}$$

where

K = Pierce's interaction impedance

I_o = beam current

V_o = beam voltage

In PPM focusing both the magnitude of the magnetic field and its period determine the dynamics of the focused beam. The magnetic field, B, required to focus an electron beam from a gun, with thermal velocity effects included, has been derived by Herrmann:[1]

$$B^2 = B_b^2 + \frac{8kT_c}{m\eta^2}\left(\frac{r_c^2}{r_o^4}\right) + \left(\frac{B_c r_c^2}{r_o^2}\right)^2 \tag{2}$$

where

$$B_b^2 = \frac{2I_o}{\pi\varepsilon_o \eta u_o}\left(\frac{1}{r_o^2}\right)$$

$$\eta = \frac{e}{m}$$

Here e and m are the electronic charge and mass respectively, ε_o is the permittivity of free space, and k is the Boltzmann constant. The electron beam is described by the total current I_o, the electron

velocity u_o, and a certain statistical rms beam radius r_o defined by Herrmann. The beam starting conditions are specified by the cathode temperature T_c (in degrees Kelvin), the cathode (disk) radius r_c, and the axial field at the cathode, B_c. For a PPM system the field magnitude B in eq. (2) is to be identified with the root-mean-square value.

Comparing the expression for the interaction strength parameter C with the "Brillouin" part, B_b, of the magnetic field, it is evident that the conditions that provide a large C (high current, low voltage) require a strong focusing field. A high interaction impedance K can be obtained with a small beam hole and this again necessitates a strong focusing field. Thus the interaction strength is limited by the magnetic field that can be achieved. It is also seen that the required focusing field goes up with increased cathode size, increased cathode flux, and higher cathode temperature.

The beam stability in a PPM focusing field involves the relation between the oscillation wavelength of the radial motion in the beam and the period of the magnetic field. With a highly thermal low perveance beam, an appropriate oscillation wavelength is that associated with the small-amplitude ripple in r_o given by the angular frequency[1]

$$\omega_R = \omega_c \sqrt{1 - \frac{1}{2} (B_b/B)^2} \qquad (3)$$

where

$$\omega_c = \eta B = \text{the cyclotron frequency.}$$

The scallop wavelength is therefore

$$\lambda_s = \frac{u_o}{(\omega_R/2\pi)} = \frac{2\pi u_o}{\omega_c \sqrt{1 - \frac{1}{2}(B_b/B)^2}} \qquad (4)$$

If λ_s is large relative to the magnetic field period L the beam will effectively experience an average constant focusing field of magnitude B. As λ_s becomes more comparable to L, the electron motion is more affected by the local changes in the field.

When λ_s equals L an unstable beam generally results. To provide good focusing it is therefore necessary to ensure some minimum value of the ratio λ_s/L. Based on prior experience with low perveance thermal electron beams this ratio was chosen as 1.2 in the present study. Since λ_s is approximately inversely proportional to B, a large C (which requires a large B) will give a small λ_s. The condition $\lambda_s/L \geq 1.2$ thus provides a further constraint on the interaction strength that can be obtained.

3.1.2 General Assumptions

The following general assumptions were made in the study:

1. The PPM structure was external to the vacuum envelope. The magnetic and electrical periods were therefore independent.

2. Samarium Cobalt magnet material was used for maximum field capability.

3. The maximum pole piece field allowed was 1.3 tesla to avoid possible saturation effects.

4. The cathode loading was chosen at 1 A/cm^2 for long life.

5. The cathode material was to be impregnated tungsten, with an approximate operating temperature of 1400° K.

6. The focusing design assumed no magnetic cathode flux, $B_c = 0$, since the available magnetic field was a constraint.

7. The ratio of scallop wavelength to magnetic period, λ_s/L, was taken to be 1.2 minimum, as discussed in the preceding section.

8. The beam hole size, 2a, was chosen to transmit (typically) 99.5 percent of the theoretical DC beam. Thus

$$a = r_{99.5,\ max}$$

where $r_{99.5,\ max}$ is the maximum value of the radius that encloses 99.5 percent of the current in the focused thermal DC beam. With no cathode flux, the rms radius r_o is 0.42 of $r_{99.5,\ max}$.[2] Although the concept of a quantitative beam filling factor, b/a, is generally unsatisfactory for a thermal beam, a value of b/a = 0.42 was used in the RF calculations.

3.1.3 Outline of Design Procedure

The general design procedure is outlined as follows:

1. An initial basic tube efficiency is assumed, and the smallest practical ferrule hole size in the PPM stack is estimated.

2. The obtainable magnetic field as a function of magnetic period is evaluated. Using this function and the known DC beam power, relevant properties of the focused thermal beam ($r_{99.5}$, λ_s, and λ_s/L) can be calculated versus the rms focusing field for different beam voltages. The data can be displayed as beam hole radius versus beam voltage at a given λ_s/L. Equivalently, the beam hole size can be expressed in terms of the radial propagation parameter γa, once an appropriate ratio between the beam velocity and the circuit phase velocity at the design center frequency has been chosen.

3. The cavity dimensions and interaction impedance can now be computed for any beam voltage by making some additional assumptions regarding the cold passband characteristics and the cavity geometry. These assumptions concern the cold bandwidth, phase shift per cavity at center frequency, the detailed shape of the frequency vs phase curve, the gap to period ratio, the tunnel wall and web thicknesses, and the coupling hole size. The resulting cavity diameter is checked for compatibility with the assumed magnetic ferrule hole size in Step 1.

4. Knowing the value of Pierce's interaction impedance (averaged over the beam area, assuming $b/a = 0.42$), the variation of Pierce's C parameter with voltage is derived. The operating voltage is chosen to maximize C for highest interaction strength. At this point all the information necessary to start the detailed electron gun design has also been generated in the process.

5. The small signal gain bandwidth is calculated and the cold passband adjusted if necessary (Step 3). Such an adjustment will generally change the magnitude of the C parameter, but,

apart from a constant factor, the variation with voltage will very nearly remain the same.

6. Large signal analysis is performed with various velocity taper configurations in the RF circuit to achieve a high interaction efficiency over the frequency band. If the minimum efficiency differs appreciably from the one assumed in Step 1, another iteration of the design procedure should be made. In practice, no further iterations were made because of the time and effort involved. For this reason the predicted output power of two of the 42 GHz tubes remained 50 percent higher than the objective.

3.1.4 Selection of Operating Voltage

The selection of operating voltage as outlined in the previous section will now be described in greater detail using the 200 W design at 42 GHz, the 943H, as an illustrative example.

In Figure 3-1 are plots of the peak magnetic field that is attainable with Cobalt Samarium magnets as a function of the magnetic period for selected ferrule hole dimensions. The smallest hole size, 0.432 cm, is for the 85 GHz tube, while a dimension of 0.6 - 0.7 cm is appropriate for the 42 GHz designs. A numerical analysis* showed that under the

*The analysis was made by adjusting the pole piece thickness, while utilizing the highest practical coercive force for the magnet material, until the maximum field in the pole piece was approximately 1.3 tesla. Referring to Figure 3-24, the maximum field occurs at radius R_3. In changing the thickness W, the ferrule thickness was also changed such that $R_2 - R_1 = W/2$, while the clearance between R_3 and R_2 was kept at 0025 cm (0.001 inch). Under these conditions, a unique value of rms field is associated with any gap-to-period ratio, for a fixed period, ferrule hole size and magnetic material.

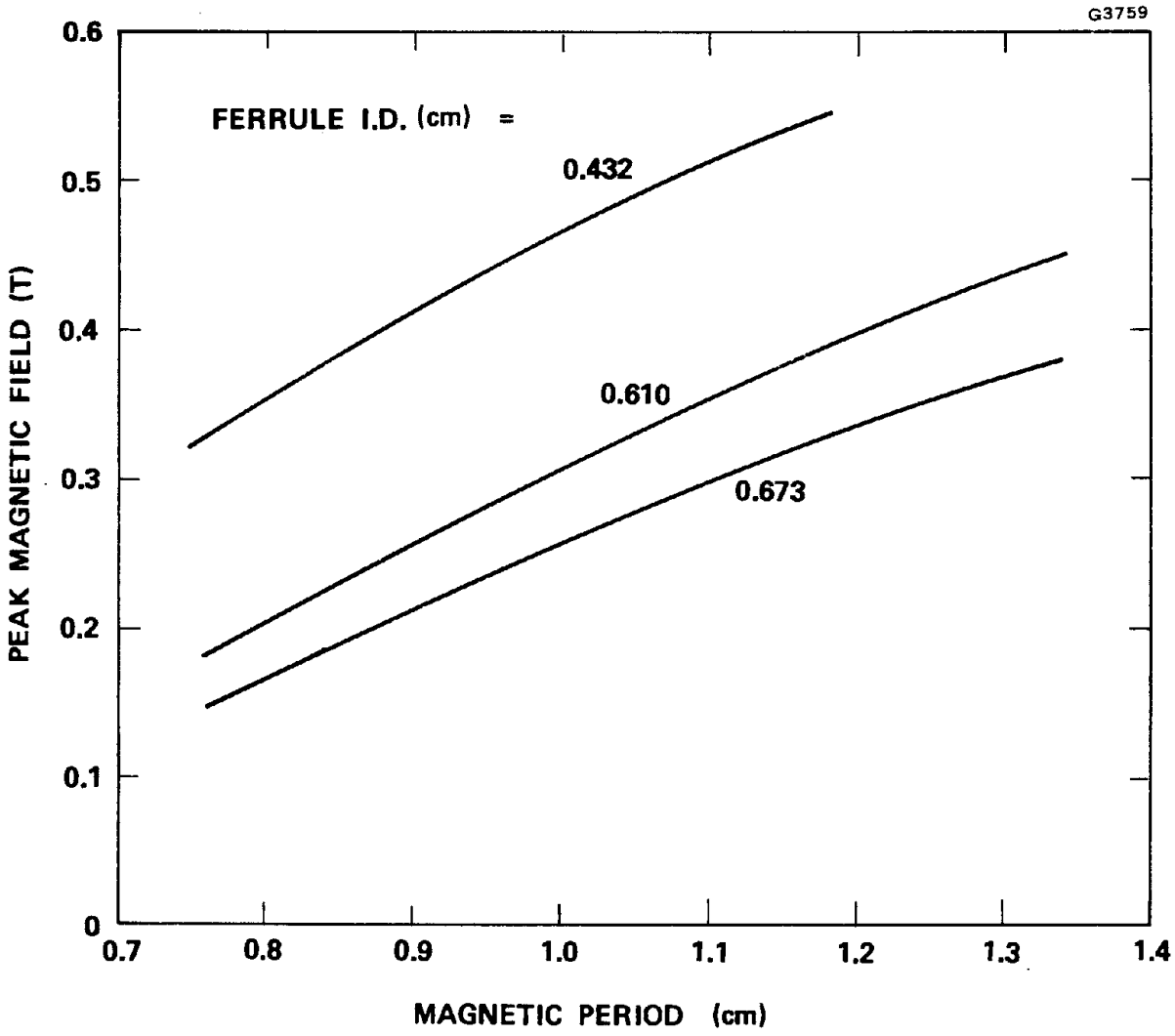

Figure 3-1 Magnetic field vs period for some ferrule hole dimensions.

constraint of a constant maximum pole piece flux the highest rms field on the axis was obtained with a gap to period ratio in the neighborhood of one third. For such a design the field is nearly sinusoidal with very little third harmonic content. The rms and peak fields are therefore approximately related by the factor $\sqrt{2}$.

Figures 3-2 and 3-3 display the beam hole diameter and the scallop wavelength to magnetic period ratio versus the rms magnetic field for beam voltages of 16, 19, and 22 kV. In these calculations a beam power of 2.0 kW was assumed, corresponding to a minimum basic efficiency of 10 percent. In evaluating λ_s/L, the curve for a ferrule I.D. of 0.61 cm in Figure 3-1 was used to relate the magnetic field to the period. From the data in Figures 3-2 and 3-3 the beam hole size can be plotted in terms of voltage at a given value of λ_s/L. Alternatively, the beam hole size can be expressed as the radial propagation parameter at center frequency for any voltage as in Figure 3-4. Here it has been assumed that the ratio of electron velocity to RF wave phase velocity, u_o/v_{ph}, is 1.04 at 42 GHz.

An initial passband design of 35 percent cold bandwidth and a phase shift per cavity of 1.35π at center frequency was selected for the 943H. The cavity configuration and impedance characteristics were then evaluated. The resulting C parameter, for the case $\lambda_s/L = 1.20$, is shown as a function of voltage in Figure 3-5. From this curve an operating voltage of 21 kV was chosen, with $\gamma a = 1.05$. The C parameter changes relatively little over a fairly large voltage range only because the γa parameter is reduced as the voltage goes up, providing increased interaction impedance.

A similar procedure was carried out for the other tube designs. An initial basic efficiency of 9 percent was assumed for the 942H. The best operating voltage for this tube was 17 kV. At the time the design

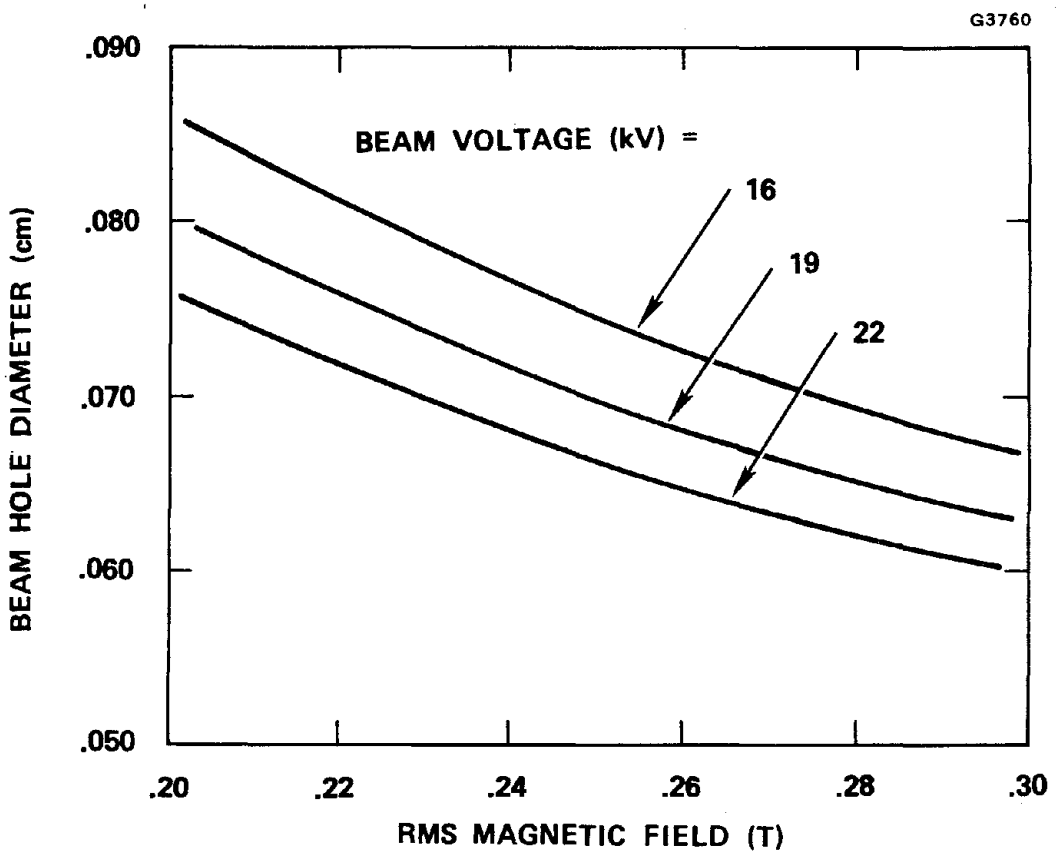

Figure 3-2 Beam hole diameter vs magnetic field for the 943H with different beam voltages.

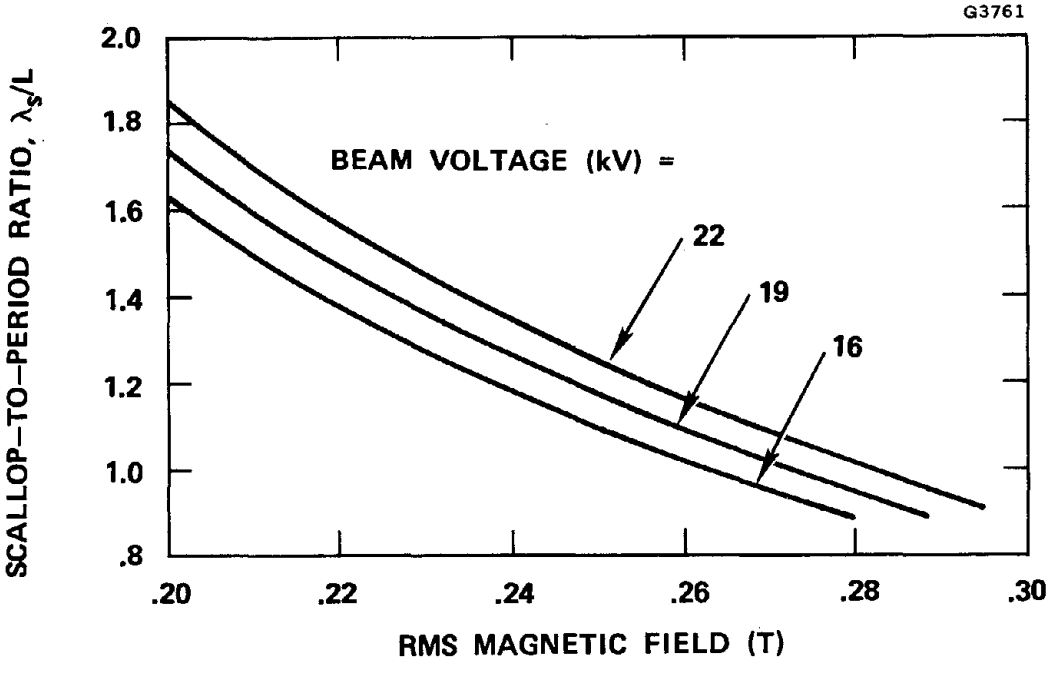

Figure 3-3 Ratio of scallop wavelength to magnetic period vs magnetic field for the 943H with different beam voltages.

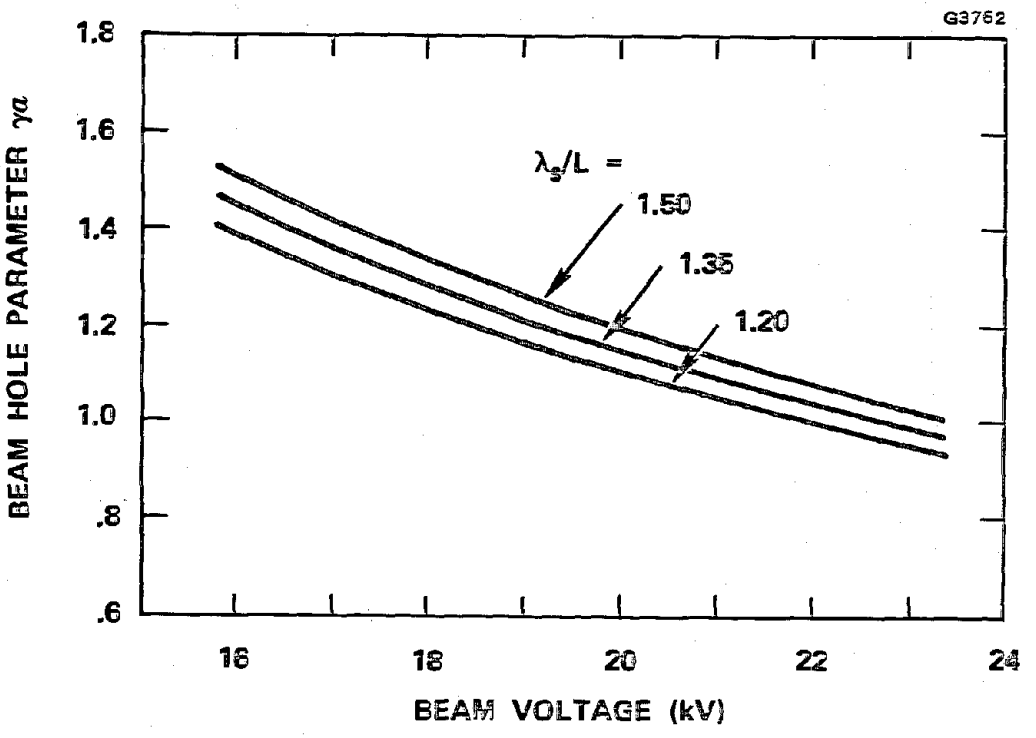

Figure 3-4 Radial propagation parameter γa vs beam voltage for the 943H at different values of λ_s/L.

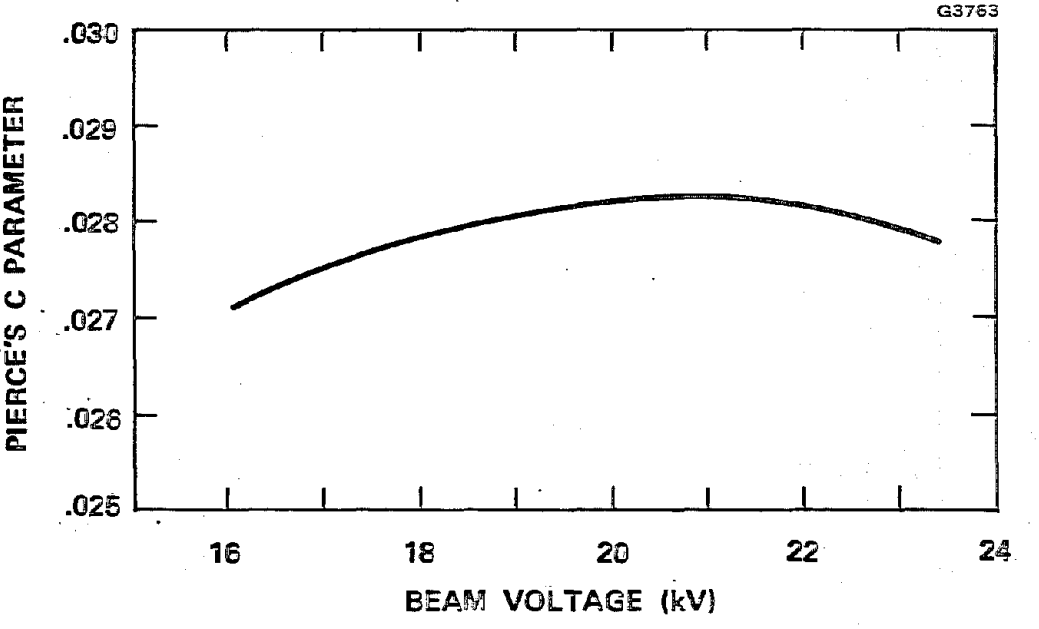

Figure 3-5 Pierce's growth parameter C vs beam voltage for the initial design of the 943H at $\lambda_s/L = 1.2$.

of the 944H was started, large signal calculations had already been made on the 942H and 943H which indicated that the basic efficiency was about 50 percent higher than estimated. The basic efficiency of the 944H was therefore assumed to be 17 percent initially, which was subsequently revised to 15 percent. The final operating voltage was 14.5 kV. The various designs that were investigated are described in the next section.

For the 985H a basic efficiency of 5 percent was assumed. The focusing constraint resulted in substantially larger γa values for this design than for the 42 GHz tubes. At 25 kV, which was the maximum allowed voltage in the design study, the required γa was 1.96. The calculated C parameter was still slowly increasing with voltage, being 4 percent larger at 30 kV than at 25 kV. However, the circuit properties for this tube were rather uncertain at the beginning of the design study, particularly the exact shape of the frequency vs phase ($\omega\beta$) curve which is needed for the impedance calculation. The shape is dependent on the cold bandwidth limit occurring when the cavity and slot modes merge. Since the maximum cold bandwidth generally decreases with increasing voltage, the uncertainty of the initial impedance evaluations were greater at the higher voltages.

Table 3-1 summarizes the basic design parameters of the four tubes, giving both the initially assumed passband characteristics and the final design values. The latter correspond to measured circuit properties established by cold tests at C-band frequencies (Appendix A). The parameters were selected by RF performance calculations that are further described in the next section.

The actual design of the PPM focusing stack, as derived for the beam parameters given in Table 3-1, and the associated gun parameters, is detailed in Figure 3-24 of Section 3.3. The final values of the required focusing field were established in the gun design process.

TABLE 3-1

SUMMARY OF BASIC DESIGN PARAMETERS

Tube	942H	943H	944H	985H
Design Objectives:				
Center Frequency, f_o (GHz)	42	42	42.25	85
Output Power (W)	100	200	100	200
Bandwidth (GHz)	2	2	0.5	2
Design Parameters:				
Assumed Min. Eff. (%)	9	10	15	5
Beam Voltage, V_o (kV)	17	21	14.5	25
Beam Current, I_o (mA)	65.4	95.2	46.0	160
Beam Perveance ($\mu A/V^{3/2}$)	0.0295	0.0313	0.0263	0.0405
Beam Hole Diam., 2a (cm)	0.0630	0.0660	0.0600	0.0676
γa	1.11	1.05	1.15	1.96
u_o/v_{ph}	1.04	1.04	1.04	1.03
Initial Passband Design:				
Phase Shift/Cavity (rad)	1.35π	1.35π	1.35π	1.35π
Cold Bandwidth (%)	35	35	18	30
Final Passband Design:				
Phase Shift/Cavity (rad)	1.40π	1.37π	1.25π	1.42π
Cold Bandwidth (%)	35.6	36.2	27.2	31.4
Pierce's Impedance, K (Ω)	13.2	15.6	25.7	3.78
Pierce's C Parameter	0.0233	0.0261	0.0268	0.0182

3.2 CIRCUIT DESIGN

With the beam parameters determined the next step was to establish the cold bandwidth of the circuit and the appropriate phase shift per cavity at center frequency. This was accomplished through evaluation of the effective performance bandwidth by small signal calculations, from which the approximate number of standard circuit cavities was also found. The final step was the design of the velocity taper for high interaction efficiency by large signal analysis.

3.2.1 Passband Design by Small Signal Gain Calculations

A small signal gain computer program was used that accurately models the RF characteristics of the coupled cavity circuit interacting with a one-dimensional representation of the electron beam. The actual RF field shape in each gap is employed and the backward wave is included. For the purpose of establishing the performance bandwidth of a given circuit, perfect hot matches were generally assumed so that the fundamental interaction characteristics would not be obscured by gain ripple with frequency.

Calculations were made on three-section circuits with a total gain of about 50 dB. The results for the initial and final passband designs are summarized in Table 3-2 for all four tubes. A cold bandwidth of 35 percent and a phase shift per cavity of 1.35 π at center frequency was initially assumed for both the 942H and 943H. The 3 dB bandwidth, at a total gain level of 53 dB, was less than the specified operating bandwidth of 2 GHz. To increase the bandwidth in these tubes the approach was to go to a larger phase shift per cavity leaving the bandwidth the same. In the final designs the calculated 3 dB bandwidth, based on measured circuit data, was about 3 GHz. With a gain per

TABLE 3-2

SMALL SIGNAL GAIN (SSG) CALCULATIONS OF
INITIAL AND FINAL PASSBAND DESIGNS

TUBE	942H	943H	944H	985H
Initial Design:				
Phase Shift (rad)	1.35π	1.35π	1.35π	1.35π
Cold Bandwidth (%)	35	35	18	30
Calculated SSG from Estimated Ckt Data:				
Gain, 3 Sections (dB)	53	53	50	50
3dB Bandwidth (GHz)	1.4	1.9	.74	1.3
Final Design:				
Phase Shift (rad)	1.40π	1.37π	1.25π	1.42π
Cold Bandwidth (%)	35.6	36.2	27.2	31.4
Calculated SSG from Measured Ckt Data:				
Gain, 3 Sections (dB)	51	53	50	51
3dB Bandwidth (GHz)	3.2	2.7	.95	1.5
No. of Cavities	112	104	103	172
Gain/Cavity at f_o (dB)	.61	.68	.68	.41

cavity between 0.6 and 0.7, approximately a hundred cavities were required. The final $\omega\beta$ diagrams of all three 42 GHz tubes are displayed in Figure 3-6.

The design of the 944H benefited from the results of the 942H and 943H analyses. Five different circuits were still investigated for this tube because of special considerations. The characteristics of these designs are summarized in Table 3-3. In designs A and B the phase shift per cavity was chosen at 1.35 π while the cold bandwidth was 18 percent to provide a hot bandwidth of at least 0.5 GHz (1.2 percent). The basic efficiency was first assumed to be 17 percent, in design A, but revised to 15 percent in design B. This change resulted from a consideration of the calculated C parameter (Figure 3-7) in comparison with the value used in the final design of the 943H, while also taking into account the increased loss of the narrower-band 944H. As is seen from Figure 3-7, the increased beam power in case B shifts the maximum value of the C parameter up, and also toward a higher operating voltage.

The cavity resonance frequency in designs A and B was 48 GHz, compared to 54 GHz in the other two 42 GHz tubes. This necessitated a larger cavity diameter and consequently a larger ferrule hole size of the magnetic circuit (0.673 vs 0.610 cm). From Figure 3-1 it is evident that the available magnetic field is almost 20 percent lower at the same period. It was of interest to consider a circuit design for the 944H with the higher cavity resonance, and consequently wider bandwidth, for which more magnetic field was available. Because design B already had adequate bandwidth performance (a 3 dB bandwidth of 0.74 GHz), the phase shift at midband of design C was lowered to 1.25 π to benefit from a higher interaction impedance. The resulting Pierce's

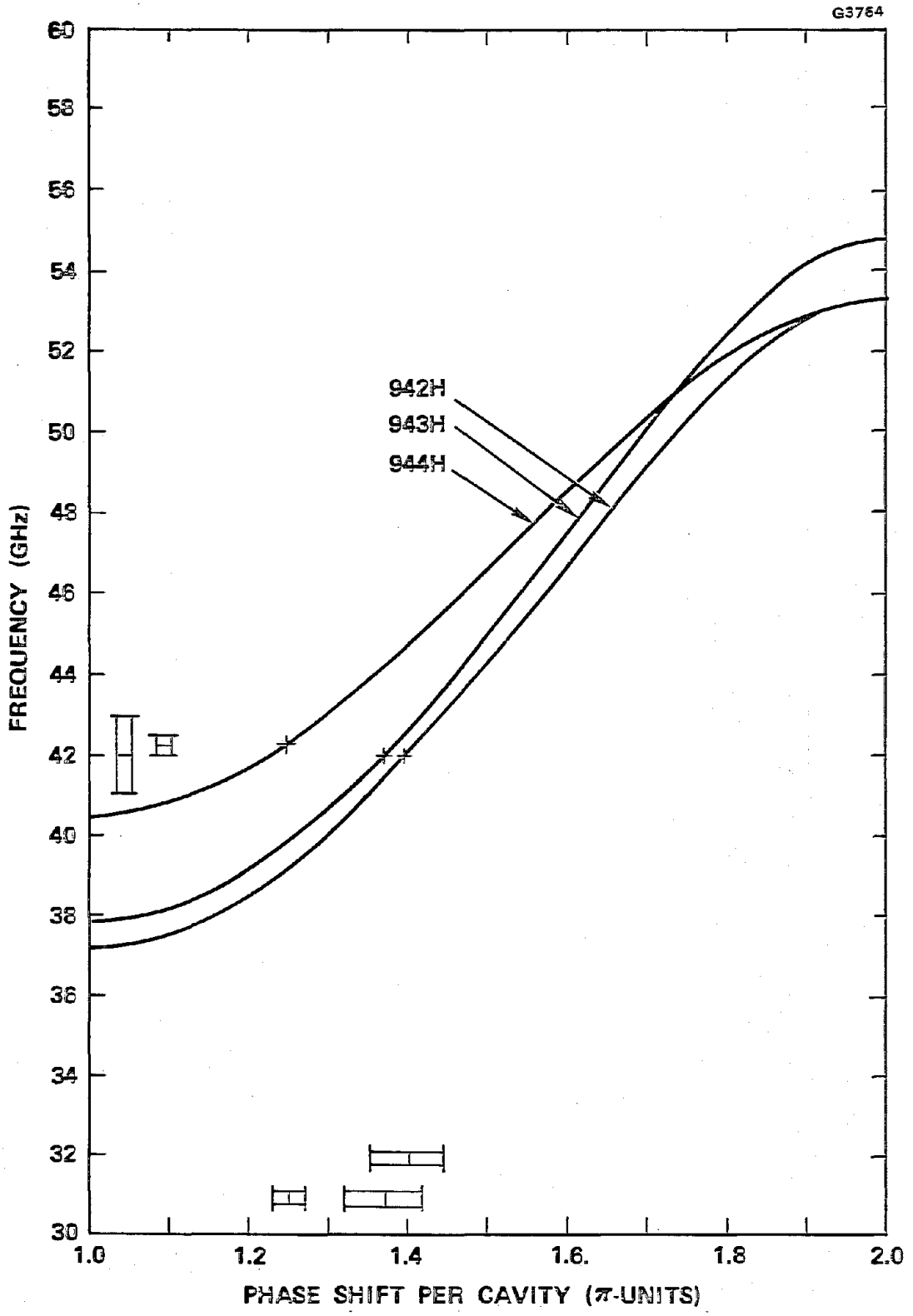

Figure 3-6 Final frequency vs phase ($\omega\beta$) characteristics of the 42 GHz tubes.

TABLE 3-3

CHARACTERISTICS OF FIVE BASIC RF DESIGNS FOR THE 944H

DESIGN	A	B	C	D	E
Basic Efficiency (%)	17	15	15	15	15
Phase Shift at f_o (rad)	1.35π	1.35π	1.25π	1.25π	1.25π
Cold Bandwidth (%)	18	18	29	23	27
Cavity Resonance Frequency (GHz)	48	48	54	51.5	53.3
Beam Voltage (kV)	14	14.5	14	14.5	14.5
Beam Current (mA)	42.0	46.0	47.6	46.0	46.0
Beam Perveance ($\mu A/V^{3/2}$)	.0254	.0263	.0287	.0263	.0263
γa	1.17	1.17	1.18	1.15	1.15
Beam Hole Diam (in) Beam Hole Diam (cm)	.0235 .0597	.0242 .0616	.0237 .0603	.0236 .0600	.0236 .0600
3 dB Bandwidth (GHz)	- - -	.74	1.06	.75	.95
Cavities/Section	- - -	28-28-36	30-30-40	28-28-40	32-32-39

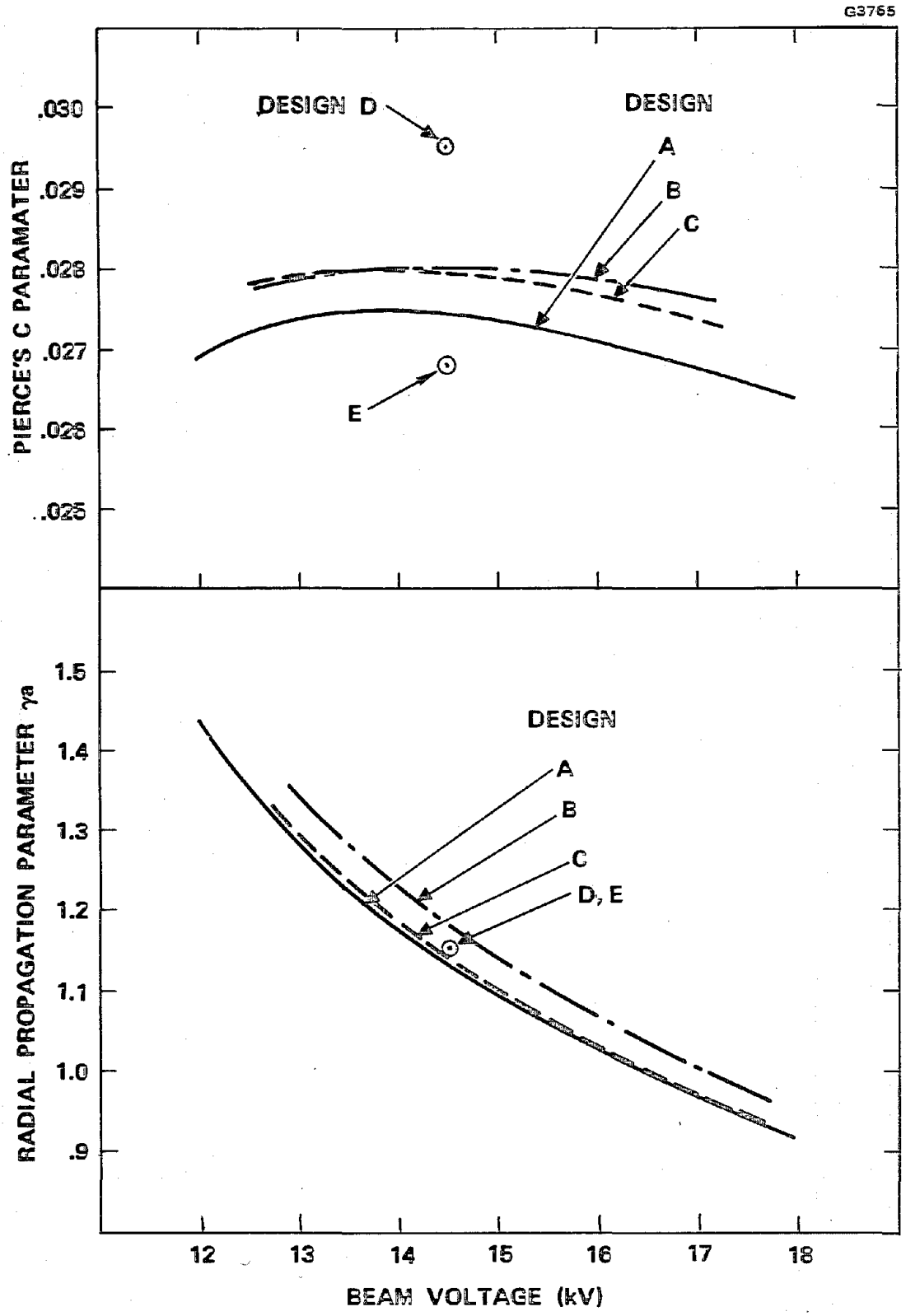

Figure 3-7 Pierce's growth parameter C and radial propagation parameter γa of several circuit designs for the 944H.

C parameter was about the same as in design B (Figure 3-7)*, while the 3 dB bandwidth increased to more than 1 GHz.

At this point an intermediate-bandwidth circuit with consequently greater interaction strength seemed better than either of designs B and C. An upper cutoff of 51.5 GHz was selected for design D, with a magnetic ferrule hole size of 0.640 cm, and cold test parts were ordered. Subsequently large signal analysis indicated that the RF dissipation was larger than desired for this circuit. In the final design, E, the bandwidth was again increased to provide reduced circuit dissipation without sacrifice in efficiency. Since the cavity diameter of the available cold test circuit could not be reduced, however, the magnetic design was left unchanged.

Figure 3-8 shows the $\omega\beta$ diagrams that were assumed for the different designs, and Figure 3-9 illustrates the small signal gain calculations for designs B, C, and D. The small signal gain curve for the final design E was very similar to that of design C, having only slightly smaller bandwidth. (See also Figure 3-18.)

The initial design for the 985H circuit, in which a phase shift of 1.35 π at midband and a cold bandwidth of 30 percent were assumed, yielded a 3 dB bandwidth of 1.3 GHz (Table 3-2). To get larger bandwidth both the operating phase shift and the bandwidth were increased. It was estimated that a 3 dB hot bandwidth of 2.1 GHz could be achieved with a phase shift of 1.42 π and a cold bandwidth of 35 percent.

---

* A note of caution should be injected regarding the graph of C vs voltage. The variation of C with voltage for a given design is meaningful, but quantitative comparison of the C parameter for two different design values of phase shift per cavity, for the purpose of estimating the efficiency performance, may be misleading since both the cavity loss and the effect of the backward wave increase strongly as the low frequency cutoff is approached.

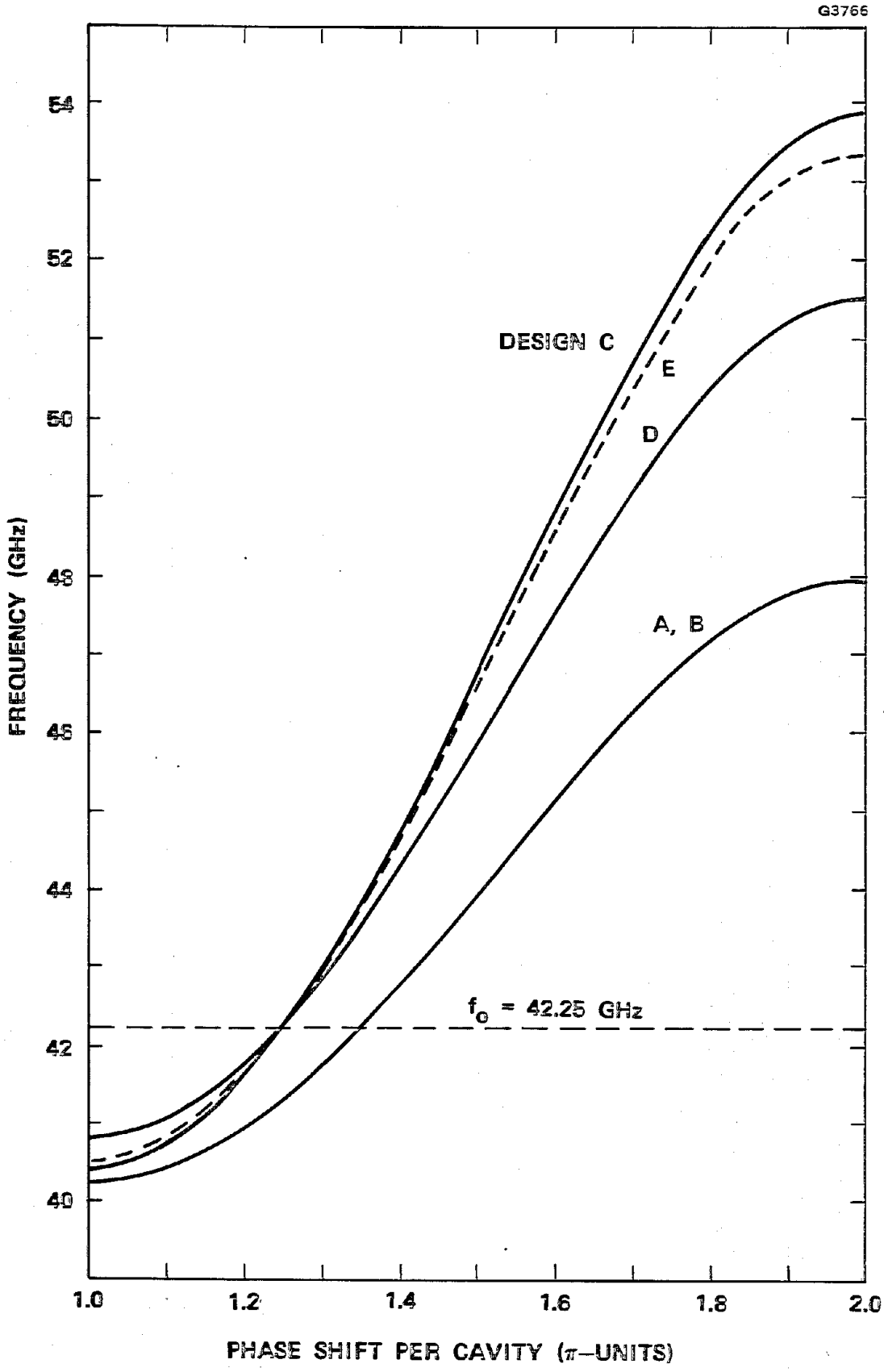

Figure 3-8 Frequency vs phase characteristics assumed for different circuit design for the 944H.

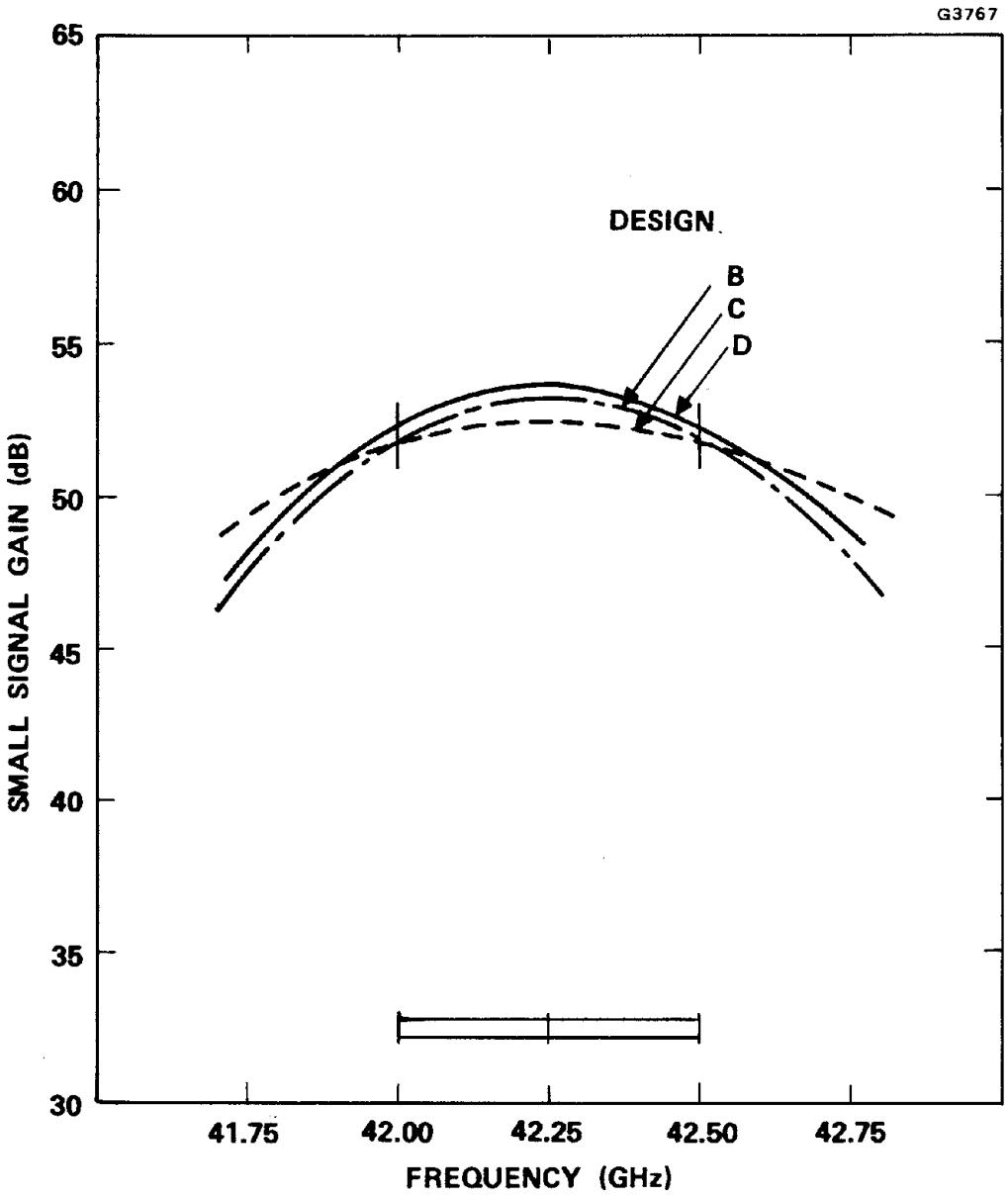

Figure 3-9 Small signal gain vs frequency of three circuit designs for the 944H.

However, the estimate was uncertain due to lack of knowledge of the exact dispersion characteristics, because the circuit might be close to the coldband-limiting merged-mode condition.

When measured circuit data (Appendix A) subsequently became available, it was determined that the maximum cold bandwidth, at merged modes, was approximately 34 percent. This assumed a phase shift of 1.42 π at mid-band. A calculation was made of the hot performance bandwidth of three different cold circuit bandwidths near and including the maximum value. The results, listed in Table 3-4, reflect the combined effect of changing impedance and phase velocity dispersion. The largest performance band was obtained with a cold bandwidth of 31 percent. Although the 3 dB bandwidth was only 1.5 GHz the circuit was used in the final design, since it could not be established that a circuit designed for a larger phase shift operation would give wider band performance, except by another series of measurements on a second test circuit. The final passband characteristics of the two lowest modes in the 985H circuit are illustrated in Figure 3-10. Also shown is the voltage line for 25 kV operation.

3.2.2 Large Signal Design Analysis for High Interaction Efficiency

A two-step phase velocity taper was included at the end of the output section to achieve high interaction efficiency. The taper for each tube was designed by large signal computer analysis, using a one-dimensional continuous-interaction computer program.

Although a large signal coupled-cavity program is also available at Hughes, which is based on the same circuit and interaction models that are employed in the small signal gain program, the continuous-interaction program was the preferred design tool in this instance. One reason was that a great deal of experience had accumulated by which

TABLE 3-4

HOT BANDWIDTH PERFORMANCE CALCULATED FOR
THE 985H WITH DIFFERENT COLD BANDWIDTH CIRCUITS
(PHASE SHIFT AT MIDBAND = 1.42π)

Cold Bandwidth (%)	28	31	34
Max. SSG, 3 Sections (dB)	54.6	54.4	55.2
3 dB Bandwidth (GHz)	1.44	1.50	1.43
Total No of Cavities	164	172	180

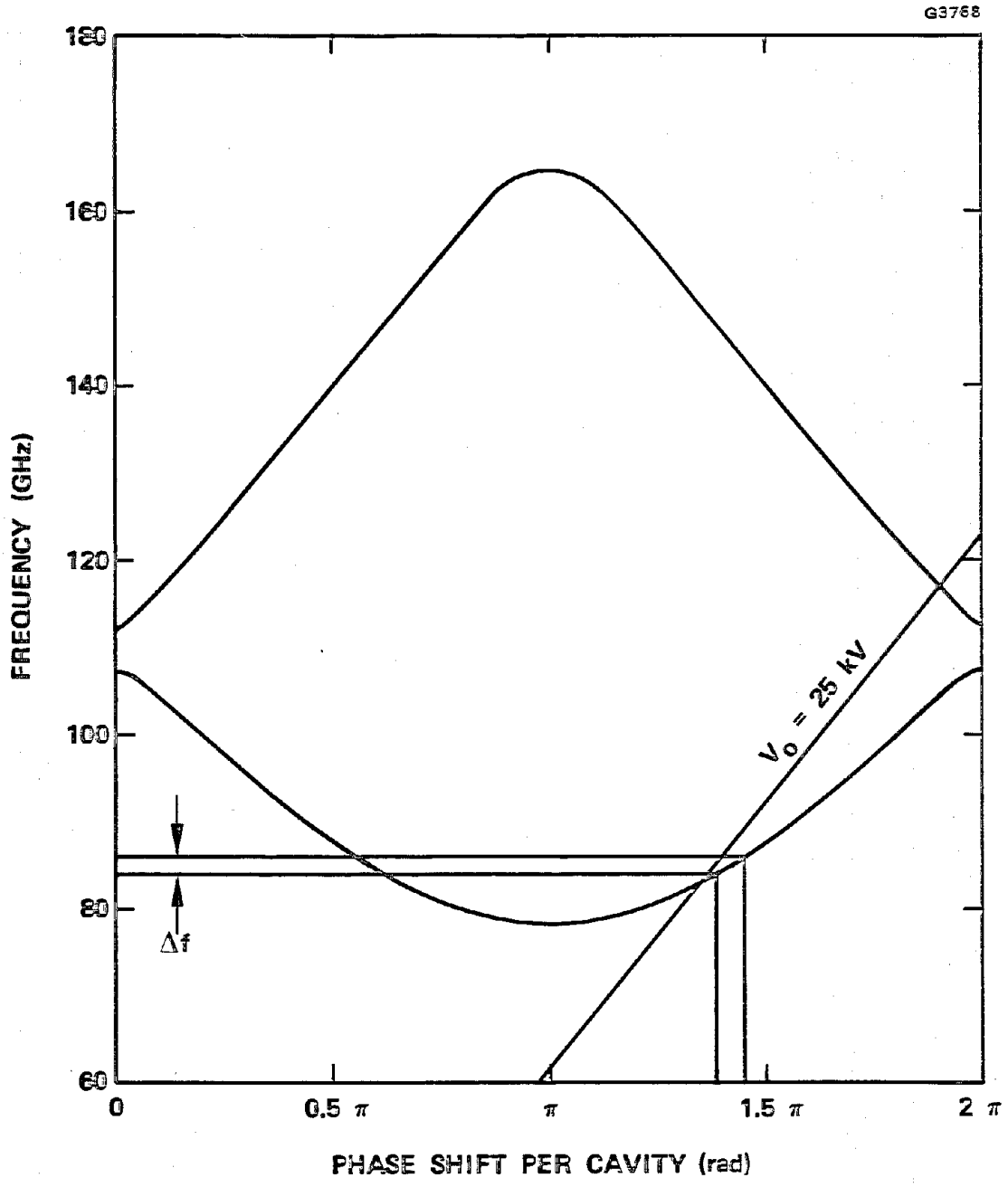

Figure 3-10 The cavity and the slot modes of the final circuit design for the 985H.

very reliable results could be expected for the present designs. Thus good agreement had been demonstrated with performance data taken on 100-200 W tubes at 12[3] and 15 GHz[4] and on same closely related devices at W-band frequencies. A second reason was that the computation time and effort would be significantly reduced. The unusually large number of cavities in the tubes under study would make a computation method in which each cavity is treated separately naturally more expensive. Also, the lack of backward wave in the continuous-interaction program greatly expedites the design of the velocity taper. Each different taper design only requires recalculation of the interaction in the taper itself (not in the driver part of the output section), and an arbitrary number of cavities in the second taper is evaluated with a single run.

Because the program is based on a simplified model, however, it is necessary to use appropriately modified interaction parameters. In particular, the RF wave phase velocity and interaction impedance may be corrected from their cold values to provide agreement between the calculated results and actual performance. Both past experience[3] and predictions with the coupled cavity small signal gain program were used as a guide in the present study.

The method is illustrated for the 943H in Figures 3-11 and 3-12. Figure 3-11 displays the gain vs frequency calculated with the coupled cavity small signal gain program. The top curve is for a uniform circuit comprised of three sections, while the next lower curve is the gain at the end of two sections. The circled points have been calculated with the large signal program for the same two sections using the effective hot interaction parameters shown in Figure 3-12.

Since the small signal program has demonstrated excellent correlation with measured bandwidth performance, the main objective is to reproduce

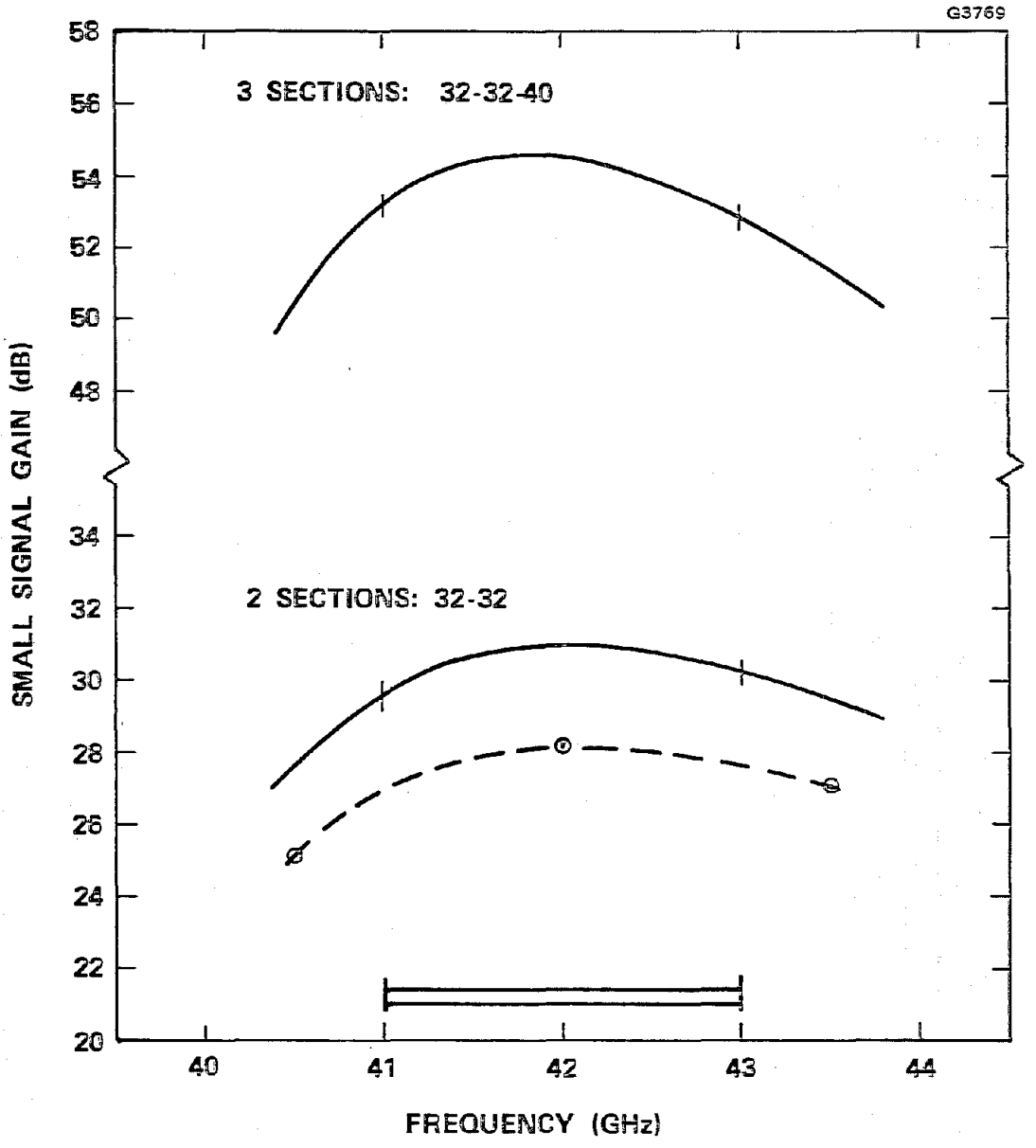

Figure 3-11 Gain of the basic 943H circuit calculated with the small signal program (solid curves) and with the large signal program at low drive levels (circled points).

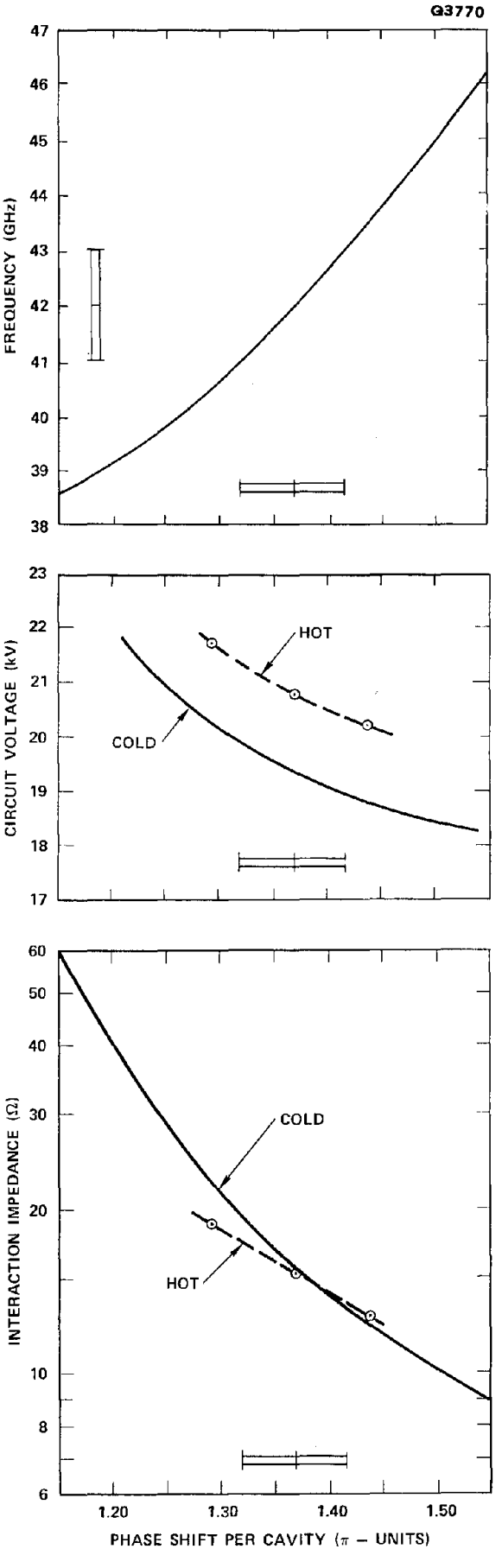

Figure 3-12

Measured characteristics of the cold 943H circuit and the effective hot interaction parameters used in the large signal program for calculation of the results in Figure 3-11.

the shape of the calculated small signal gain curve with the large signal program at low drive levels. The overall magnitude of the calculated small signal gain tends to be somewhat uncertain. The simple one-dimensional beam model in the program does not realistically represent the actual thermal electron beam in the tube, and the assignment of an equivalent beam size is ambiguous (a smaller gain could have been obtained by assuming a smaller beam).

Agreement between the gain levels calculated with the two programs could also have been obtained by increasing the hot interaction impedance. Physically, however, the effective impedance is expected to be generally lower than the measured value, particularly at low values of phase shift per cavity where backward wave effects become more pronounced. The phase velocity in the large signal program is increased by approximately 3½ percent over the measured value. (In Figure 3-12 the phase velocity has been expressed as a voltage, called the circuit voltage, by which electrons would have to be accelerated to acquire a speed equal to the phase velocity.)

After the effective interaction parameters in the large signal program were determined by such a "computer calibration", the efficiency performance was evaluated with a variety of taper configurations for each tube design. A computer-generated plot for the final design of the 943H at midband 42 GHz is reproduced in Figure 3-13. The calculation was performed over a short driver section followed by the complete output section. It is not necessary to include additional gain sections of the tube for predicting the interaction efficiency. At the tube output, which is located at the (normalized) axial distance of $y = 9.05$, an interaction efficiency of 16.6 percent was predicted. This value was corrected by the dissipative loss in the output coupler, step transformer, and RF window, estimated to be 0.15 dB, yielding a net basic efficiency of 16.0 percent.

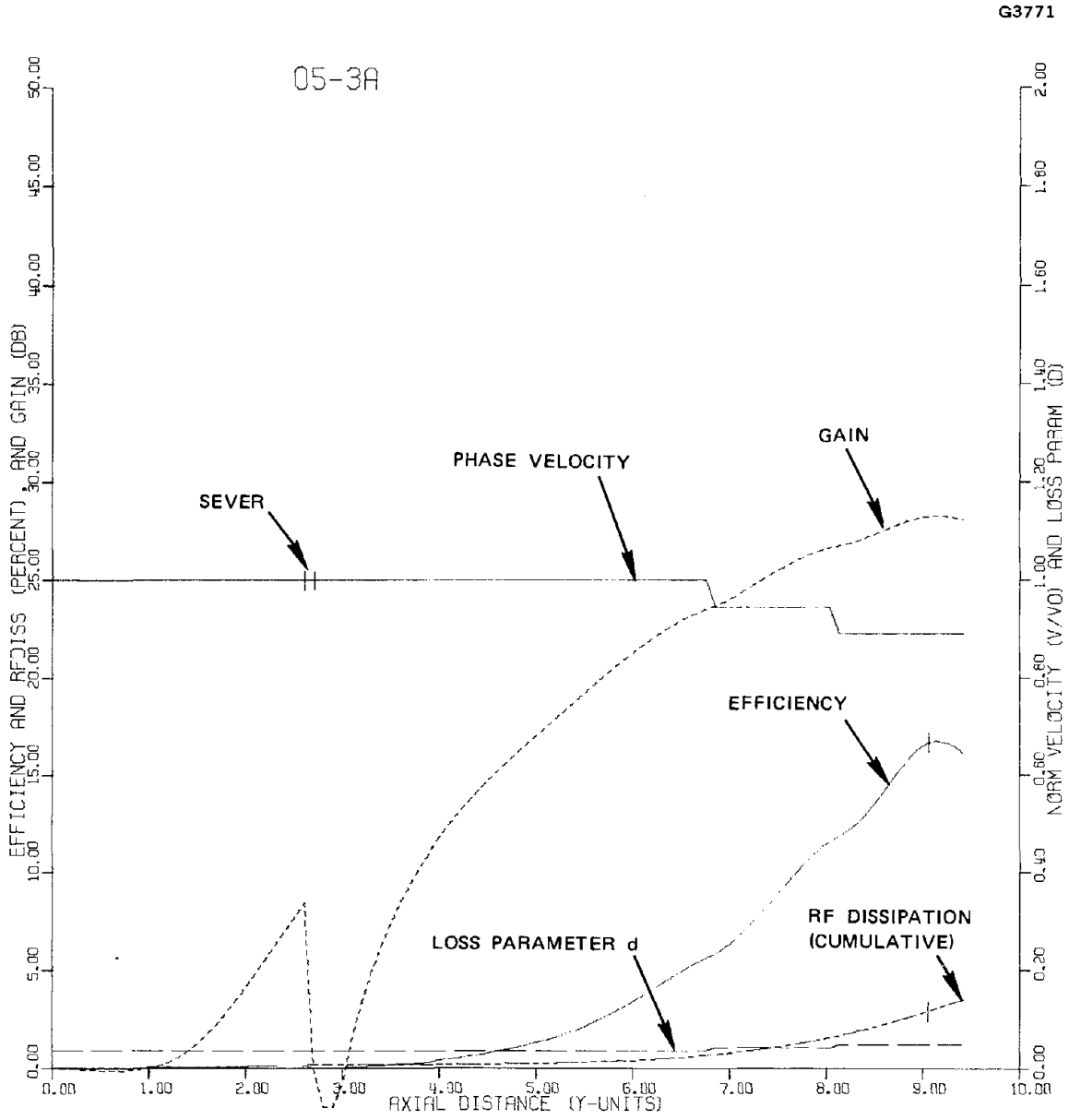

Figure 3-13 Computer plot of a large signal run for the 943H final design at midband.

Large signal calculations were also performed at 40.5 and 43.5 GHz. Figure 3-14 exhibits the results in a plot of basic efficiency vs frequency for both the 943H and the 942H. The predicted minimum efficiency over the operating band 41-43 GHz is 15.3 percent and 13.7 percent for the respective tube designs. These values were one and a half times as large as assumed at the start of the analysis. Similar plots for the 944H and the 985H are displayed in Figures 3-15 and 3-16. In both these cases the predicted efficiency was very close to the initially assumed values.

3.2.3 Circuit Design and Performance Data

The final circuit configurations are detailed in Table 3-5, while the cavity dimensions are given in Figure 3-17. In the taper cavities only the dimensions of the cavity height and gap are changed. This has generally proved to be satisfactory in other designs. The most critical dimension is the gap, which would require a tolerance of approximately 2 microns (0.0007 inches) for the 42 GHz tubes and 1.3 microns (0.0005 inches) for the 85 GHz design. Most other dimensions could be relaxed in tolerance by a factor of two.

Figure 3-18 shows the small signal gain calculated for the complete 944H circuit. The gain without the taper is also plotted for comparison. In these calculations the circuits were terminated with the characteristic impedance, rather than hot matched, while the interaction strength was reduced in the couplers and termination cavities. In practice, additional external mismatches which have not been here included, would generally tend to increase the gain ripple with frequency.

No special oscillation suppression methods are expected to be necessary or have been assumed. This is concluded from both an extensive

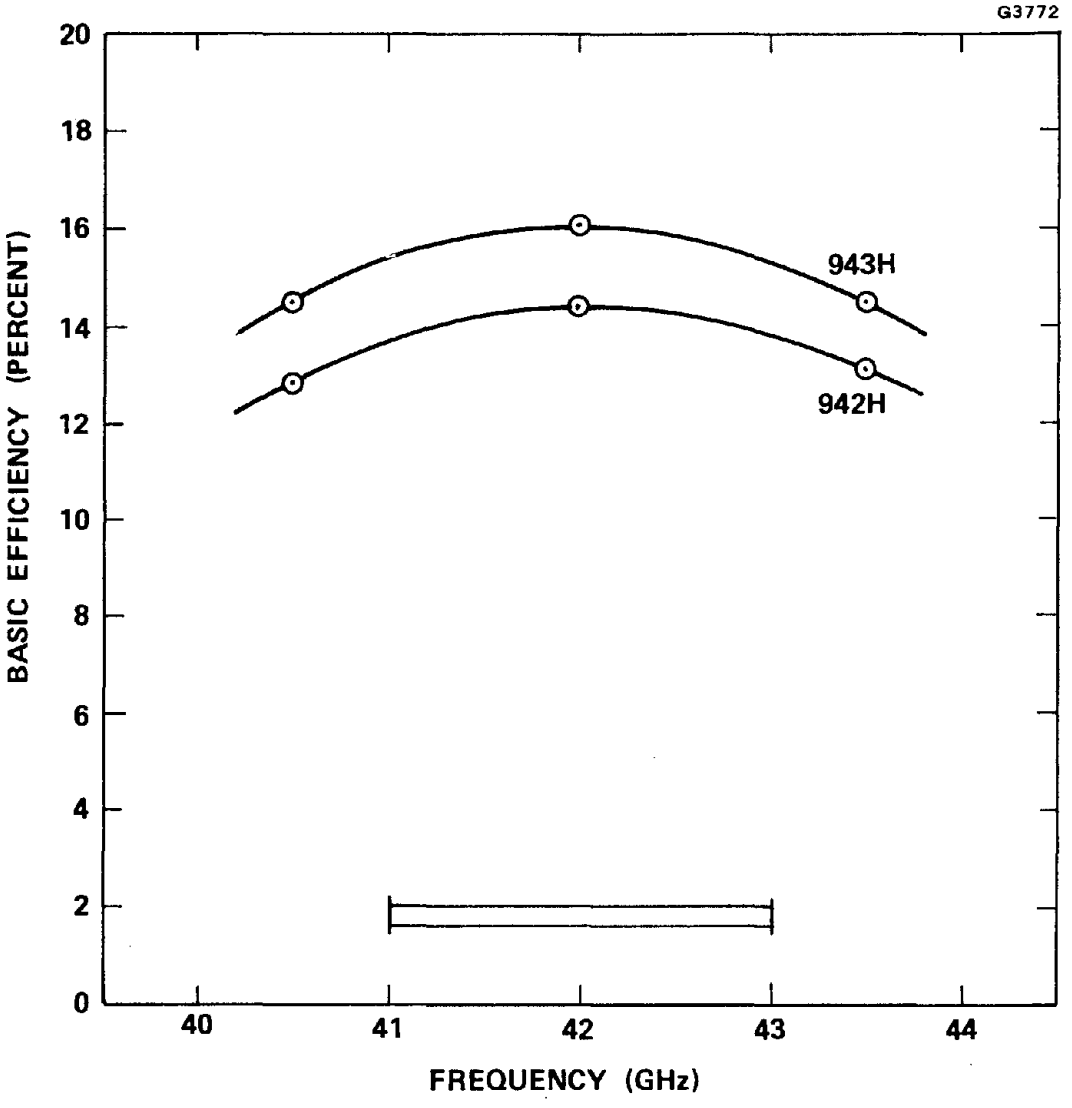

Figure 3-14 Predicted basic efficiency of the 942H and 943H vs frequency.

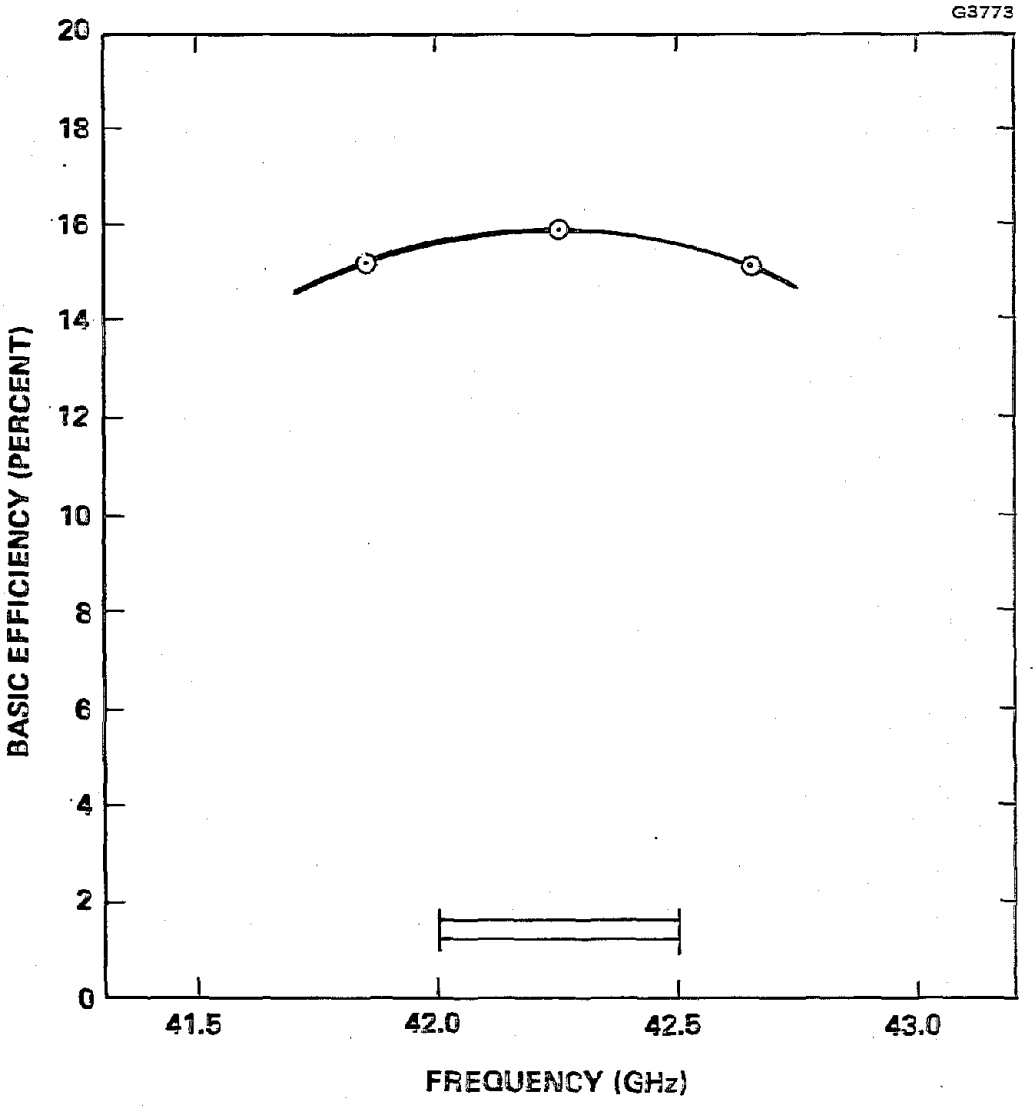

Figure 3-15 Predicted basic efficiency of the 944H vs frequency.

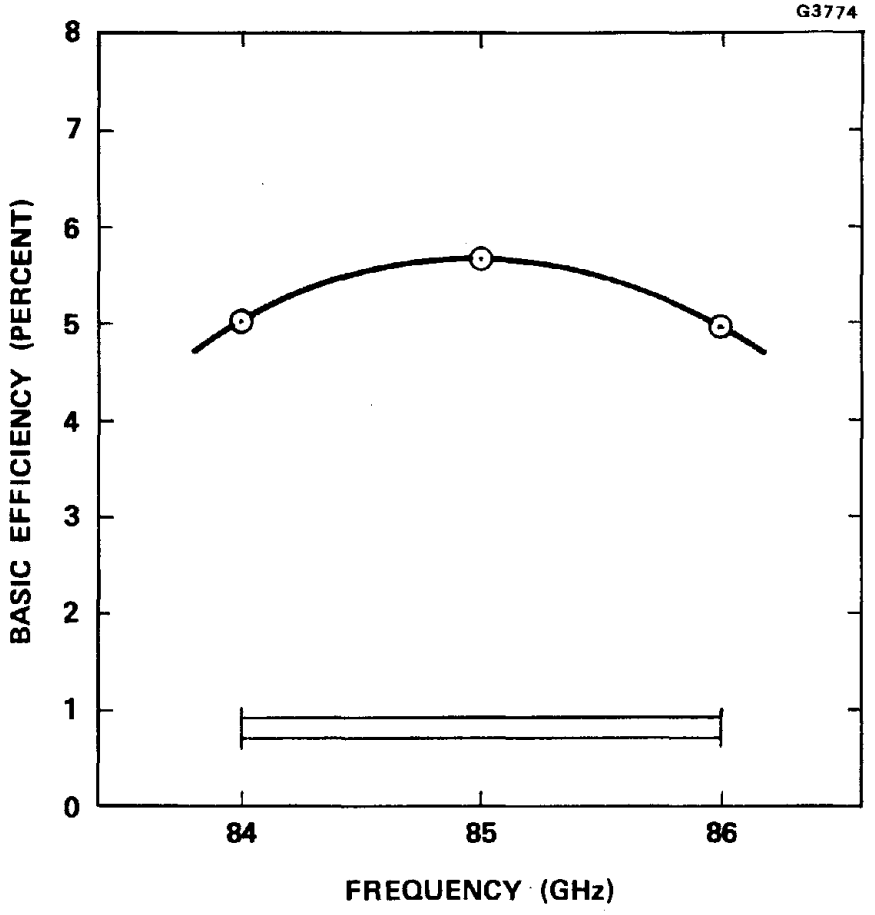

Figure 3-16 Predicted basic efficiency of the 985H vs frequency.

TABLE 3-5
RF CIRCUIT CONFIGURATION

TUBE	942H	943H	944H	985H
Number of Cavities*:				
Section I	38	36	34	58
Section II	36	33	30	55
Section III:				
Standard	44	39	41	63
Taper 1	14	13	13	13
Taper 2	12	10	11	5
Relative Phase Velocity:				
Taper 1	.95	.945	.939	.975
Taper 2	.90	.89	.88	.95

*Couplers and termination cavities not included in count

stability analysis that was performed on a closely related TWT with the small signal gain program, and from practical experience on similar mm wave devices. Table 3-6 summarizes the RF output power and RF dissipation performance of all four designs. The loss per cavity was estimated by correlating loss calculations (using the cavity configurations and the $\omega\beta$ characteristics of the design) with available loss data on existing mm wave tubes that have been constructed along the lines

G3775

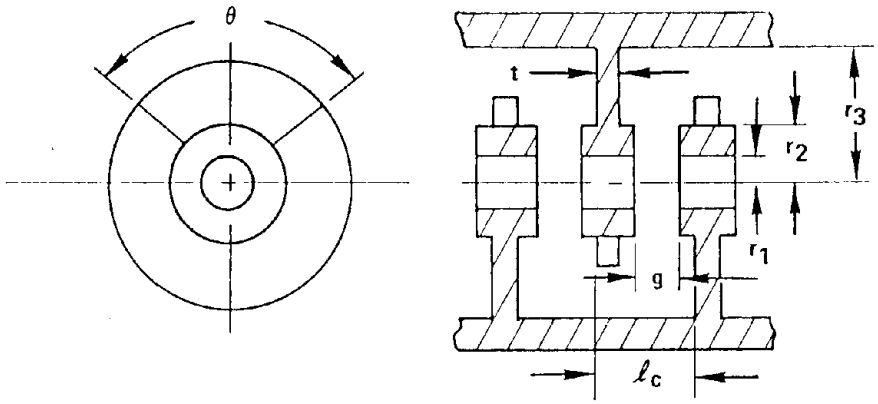

TUBE	942H	943H	944H	985H
$2r_1$ – cm (in.)	.0630 (.0248)	.0660 (.0260)	.0600 (.0236)	.0676 (.0266)
$2r_2$ – cm (in.)	.1036 (.0408)	.1067 (.0420)	.0955 (.0376)	.0955 (.0376)
$2r_3$ – cm (in.)	.3155 (.1242)	.3084 (.1214)	.3363 (.1324)	.1748 (.0688)
θ – rad (^{o})	2.618 (150)	2.670 (153)	2.269 (130)	2.182 (125)
t – cm (in.)	.0279 (.0110)	.0305 (.0120)	.0254 (.0100)	.0191 (.0075)
STANDARD CIRCUIT:				
ℓ_c – cm (in.)	.1209 (.0476)	.1308 (.0515)	.0995 (.0392)	.0734 (.0289)
g – cm (in.)	.0354 (.01395)	.0411 (.01619)	.0284 (.01117)	.0293 (.01153)
FIRST TAPER:				
ℓ_c – cm (in.)	.1148 (.0452)	.1237 (.0487)	.0935 (.0368)	.0716 (.0282)
g – cm (in.)	.0326 (.01285)	.0376 (.01482)	.0261 (.01027)	.0282 (.01109)
SECOND TAPER:				
ℓ_c – cm (in.)	.1087 (.0428)	.1163 (.0458)	.0877 (.0345)	.0698 (.0275)
g – cm (in.)	.0299 (.01175)	.0342 (.01345)	.0237 (.00934)	.0270 (.01065)

Figure 3-17 Final cavity dimensions.

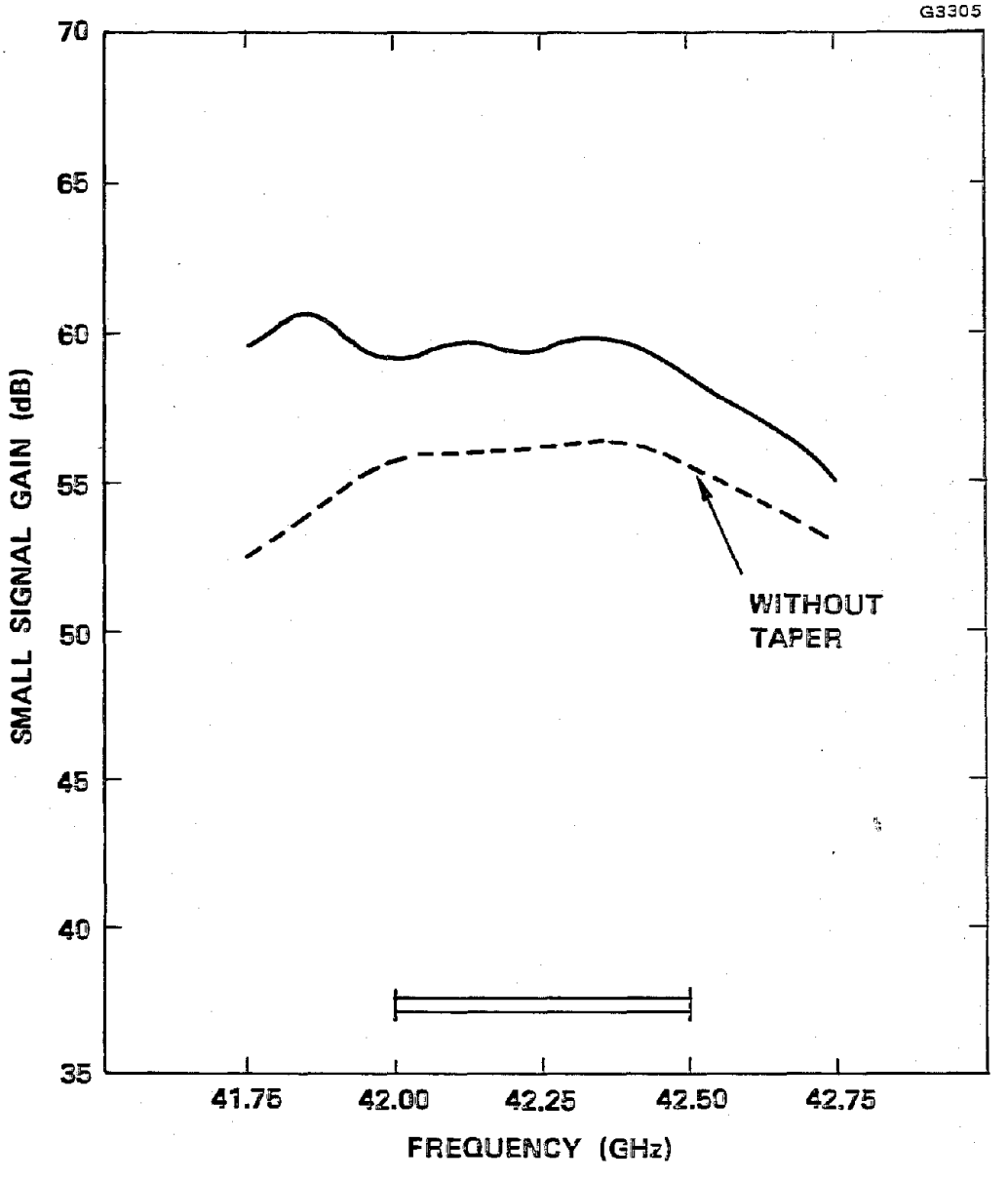

Figure 3-18 Small signal gain vs frequency of the 944H.

proposed in the present study.* A cavity Q of 830 was assumed for the 942H and 943H. The value was revised to 950 for the 944H, while a Q of 710 was used for the 985H. The ratio of RF dissipation to RF output power varies over the frequency band. It is largest at the high frequency end and also depends on the exact drive level. The listed values are for conditions close to saturation.

The large dissipation of the 985H (approaching 50 percent) results from the combined effect of weak interaction and moderately high loss per cavity. The weak interaction is ultimately caused by the focusing constraint, which necessitates a large beam hole in relation to the wavelengths involved. (As mentioned in Section 3.1.4 the parameter γa was 1.96, which is exceptionally large.) Any relaxation of the focusing constraint would result in a more efficient tube design. Appendix B describes the improved RF performance that could be obtained if the cathode current density, which is one of the relevant focusing parameters, were increased from 1 A/cm^2 to 2 A/cm^2.

*Experimental data on some sintered W-band circuits and on a circuit above 90 GHz were available. Approximate calculations of cavity loss yielded values which were typically 60-70 percent of the measured loss on these circuits. (Most of the discrepancy is likely to result from the increased resistance of the sintered joints between the cavities in the actual structure.) In the design analysis of the 942H and 943H, the loss values used (Table 3-6) were conservative. Because of the relatively strong interaction and wide bandwidths the effect of RF dissipation is fairly small in these designs. For the 944H and 985H, on the other hand, the predicted performance is quite strongly dependent on resistive effects. The loss in these designs was more carefully reviewed to reflect the best estimates that could be made. The cavity Q, quoted in the text, is somewhat fictitious and has been included only for general reference purposes. More specifically, it is the (frequency-independent) Q in an equivalent circuit model that yields the listed loss per cavity at operating midband frequency.

TABLE 3-6

RF OUTPUT POWER AND RF DISSIPATION PERFORMANCE

TUBE		942H	943H	944H	985H
Beam Power	(kW)	1.11	2.00	.667	4.00
Loss/Cavity at f_o	(dB)	.032	.033	.046	.053
Coupler & Window Loss	(dB)	.15	.15	.15	.20
Min. Net Basic Eff.	(%)	13.7	15.3	15.6	5.0
Min. RF Output Power	(W)	152	306	104	200
RF Dissipation/Output Power		.23 - .26	.20 - .24	.28 - .29	.32 - .47
Max. RF Dissipation	(W)	38	70	30	92

3.3 ELECTRON GUN AND PERIODIC PERMANENT MAGNET FOCUSING

The electrical and mechanical designs of four electron guns for the 942H, 943H, 944H and 985H TWTs were completed. Further, periodic permanent magnet (PPM) focusing arrays for each of the four tube types were also defined. Table 3-7 gives the gun designation numbers and pertinent electrical parameters.

3.3.1 Electron Gun Design

The design procedure was the same for each gun. Graphs in a paper by Herrmann[5] provided an initial set of dimensions for: cathode sperical radius, anode spherical radius, beam minimum diameter, and distance from cathode edge to beam minimum for a given cathode button diameter, electron gun perveance, cathode temperature and electron beam voltage. The voltage gradation between cathode and anode was determined,[6] and a scaled up analog of the cathode-anode region was established in the electrolytic tank.[7] Figure 3-19 is a photograph of the Hughes electrolytic tank. A focus electrode was experimentally configured which causes the measured potential variation between cathode and anode to equal the value previously calculated. In order to achieve this, it is usually necessary to make minor adjustment of the spherical anode surface configuration in the vicinity of the anode aperture. The axial potential variation is measured by means of a motorized probe, which travels in the electrolyte along the beam edge of the electron gun analog. This potential is recorded by an x-y plotter. Figure 3-20 shows actual plots of the measured and calculated electron gun (232B) potential vs axial distance. Separate magnified plots of the important region in the vicinity of the cathode are also recorded.

A computer program, developed from a program by Herrmannsfeldt,[8] provides additional important characteristics of the design achieved in the

TABLE 3-7

GUN DESIGN PARAMETERS

TWT	942H	943H	944H	985H
Electron Gun	223-B	222-B	232-B	224-B
Voltage (kV)	17	21	14.5	25.6
Current (mA)	65.4	95.2	46.0	160
Perveance ($\mu A/V^{3/2}$)	.0295	.0313	.0263	.0405
Cathode Loading (A/cm^2)	1.0	1.0	1.0	1.0
Beam Aperture DIA	.063	.066	.060	.068

E1278

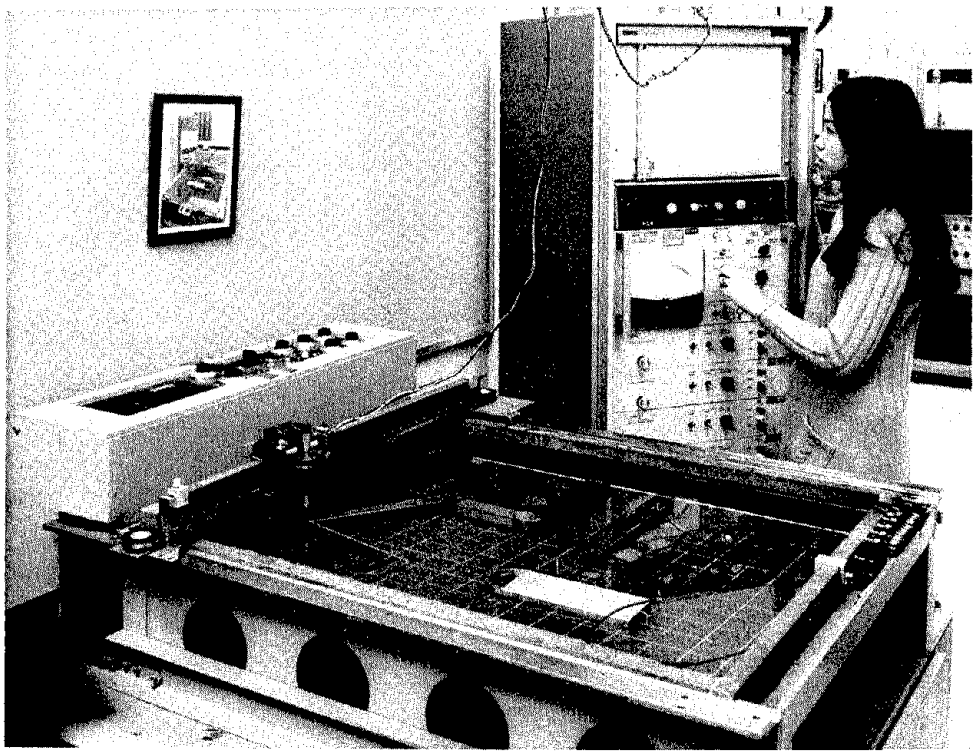

Figure 3-19 Hughes electrolytic tank used for electron gun design.

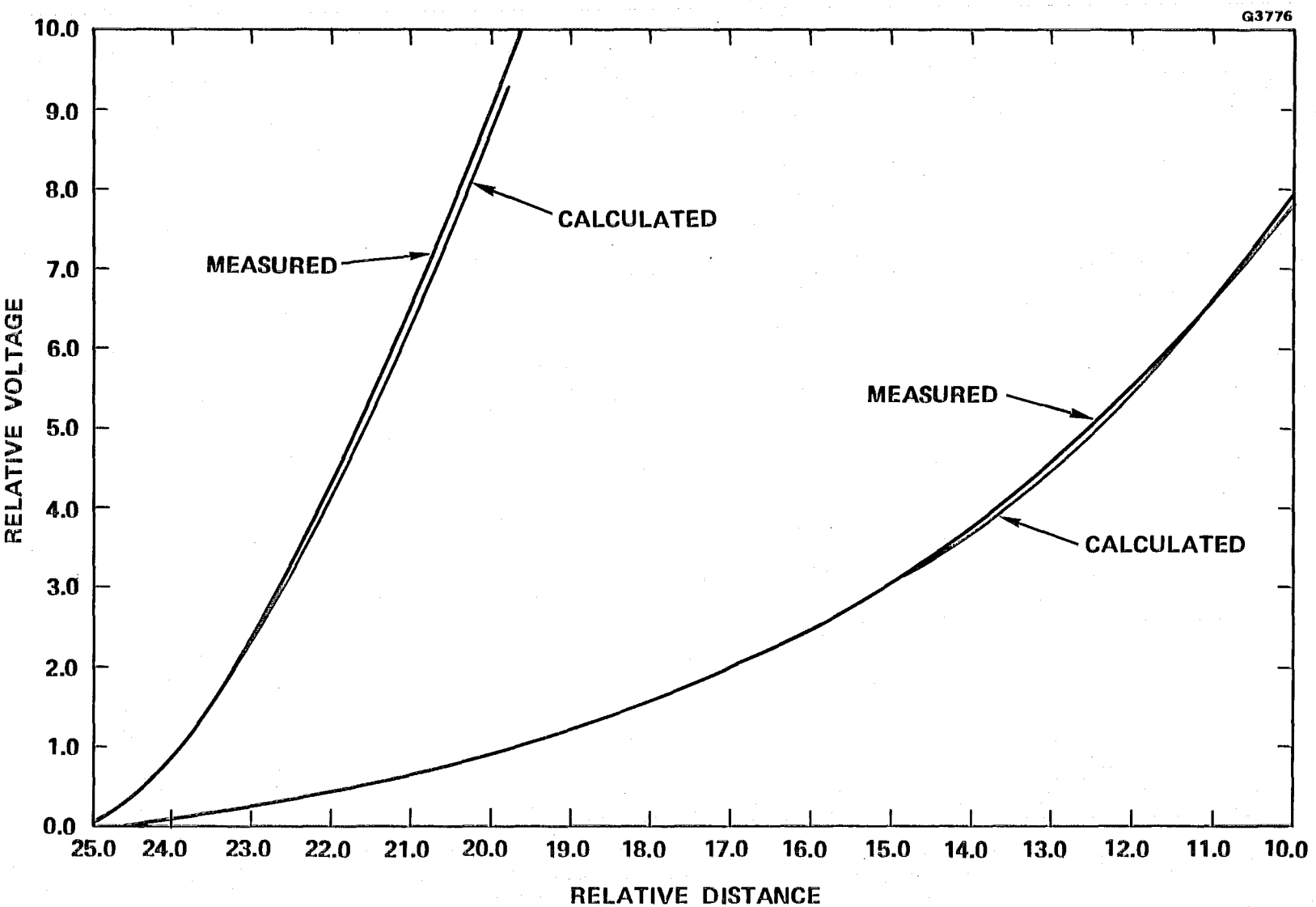

Figure 3-20 Measured and calculated values of axial cathode - anode potential variation of electron gun 232B for the 944H TWT. Measured values were determined from electrolytic tank analog.

electrolytic tank. Inputs to this computer program are the cathode, anode, and focus electrode configurations. The computer output is a plot of equipotential surfaces and electron trajectories. Figure 3-21 depicts this kind of plot for the electron gun of the 944H TWT. Important information obtained is: uniformity of cathode current distribution, axial position of the electron beam minimum and the diameter of the electron beam at its minimum. In addition, tabular data shows: potential gradation along electron gun axis and the electron gun perveance. This latter quantity must agree with the design value of perveance originally chosen.

The focused electron beam computer program is employed to determine the peak magnitude and period of the magnetic focusing field and the quality of the focused electron beam. Figure 3-22 shows a plot of the focused electron beam for the 944H. Also included is the periodic magnetic focusing field and a line representing the beam aperture diameter of the interaction circuit. r_{99} is a radius which encloses 99% of the electron beam current. Similarly, r_{95} encloses 95% of the electron beam current. r_o is the statistical beam radius. Optimum beam focusing has been achieved when the ripple in r_o is minimum. Table 3-8 summarizes electron gun design for the four TWTs. Figure 3-23 is a geometric diagram of the electron gun configuration. Table 3-9 lists all important electron gun dimensions.

3.3.2 Periodic Permanent Magnet Focusing

As cited, the focused electron beam computer program determines the optimum PPM field for a given magnet period. Criteria for this latter quantity was described in Section 3.1.1, Interaction Strength versus Focusing Constraint.

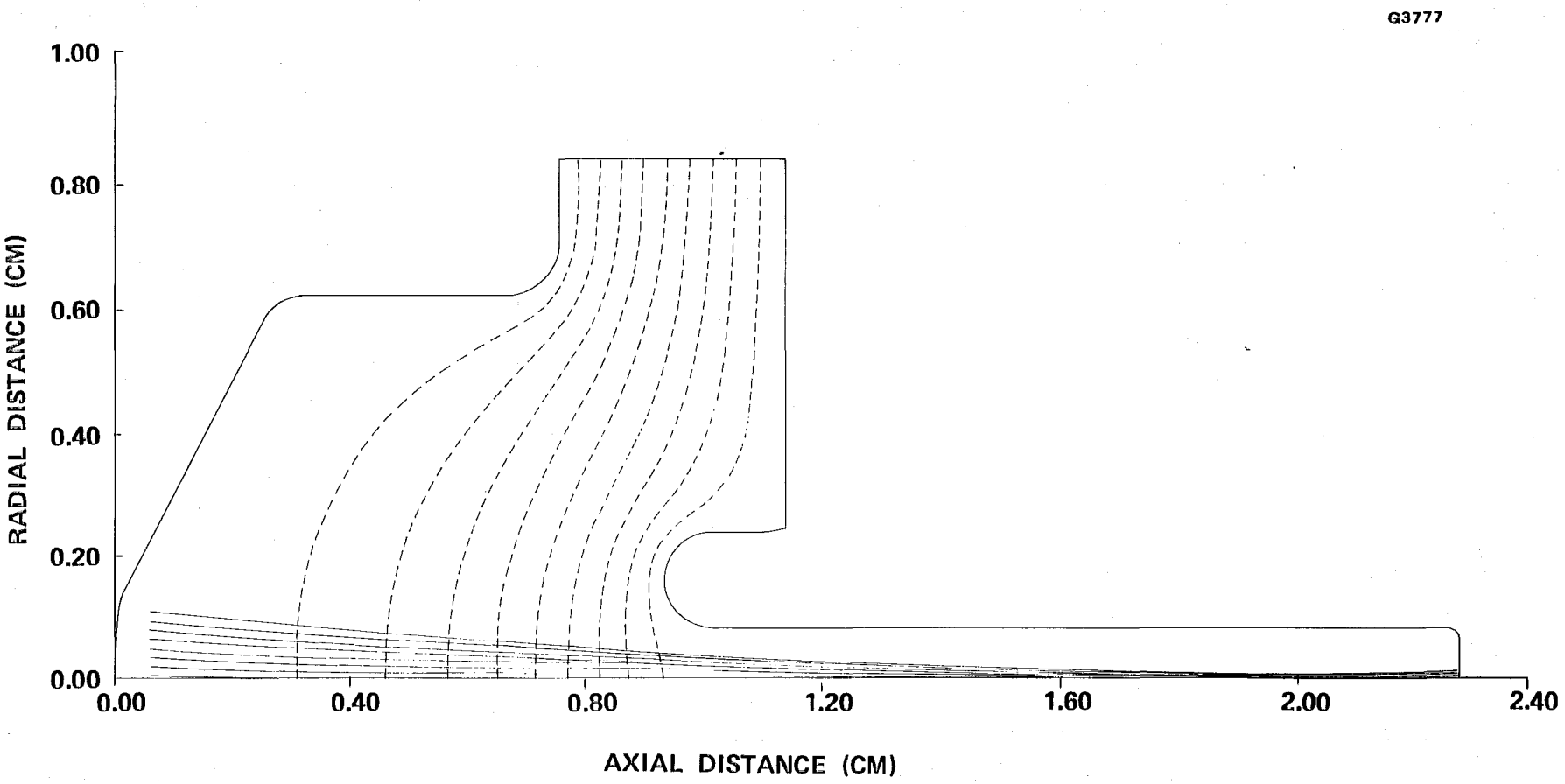

Figure 3-21 Computer plot of equipotential surfaces and electron trajectories of the 944H electron gun.

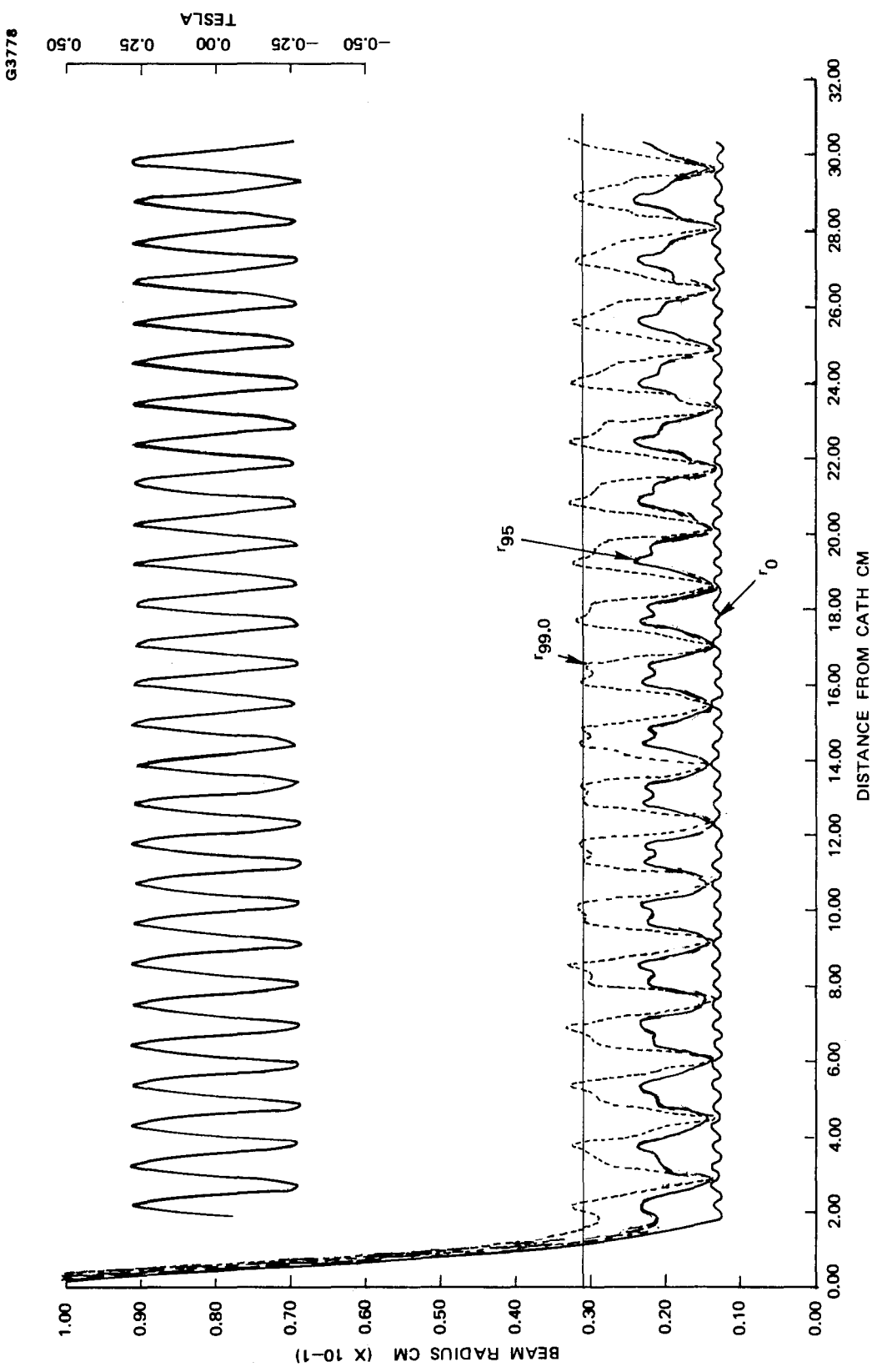

Figure 3-22 Computer plot of the foucsed electron beam of the 944H TWT. r99 and r95 are radii which enclose 99% and 90%, respectively, of the electron beam. r_o is a statistical rms radius. The required periodic magnetic field is also shown.

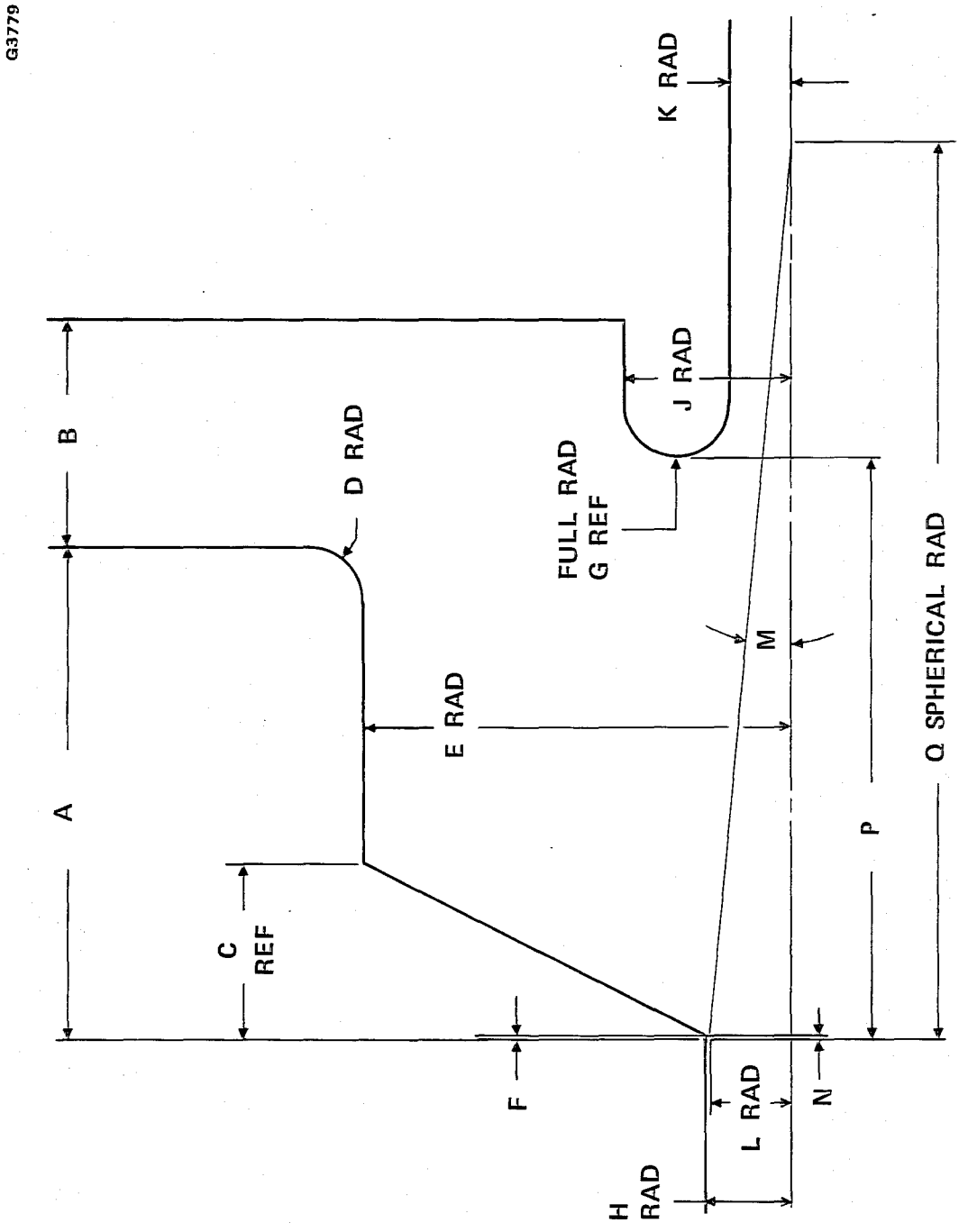

Figure 3-23 Electron gun geometric diagram.

TABLE 3-8

ELECTRON GUN DESIGN SUMMARY

Gun Designation	222-B	223-B	224-B	232-B
TWT	942H	943H	985H	944H
Output Power (W)	200	100	200	100
Center Frequency (GHz)	42	42	85	42.0-42.5
Beam Voltage, V_o (kV)	21	17	25	14.5
Beam Current, I_o (mA)	95.2	65.4	160	46.0
Beam Perveance ($\mu A/V^{3/2}$)	.0313	.0295	.0405	.0263
Cathode Loading (A/cm^2)	1.0	1.0	1.0	1.0
Beam Hole Diameter (cm)	.066	.063	.0675	.060
Effective Beam Filling Factor, b/a	.42	.42	.42	.42

TABLE 3-9

ELECTRON GUN DIMENSIONAL SUMMARY

(See Figure 3-23 for Definition of Symbols)

Gun Designation	222-B	223-B	232-B	224-B
TWT	942H	943H	944H	985H
A (cm)	.984	.912	.7539	1.208
B (cm)	.535	.302	.3467	.501
C (cm)	.333	.319	.2736	.420
D (cm)	.105	.091	.0826	.119
E (cm)	.804	.712	.6533	.990
F (cm)	.0040	.0040	.0061	.0044
G (cm)	.105	.079	.0826	.105
H (cm)	.182	.152	.1285	.234
J (cm)	.445	.380	.2499	.368
K (cm)	.235	.222	.0848	.158
L (cm)	.174	.144	.1209	.226
M (degrees)	5.68	5.44	5.04	6.55
N (cm)	.009	.0068	.0053	.0129
P (cm)	1.178	1.014	.8931	1.288
Q (cm)	1.758	1.520	1.3759	1.981

The magnetic circuit consists of a series of periodic cells. The cells are comprised of soft iron pole pieces and samarium cobalt magnets. A computer program calculates the physical design of the PPM array. Figure 3-24 lists all dimensions of the focusing structures for the four types.

3.4 SPENT BEAM ANALYSIS AND REFOCUSING DESIGN

An essential element in a successful multi-stage collector design is knowledge of the characteristics of the electron beam that enters the collector. In this study the spent beam composition was calculated with a three-dimensional large signal computer program, while a scheme of beam refocusing accompanied by beam expansion was utilized to further control and define the electron beam prior to injection.

The computer program used in this effort is based on a deformable-disk model of the electron beam,[9,10] in which the disk radii are variable. The interaction takes place with a continuous RF wave, the approximately synchronous space harmonic in the coupled cavity circuit, just as in the one-dimensional large signal program employed in the RF design. As the beam traverses the interaction region, the axial and radial motion of the electron disks is progressively evaluated. The calculation takes into account the axial and radial electric forces associated with the propagating RF wave and those due to space charge in the bunched beam. Also included are the forces of the magnetic focusing field, which may vary as a function of axial distance in any arbitrary fashion. Rotational motion, resulting from the focusing action of the magnetic field, is included through Busch's theorem.

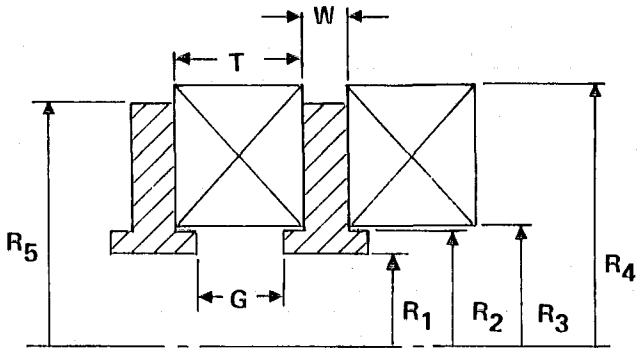

TUBE	942H	943H	944H	985H
PEAK MAGNETIC FIELD (T):				
INITIAL DESIGN	.34	.36	.31	.45
FINAL DESIGN	.30	.34	.28	.49
FERRULE I.D., $2R_1$ – cm (in.)	.610 (.240)	.610 (.240)	.640 (.252)	.432 (.170)
FERRULE O.D., $2R_2$ – cm (in.)	.775 (.305)	.782 (.308)	.808 (.318)	.584 (.230)
MAGNET I.D., $2R_3$ – cm (in.)	.777 (.306)	.785 (.309)	.810 (.319)	.587 (.231)
MAGNET O.D., $2R_4$ – cm (in.)	2.16 (.850)	2.54 (1.00)	2.29 (.900)	2.79 (1.10)
POLE PIECE O.D., $2R_5$ – cm (in.)	2.16 (.850)	2.54 (1.00)	2.29 (.900)	2.54 (1.00)
P.P. THICKNESS, W – cm (in.)	.163 (.064)	.173 (.068)	.168 (.066)	.152 (.060)
P.P. GAP, G – cm (in.)	.320 (.126)	.335 (.132)	.320 (.126)	.292 (.115)
MAGNET THICKNESS, T – cm (in.)	.368 (.145)	.386 (.152)	.366 (.144)	.335 (.132)
MAGNETIC PERIOD, L – cm (in.)	1.062 (.418)	1.118 (.440)	1.067 (.420)	.975 (.384)
RMS FIELD (T)	.211	.237	.200	.345
MAX. POLE PIECE FIELD (T)	1.18	1.20	1.18	1.29

Figure 3-24 Dimensional summary of PPM focusing array.

3.4.1 Generation of Spent Beam Representation

Runs were made with the three-dimensional large signal computer program with the following objectives and constraints.

1. The basic efficiency predicted with a tapered circuit should be close to the anticipated efficiency, obtained by one-dimensional calculations. (The three-dimensional program is not used for RF design because of less extensive practical experience and because the results may be masked by spurious effects due to the detailed development of the beam in the focusing field.)

2. The actual physical focusing field magnitude and period are used.

3. The calculated beam interception on the RF circuit should approximately equal the expected interception due to RF defocusing, typically 3 percent.

From practical experience, a total interception of 5 percent with RF drive has been obtained in tubes operating both in the 12 - 15 GHz range and at W-band frequencies. Since these tubes were designed with similar design concepts that are applied in the present study, it is expected that a 5 percent interception is a realistic estimate. With a DC beam interception of about 2 percent, the increase in interception due to RF drive is therefore typically 3 percent. (With collector depression another 2 percent may be contributed by backstreaming.)

Figure 3-25 shows a computer-generated plot from a run for the 943H. The solid lines are the edge electron trajectories of the 32 disks used in the calculation and the dashed line is the absolute value of the focusing field on the axis, normalized to the peak field. The calculation starts at a small signal level of about 25 dB below saturation and includes a velocity taper at the output. A conversion efficiency of 15.3 percent is obtained at the end of the interaction.

To achieve the desired amount of interception the beam trajectories at the start of the calculation are empirically adjusted by assigning initial slopes to some of the disk edge electrons. This is qualitatively justified by the effect of thermal velocities in the beam. No attempt was made to correlate the selected trajectory slopes with electron gun design data, since the object was merely to generate a representative beam at the end of the RF interaction, according to the listed criteria. The trajectory slopes, dr/dz, at the start of the run in Figure 3-25 were ±0.024, ±0.015, and 0. They were assigned to the 32 disks, initially uniformly distributed in phase over an RF wavelength, in the following pattern: +0.015, 0, -0.015, +0.024, +0.015, 0, -0.015, -0.024 repeated four times. A total interception of 3.3 percent was calculated. In the figure the interception is evidenced by jogs in some of the trajectory curves, arising from disks being clipped by the RF circuit while a fraction of their charge is removed.

Figure 3-26 is a similar plot for the 85 GHz tube. In this case larger initial trajectory slopes, with magnitudes of 0.06 and 0.04, were necessary to obtain an interception of 2.9 percent.

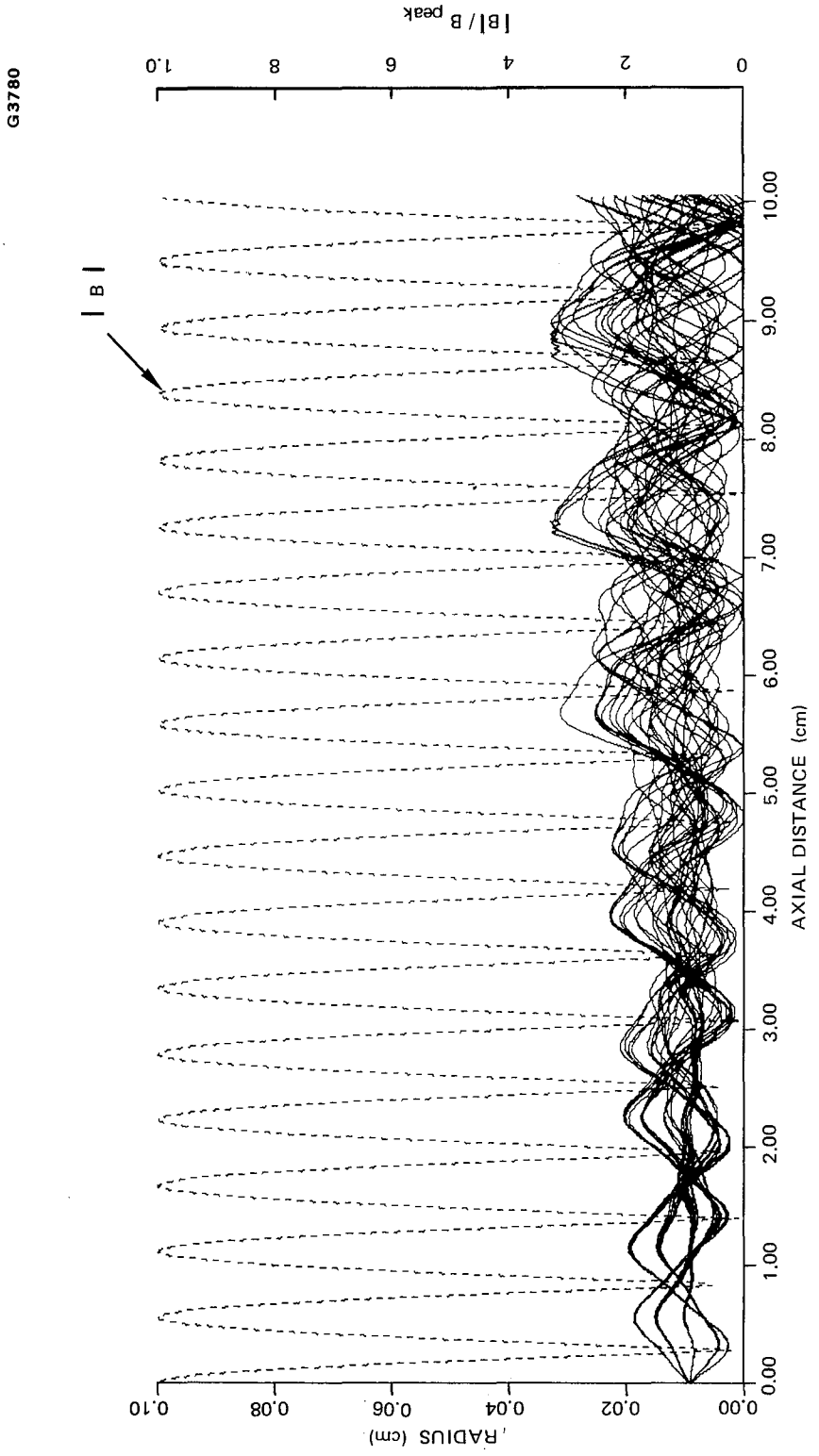

Figure 3-25 Edge trajectories of 32 disks modeling the electron beam in the output region of the 943H under saturation drive.

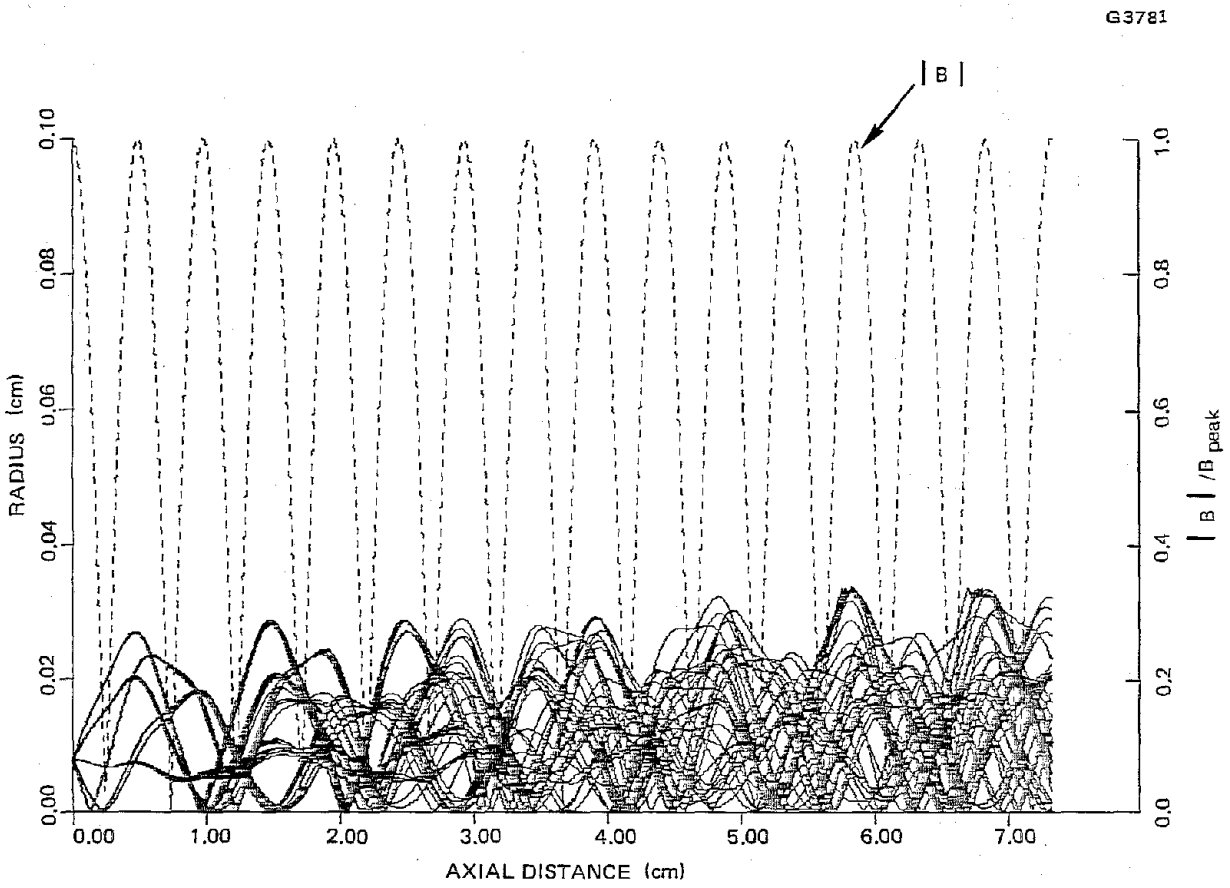

Figure 3-26 Edge trajectories of 32 disks modeling the electron beam in the output region of the 985H under saturation drive.

Table 3-10 summarizes the spent beam trajectory data for all four designs. The maximum trajectory slopes at the output of the interaction region have values between 0.07 and 0.08. An important function of the refocusing section which follows is to reduce the spread of trajectory angles. The electron energies in the spent beam range from about 0.65 to 1.08 of the initial value for the 42 GHz tubes and from 0.81 to 1.05 in the 85 GHz design.

3.4.2 Refocusing Design and Performance

The refocusing section accomplishes a controlled expansion of the spent beam, thereby decreasing the space charge forces, and a simultaneous reduction of the radial velocities of the electrons.[11] The particular scheme here adopted utilized two magnetic field regions, which, in an idealized form, achieves refocusing for two distinct energy groups.[12]

The idealized concept is illustrated in Figure 3-27. The main (uniform) focusing field is reduced in two steps. In the first section the field magnitude is chosen to allow the electrons with a specified energy in the lower part of the energy range to expand an appropriate amount. The length of this section is made one half of a scalloping wavelength to achieve parallel electron trajectories at the end. The field in the second section, is selected to maintain a parallel flow for the low energy electrons, while its length is determined by the axial distance at which electrons with a given energy in the upper part of the total energy range achieve parallel flow. These electrons therefore also execute a motion which is essentially one half of the natural scallop period in the field of the second section. Electrons with other than the two selected energies will not be perfectly refocused into axial flow but the deviations will be minor. (The half-wavelength two-step concept is somewhat analagous to a step transformer between waveguides of different heights.)

TABLE 3-10

PARAMETER SUMMARY OF COMPUTER RUNS USED TO GENERATE SPENT BEAM REPRESENTATION

Tube	942H	943H	944H	985H
Rms Field (T)	0.209	0.235	0.199	0.339
Initial Trajectory Slopes, ± dr/dz	0.024 0.015 0.0	0.024 0.015 0.0	0.024 0.015 0.0	0.06 0.04 0.0
Basic Efficiency (%)	14.0	15.3	17.0	5.08
Interception (%)	2.9	3.3	2.3	2.9
Final Slope, dr/dz:				
Minimum	-0.057	-0.050	-0.059	-0.083
Maximum	+0.075	+0.067	+0.068	+0.080
Beam Hole Radius (cm)	0.0315	0.0330	0.0300	0.0338

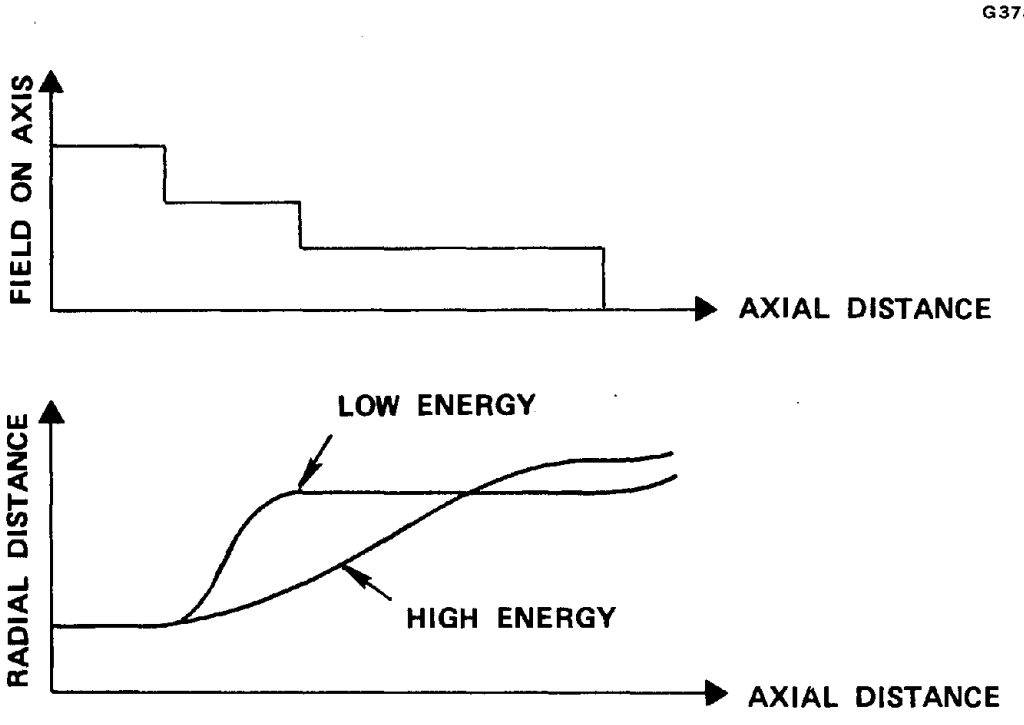

Figure 3-27 An idealized concept for the refocusing scheme used in the study.

In a PPM focused tube the natural way to implement a two-step design is with field reversals. The idealized performance of Figure 3-27 will then no longer be obtained, because the field transitions give additional radial impulses to the motion. Also, in a practical spent beam, the trajectories entering the refocusing field will have a range of angles with respect to the axis.

Figure 3-28 shows the calculated trajectories in a practical refocusing field for the 943H. The calculation is a continuation of the computer run in Figure 3-25, with the RF interaction switched off. The scale of the magnetic field plot has here been renormalized to the rms value of the main focusing field (rather than the peak value). The refocusing section was designed to expand the spent beam by a factor of about four, while providing an approximately parallel flow with a minimum range of trajectory slopes at the end. A similar plot for the 985H is reproduced in Figure 3-29.

Figure 3-30 summarizes the refocusing field design for all four tubes, while the performance data are given in Table 3-11. The magnetic field shapes assumed are generally achievable with permanent magnets, although they were generated by using superpositions of Molnar-Moster type field terminations[12,13] appropriate to solenoid fields. The inner face of the last pole piece, which is indicated in the figure and defines the length of the refocusing region, is located at the axial plane where the magnetic field is one half of the maximum value in the last refocusing section. A hole radius of about 0.3 cm was assumed in the output pole piece. With permanent magnents the field termination may have a small additional field reversal.

The point labeled number 3 in the figure defines the plane where the data on disk radii and trajectory slopes given in Table 3-11 were gathered. Of primary importance for the collector design is the beam size data (output disk radii) and the maximum trajectory slope, since

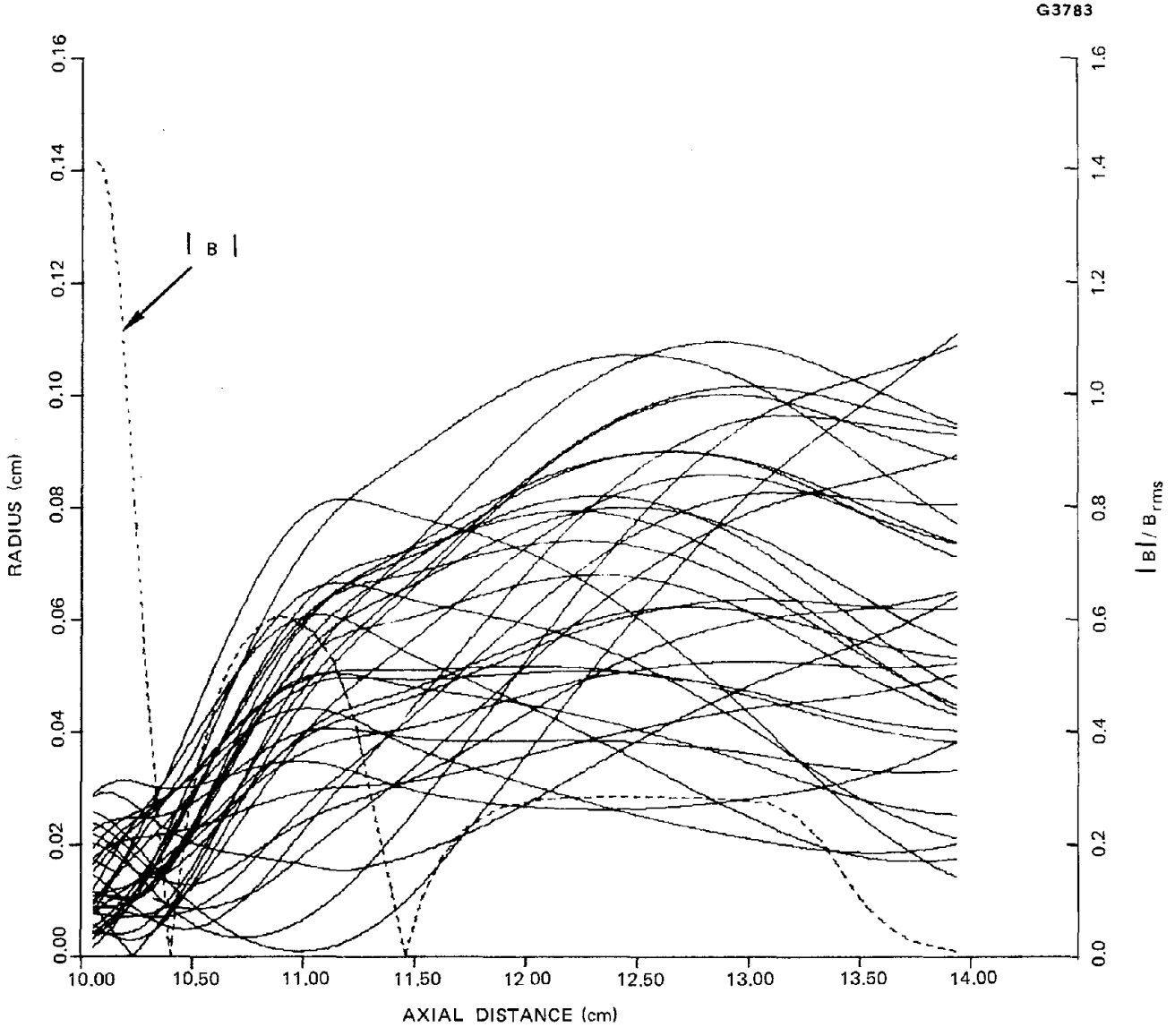

Figure 3-28 Disk edge trajectories of the spent beam in the refocusing field for the 943H.

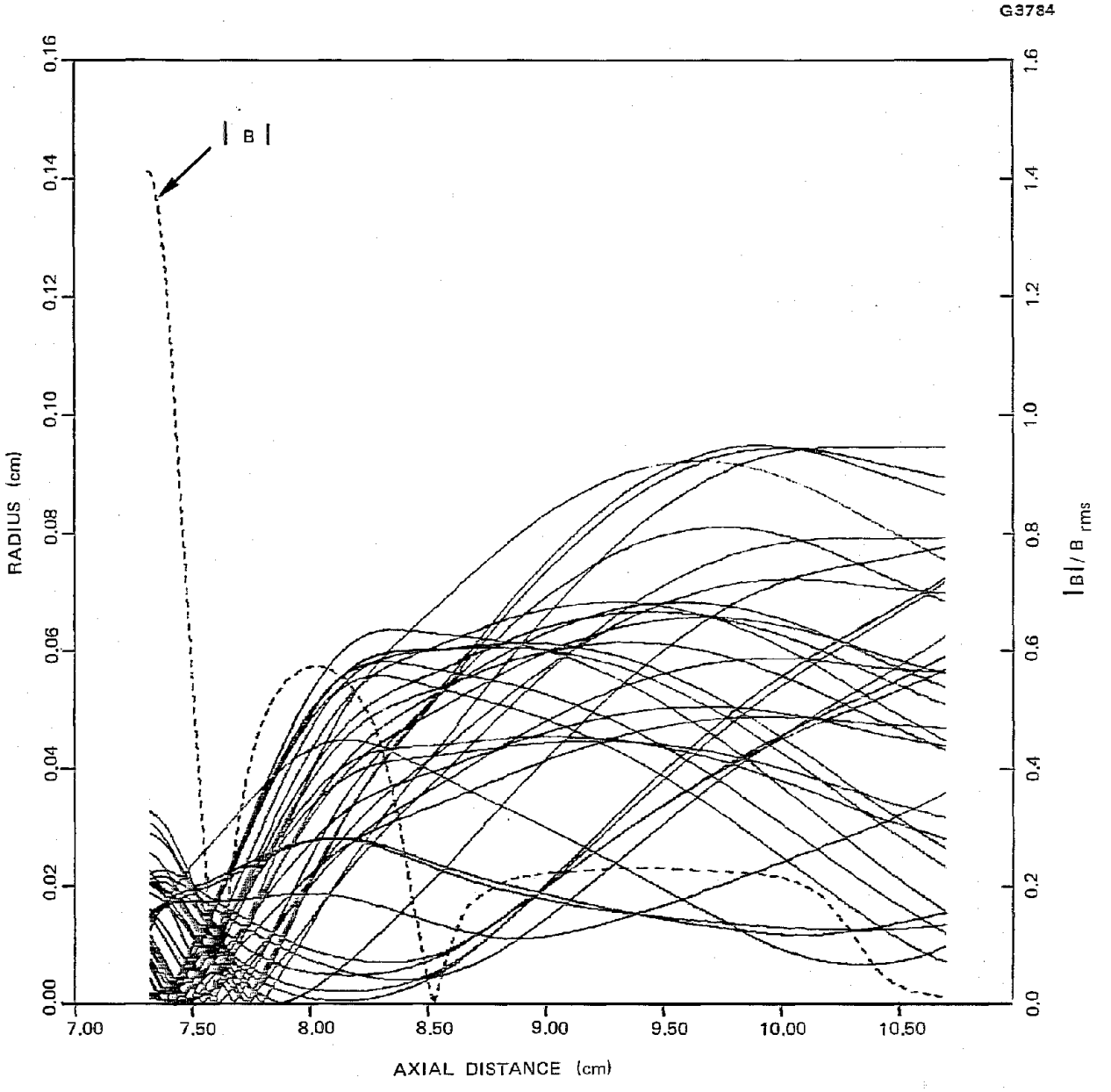

Figure 3-29 Disk edge trajectories of the spent beam in the refocusing field for the 985H.

G3785

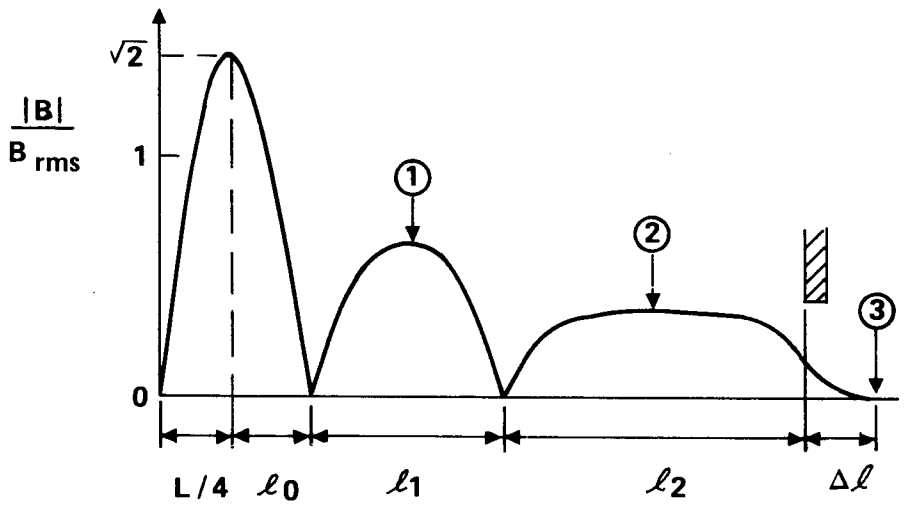

TUBE	942H	943H	944H	985H
L/4 (cm)	.266	.280	.267	.244
ℓ_0 (cm)	.325	.335	.325	.288
ℓ_1 (cm)	1.06	1.06	1.06	.920
ℓ_2 (cm)	1.95	1.95	1.95	1.78
$\Delta\ell$ (cm)	.52	.52	.57	.42
$\|B_1\| / B_{rms}$	.583	.605	.580	.575
$\|B_2\| / B_{rms}$	.250	.285	.260	.230
$\|B_3\| / B_{rms}$	.009	.009	.009	.010

Figure 3-30 Refocusing field design data.

TABLE 3-11

SUMMARY OF REFOCUSING PERFORMANCE DATA

Tube	942H	943H	944H	985H
Output Disk Radii:				
Max. Radius (cm)	0.113	0.109	0.098	0.094
Ave. Radius, r_{ave} (cm)	0.061	0.059	0.054	0.049
Output Traj. Slopes:				
Min.	-0.020	-0.026	-0.019	-0.026
Max.	+0.024	+0.032	+0.026	+0.026
Ave.	+0.003	-0.002	0.000	-0.003
Std. Deviation, $\sigma_{dr/dz}$	0.012	0.014	0.011	0.017
Statistical Performance:				
$r_{ave}(out)/r_{ave}(in) = R$	4.0	4.6	3.9	3.5
$\sigma_{dr/dz}(in)/\sigma_{dr/dz}(out) = S$	2.9	2.2	2.4	2.6
S/R	0.75	0.49	0.61	0.74

these will determine the collector apertures for a given beam current and electron energy distribution. Statistical performance data[14] have also been included, concerning the increase in the beam size, $r_{ave}(out)/r_{ave}(in) = R$ (where r_{ave} is the average disk radius), and the decrease in the standard deviation of the trajectory slope, $\sigma_{dr/dz}(in)/\sigma_{dr/dz}(out) = S$. The ratio S/R provides a measure of the intrinsic performance of the refocusing field. The larger this ratio is, the more effectively the radial velocies are quieted down with a given beam expansion. In the persent designs the ratio S/R is between one half to three quarters. It should also be noted, however, that the reference data on the spent beam before refocusing have been collected at the last peak of the regular PPM field. At the null planes of the axial field the beam tends to be smaller and have larger radial velocities. With such a choice of input reference the ratio S/R would generally be larger.

Figure 3-31 presents the electron energy distribution and disk data in histogram form for the 944H before and after refocusing. (The ratio S/R had an intermediate value of .61 in this case.) The ordinate represents the normalized current, so that the thickness of a histogram strip is proportional to the amount of charge left in the disk. The disks have been arranged in order of decreasing velocity, starting with the highest velocity disk placed along the X-axis. A smooth energy distribution curve has been obtained by joining the tip midpoints of adjacent strips. The general design criterion that was used in the refocusing design is exemplified by the plot of disk slopes after refocusing. The total range of slopes is small, centered around zero, and with no marked systematic groupings in value or systematic trends with energy. Such a design approach has been applied successfully in a 100 W TWT at 12 GHz.[15] In practice the final field magnitudes are fine-tuned empirically, and it is likely that a slope pattern that somewhat favors the positive slopes is actually produced for best overall collector performance.

BEFORE REFOCUSING

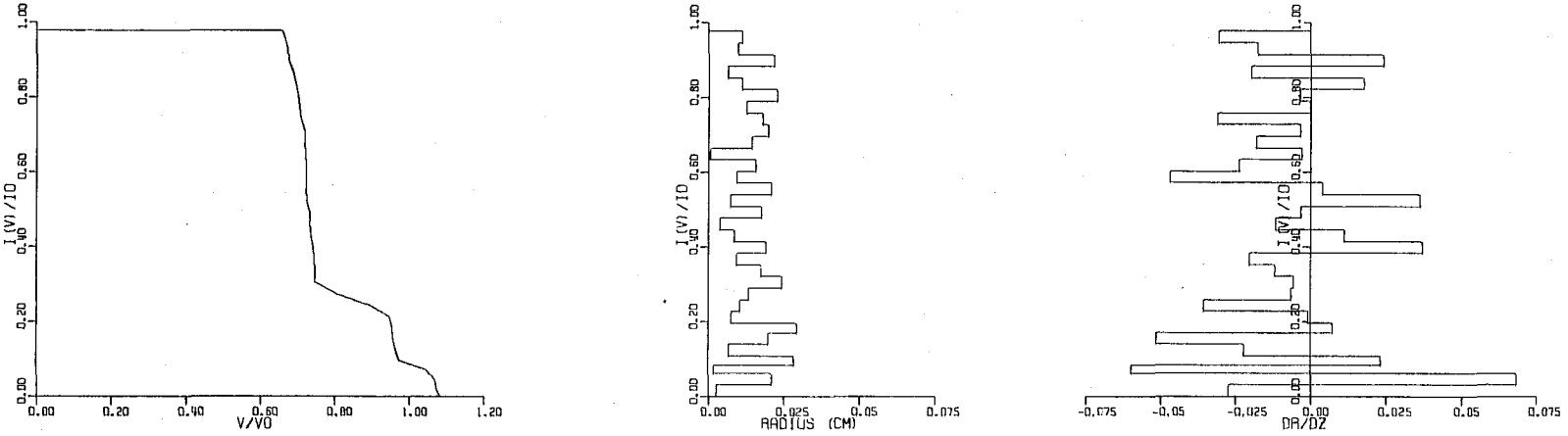

AFTER REFOCUSING

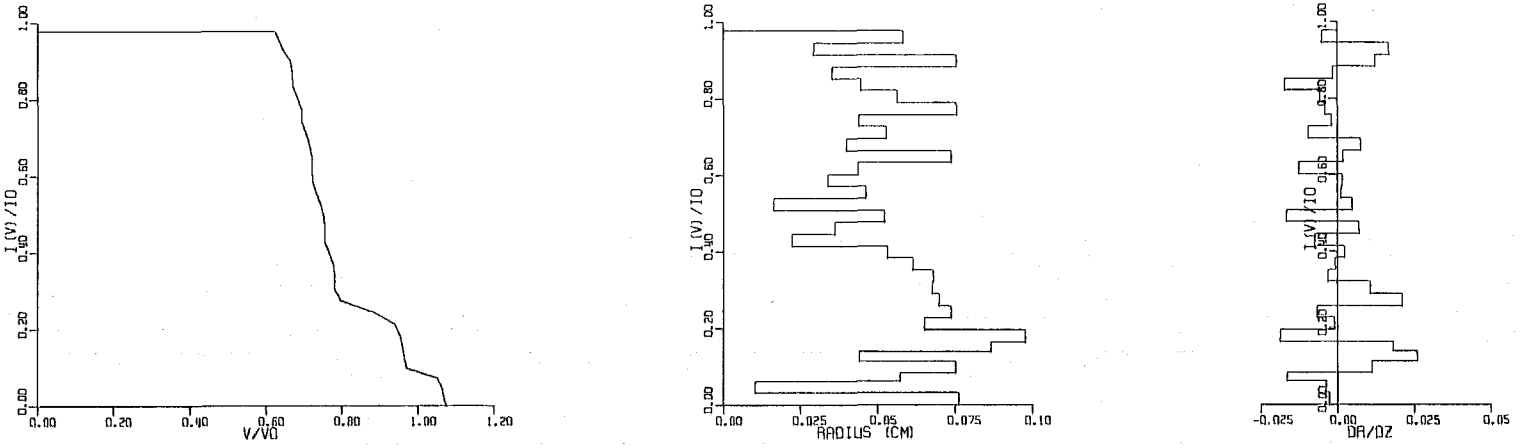

Figure 3-31 Electron disk data before and after refocusing for the 944H.

Figure 3-32 again shows the spent beam energy distributions before and after refocusing for the 944H, but replotted on the same graph for ease of comparison. It is observed that an energy exchange takes place between the slowest electrons and the intermediate electrons, with the former slowing down and the latter speeding up. Physically the reason for this is that, in the drifting bunched beam, the slow electrons fall behind and experience a retarding space charge force from the bunch ahead, while the opposite happens to the faster electrons. As a consequence of this energy exchange the first collector stage generally has to be operated with less depression to collect the slowest electrons whenever the beam has been allowed to drift long enough to disperse the RF bunching.

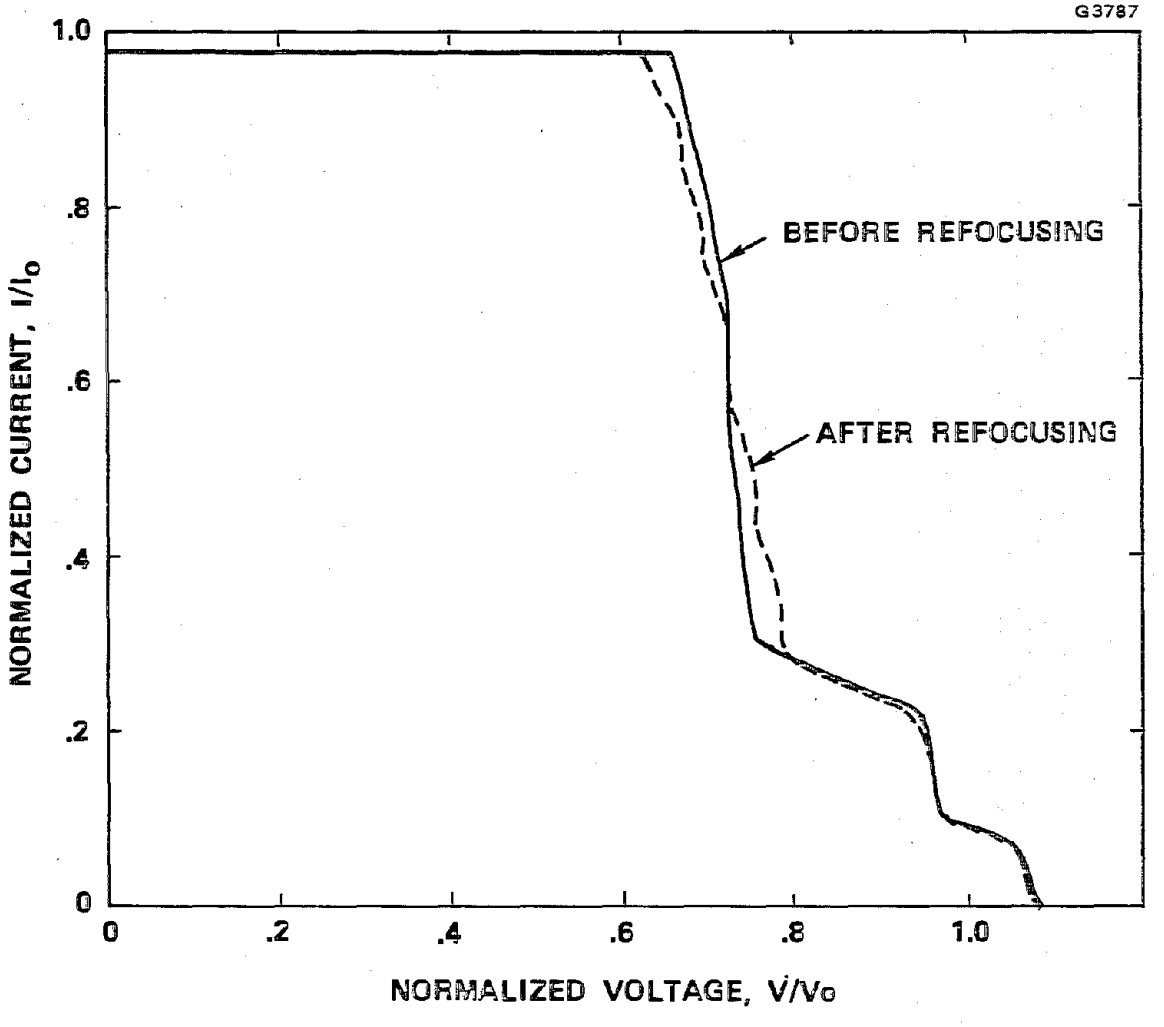

Figure 3-32 Spent beam energy distribution before and after refocusing for the 944H.

3.5 MULTI-STAGE DEPRESSED COLLECTOR

Multi-stage collectors possessing cylindrical symmetry and having three depressed elements, with a bucket as the last stage, were considered for the present TWTs.

The basis for the design, operation, and expected performance of any collector is the characteristics of the electron beam that it receives. A major consideration in assigning operating voltages and evaluating projected performance is given to the energy distribution of the beam, while the detailed electrode design also depends on other properties like beam size, perveance, and electron trajectory angles.

3.5.1 Collector Operation and Performance

The energy distributions used in the collector designs were calculated with the one-dimensional large signal program. An example is shown in Figure 3-33 for the 944H at midband. All the electrons in this theoretical beam could in principle be collected at a depression voltage of at least 68 percent of the cathode potential. The energy distribution of the actual beam will differ mainly because of beam interception on the RF circuit with an attendant power loss. Also, as was noted in the previous section, the drift in the refocusing region will cause an internal energy exchange to take place between the slow and intermediate velocity electrons. For these reasons the theoretical distribution calculated with the one-dimensional program is replaced by a practical one in which these effects are taken into account.

For the 944H at midband the anticipated practical distribution is plotted in Figure 3-34 with the theoretical graph also displayed for comparison. A beam interception of 5 percent of the cathode current has been assumed. Part of this is DC interception (2 percent) and

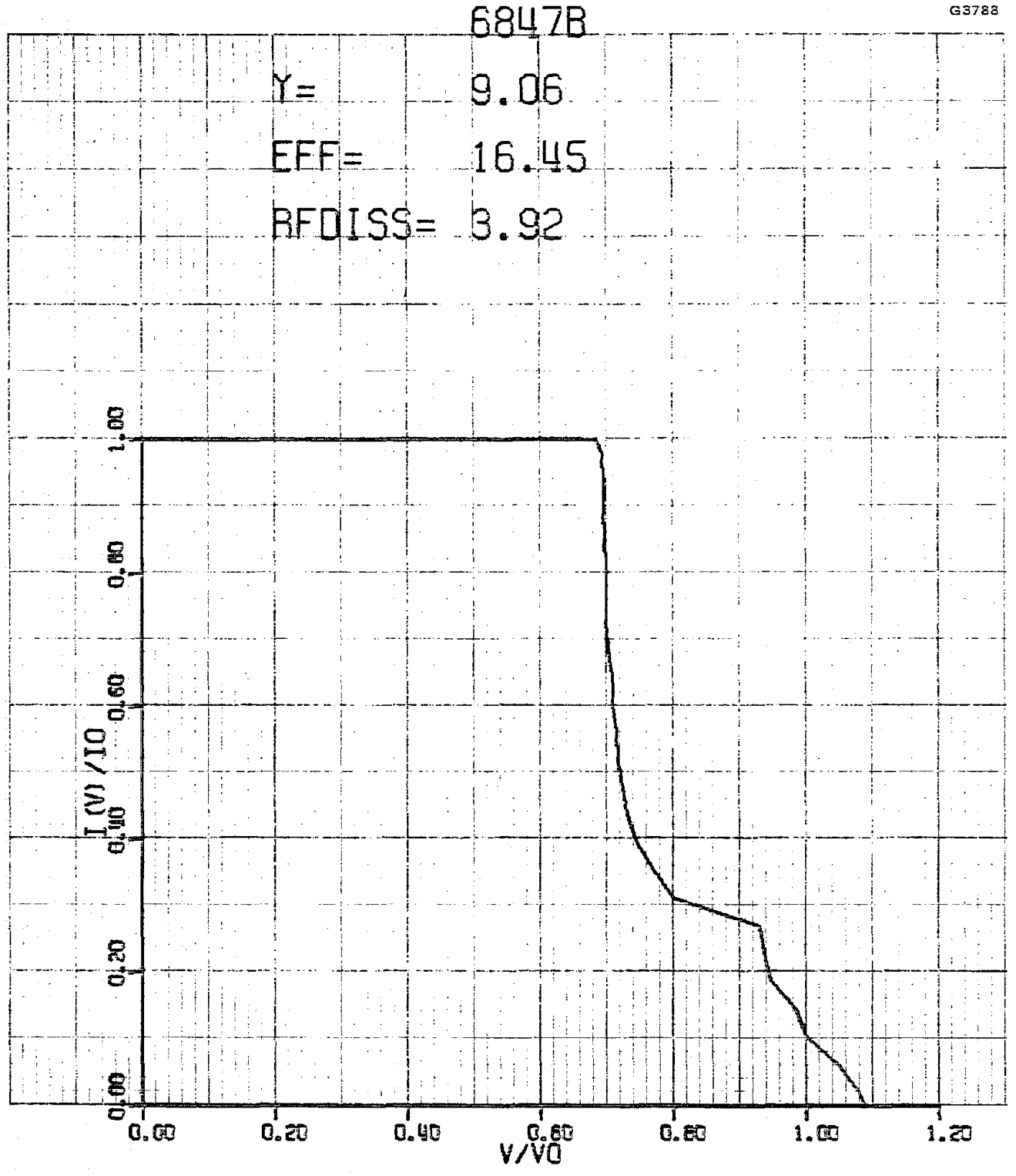

Figure 3-33 Spent beam energy distribution for the 944H at midband calculated with the one-dimensional large signal program.

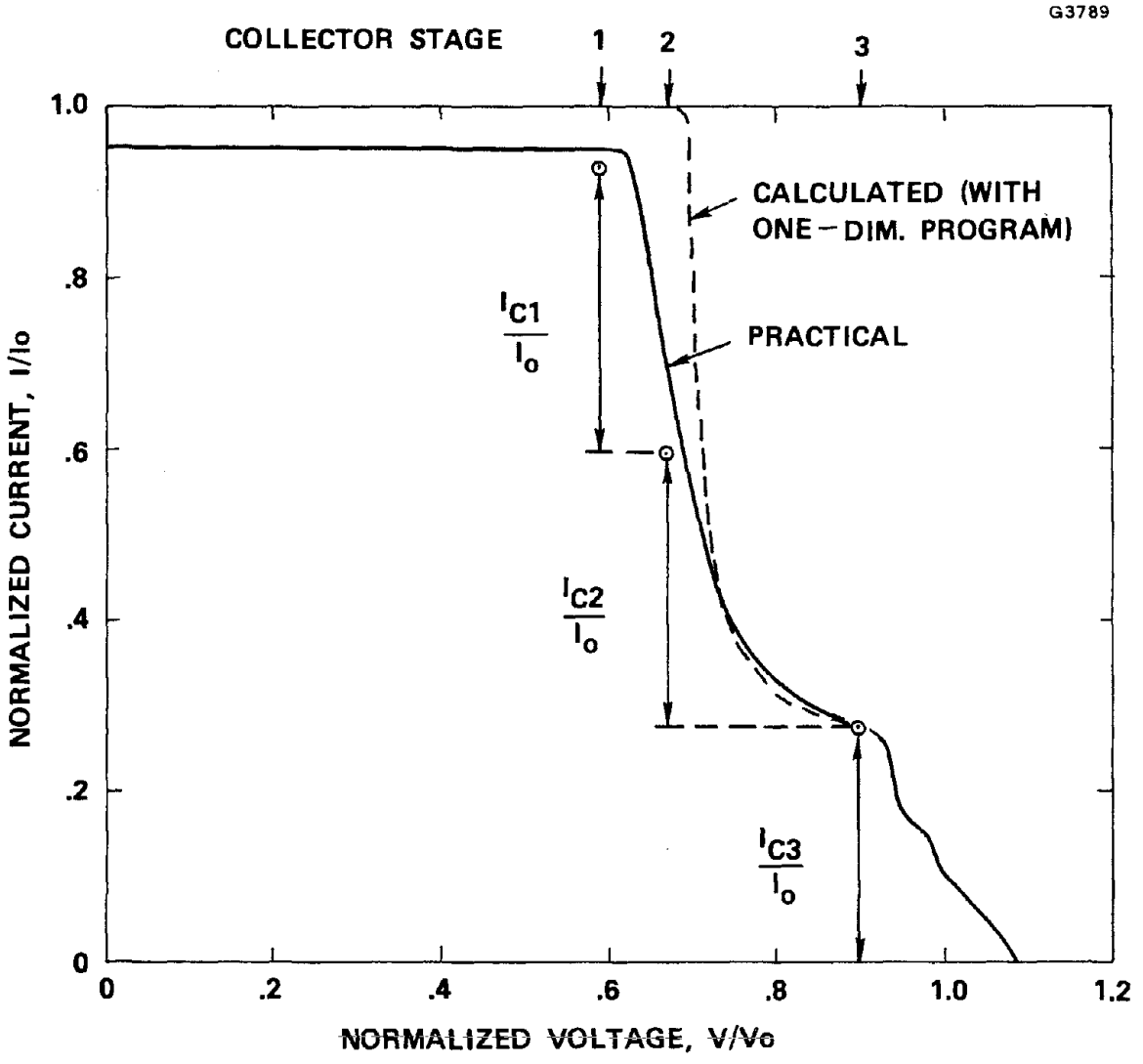

Figure 3-34 Practical spent beam energy distribution for the 944H at midband, and data points defining collector operation.

the rest is due to RF defocusing. From this the top boundary of the practical curve is established. The rest of the distribution has been drawn in using the theoretical graph as a guide. Since the total area under the curve is directly related to the kinetic power in the spent beam, the area must be reduced to account for the power absorbed by the circuit due to beam interception. This power has been estimated by assuming the DC interception occurs at the initial electron velocity in the beam, while the part due to RF defocusing involves electrons whose energy on the average has been reduced by 15 percent. Furthermore, the slope of the drop-off from the plateau has been made less steep to account for the energy exchange taking place in the refocusing region (note Figure 3-32). Finally, practical experience[15] has indicated that the high energy part of the distribution is generally predicted quite well.

Included in Figure 3-34 are data points defining the operation of a practical collector with three depressed stages, again using practical experience as a guide. With an ideal collector the data points would lie on the energy distribution curve. The actual points lie below because of imperfect performance, although the last bucket stage acts almost like an ideal collector. A total backstreaming current of two percent has been assumed.

The collector voltages have been partly selected by considering the energy distributions at other frequencies in the band. Figure 3-35 shows a comparison of the calculated curve at midband frequency (42.25 GHz) with the ones obtained at 400 MHz on either side. A lowering of the minimum electron energy as the frequency is increased is typical for these devices, and generally the depression of the first stage (59 percent for the 944H) is established at the high frequency end.

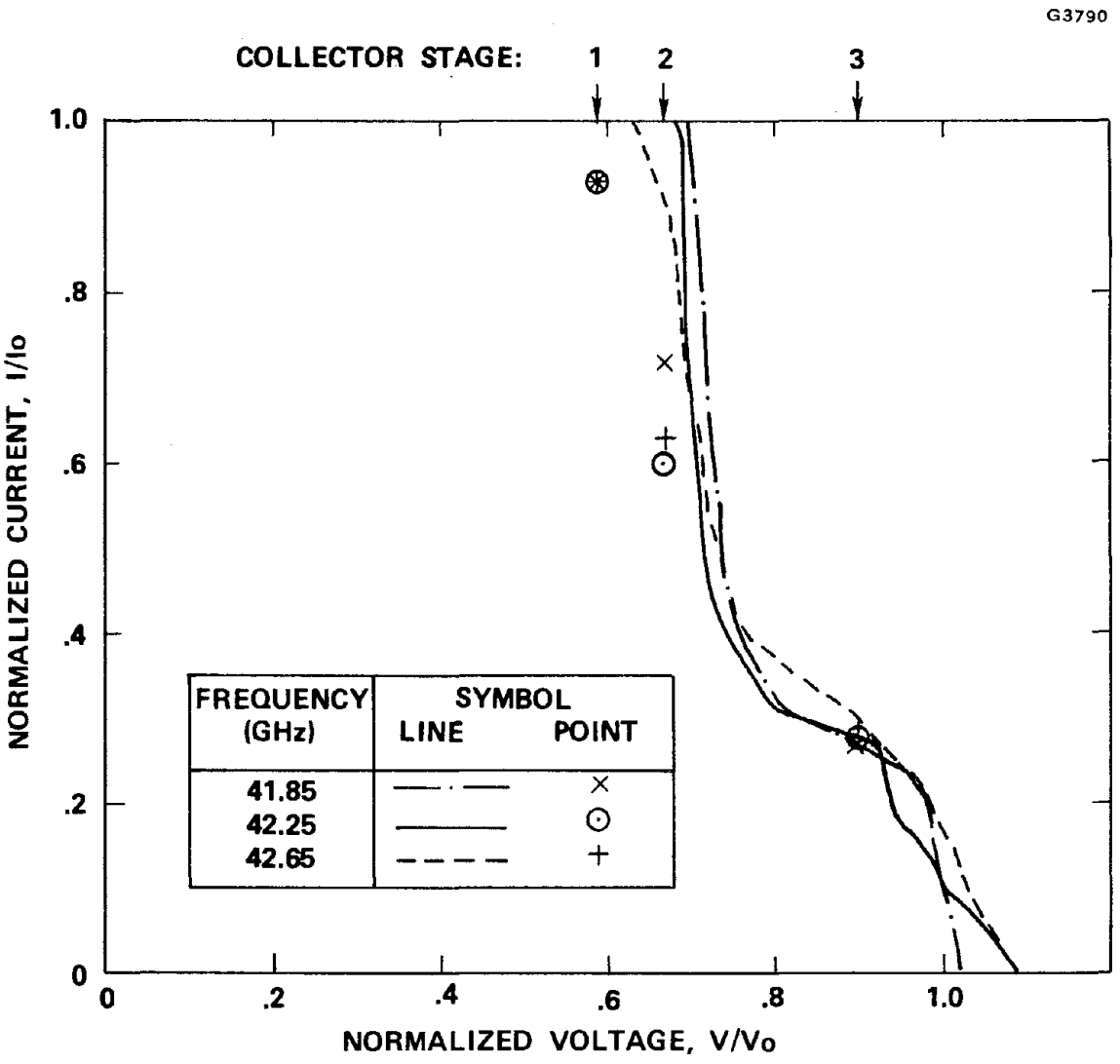

Figure 3-35 Spent beam energy distributions calculated for the 944H at three frequencies, and data points defining collector operation.

Table 3-12 details the collector performance at all three frequencies, according to the operating points that have also been plotted in Figure 3-35. The collector raises the efficiency from 15 - 16 percent to 46 - 47 percent, or a factor of three. Assuming a heater power of 5 W the overall efficiency is reduced by one percentage point. Figure 3-36 is a graph of the efficiency performance versus frequency. The minimum efficiency over the band 42 - 42.5 GHz is 45.4 percent.

Table 3-13 summarizes the collector operation of all four tube designs. The performance characteristics of the three 42 GHz devices are very similar to each other. The first and the last collector electrodes are typically depressed 60 percent and 90 percent respectively. With a heater power of 5 W, the minimum overall efficiencies range from 42 to 45 percent. In the 85 GHz design the first stage is depressed to 80 percent while the last stage is operated at 96 percent of the cathode voltage. The collector in this case improves the efficiency by a factor of five, resulting in an overall efficiency of 25 percent minimum over the band.

An evaluation of the collector efficiency (defined as the ratio of recovered power to incident spent beam power) for the 944H at midband can be made from the information presented in this section. The result is 88.1 percent. Similar values were obtained for the other two 42 GHz tubes. For the 985H the collector efficiency was 91.3 percent. These performance estimates are likely to be on the low side. A closely related W-band TWT at Hughes EDD, with a basic saturated efficiency of 9.5 percent, has demonstrated a collector efficiency of 92.0 percent. The collector in this case had two depressed electrodes, while beam refocusing was not utilized.

Although the collector performance estimates presented here have been given without direct reference to the electrode design, the two are

TABLE 3-12

COLLECTOR PERFORMANCE DATA FOR THE 944H AT THREE FREQUENCIES

Frequency (GHz)	41.85	42.25	42.65
Net Output Power (W)	101	106	101
Collector Depression (%)			
Stage 1	59	59	59
Stage 2	67	67	67
Stage 3	90	90	90
Collector Current (%)			
Stage 1	21	33	30
Stage 2	45	32	34
Stage 3	27	28	29
Body Current (%)	7	7	7
Basic Efficiency (%)	15.2	15.9	15.2
Depressed Efficiency (%)	45.8	46.9	45.5
Overall Efficiency (%)*	44.7	45.9	44.5

*Including 5 W heater power

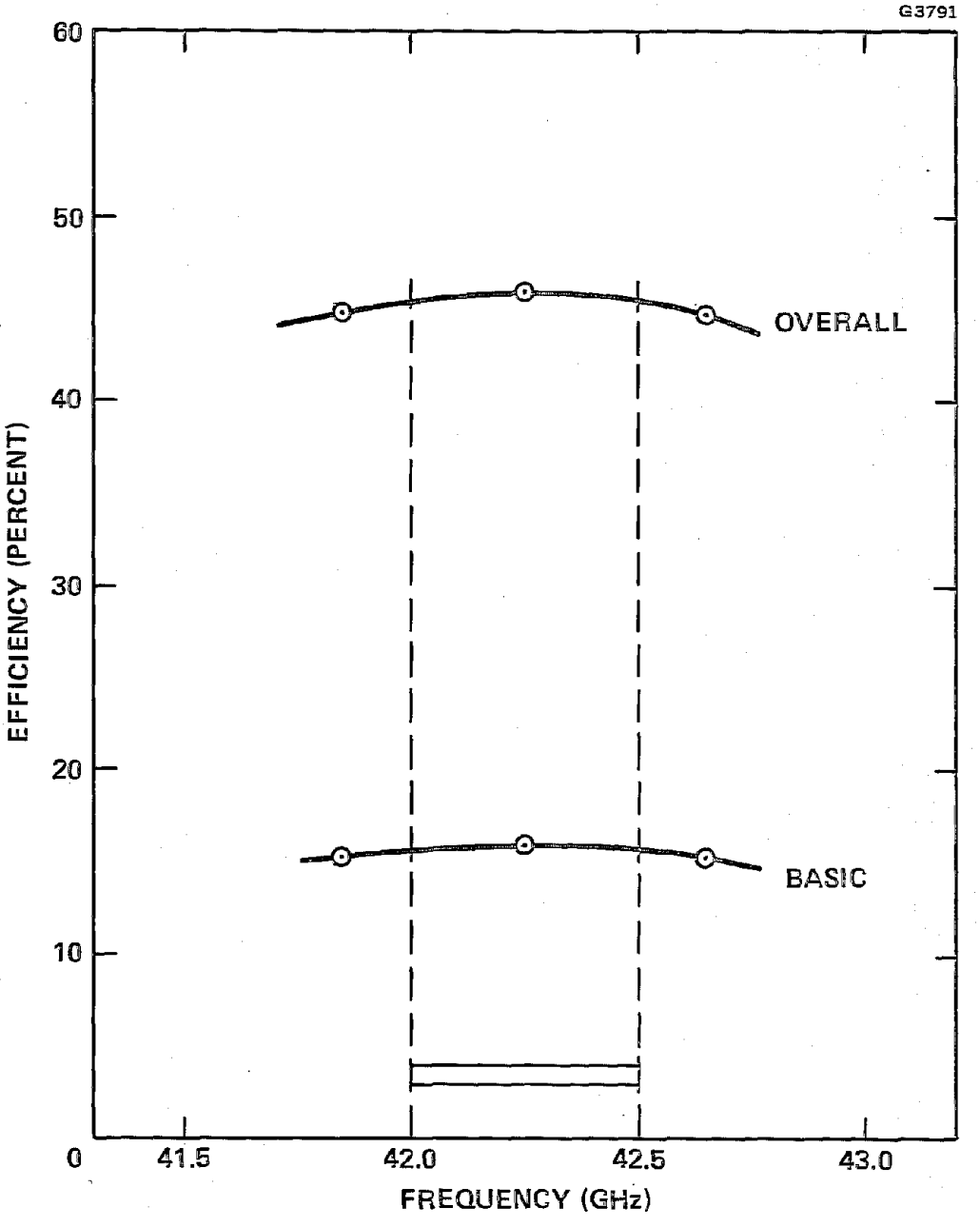

Figure 3-36 Basic and overall efficiency of the 944H vs frequency.

TABLE 3-13

SUMMARY OF COLLECTOR OPERATION AND OVERALL EFFICIENCY
FOR ALL FOUR TUBE DESIGNS

Tube	942H	943H	944H	985H
Collector Depression (%)				
Stage 1	61	60	59	80
Stage 2	69	68	67	86
Stage 3	92	90	90	96
Collector Current at f_o (%)				
Stage 1	29	31	33	34
Stage 2	39	37	32	28
Stage 3	25	25	28	30
Body Current (%)	7	7	7	8
Net Basic Efficiency at f_o (%)	14.4	16.0	15.9	5.5
Overall Efficiency at f_o (%)*	44	47	46	27
Min. Overall Efficiency (%)*	42	45	45	25

*Including 5W heater power

evidently closely related. For the present study the type of collector that was assumed has been evaluated experimentally on devices whose characteristics are sufficiently similar to the TWTs being considered to permit realistic projections to be made.

3.5.2 Collector Electrode Design

The detailed electrode design is carried out with an electron trajectory computer program,[8] using different electrode shapes until satisfactory performance is obtained. The program evaluates the potential everywhere in the collector region, as determined by the exact electrode configuration and potentials, and traces out discrete electron trajectories. Each trajectory (ray) is assigned an appropriate amount of current. The effect of space-charge is taken into account by an iteration procedure. A plot of the electron trajectories and equipotentials, for a given collector geometry and electrode voltages, reveals how well the collector functions are being performed.

The analysis utilized the electrode voltages and the characteristics of the beam entering the collector as derived in preceding sections. The electron beam is simulated by several rays over the beam cross-section, with each ray corresponding to a ring of charge in a cylindrically symmetric system. The energy distribution of the spent beam is approximated by a number of discrete energy groups, each carrying a suitable amount of current.

Figure 3-37 shows calculated electron trajectories and equipotentials in a collector for the 943H. The spent beam has been represented by 8 energy groups of 4 trajectories each. A number of test trajectories, which do not contribute to the space charge, have also been injected at selected energies and angles. The maximum trajectory slope at the entrance is $dr/dz = 0.03$, or an angle of 1.7°.

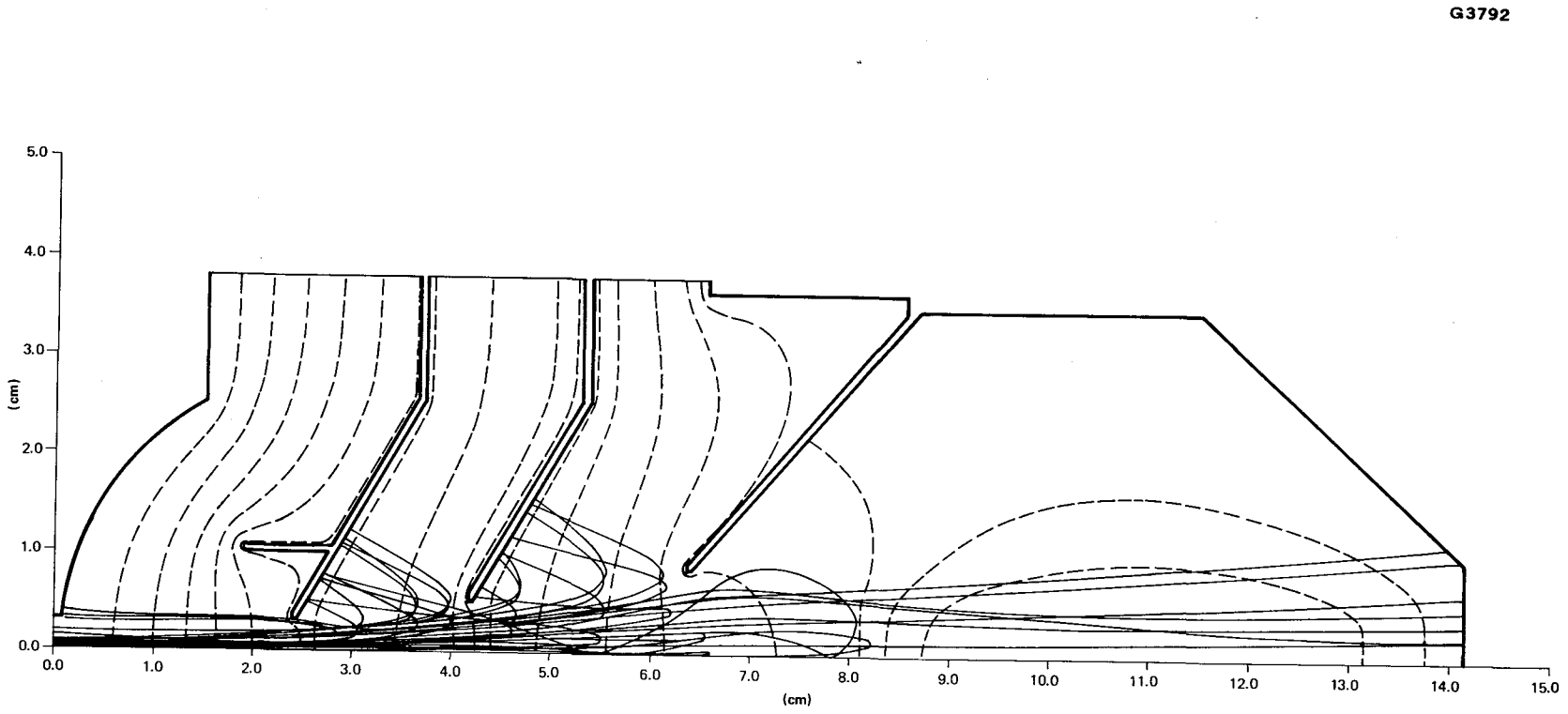

Figure 3-37 Electron trajectories and equipotentials in a three-stage collector for the 943H.

The general performance appears good, although some backstreaming occurs. Part of the backstreaming is inevitable, being characteristic of all cylindrically symmetric electrostatic collectors, and arising from electrons which are injected with zero angle very close to the axis, or with somewhat negative angles off the axis. A second source of backstreaming is the focusing action that occurs at the entrance to the last bucket stage. It has an adverse effect only on those electrons which do not quite have enough energy to penetrate all the way into the last stage.

All of the intermediate-energy electrons are intercepted on the far-side of the collector elements. At these surfaces the secondary electrons are prevented from escaping by the depression field. In the last stage a potential depression region due to space charge tends to deflect secondary electrons back to the bucket walls. The presence of this depression region is indicated by the equipotential "bubbles" in the interior of the bucket.

A special cylindrical shield has been incorporated at the front end of the first depressed element. Its purpose is to shape the equipotential lines at the aperture of the first stage. To explain its beneficial effect in the present collector, it will first be noted that the depression potentials have been chosen at 60, 68, and 90 percent of the cathode voltage for the three stages respectively. Since the physical spacing of the electrodes is approximately uniform, the potential gradient between the first stage and ground is much larger than between the first and second elements. This has the effect of pushing some equipotential surfaces through the aperture of the first stage. The resulting concave surface is associated with an electric force on the electrons which is directed radially inward. It produces an undesirable focusing effect that is particularly strong on the slow electrons, whereas ideally, these electrons should be deflected outward to be

collected on the first stage. The cylindrical protrusion on this electrode pushes the region of strong potential gradient away from the aperture so that the focusing effect is significantly reduced. Thus in Figure 3-37 there are two low energy trajectories, which turn around at the axial coordinate plane of 3 cm, that are collected at the first stage. Without the electrode modification, a calculation showed that these electrons would stream back through the aperture. The modification may also be described as a method of compressing the region of retarding field that is not needed for velocity sorting in a manner which retains the desireable features of the refocused beam, without creating a strong electrostatic lens that would perturb the subsequent velocity sorting in the collector.

In the final collector design for the 943H the shield was increased by 2 mm in length over that shown in Figure 3-37. The same collector configuration worked well for the other two 42 GHz tubes also. The main noticeable difference for the 944H was that the space charge depression in the bucket was reduced because of smaller beam perveance.

The spherical shape of the ground potential has no electrical significance in the present designs. For diagnosis of the collector performance it is useful to have an isolated electrode at body potential by which most of the backstreaming current can be measured. If such an electrode is supported some distance away from the collector base, the thermal power due to backstreaming current that is transferred to the base by conduction is reduced. The round shape is one way of accomplishing this.

The final collector design for the 985H is presented in Figure 3-38. In this case the first stage is depressed 80 percent, while the last two stages are held at 86 and 96 percent of the cathode potential.

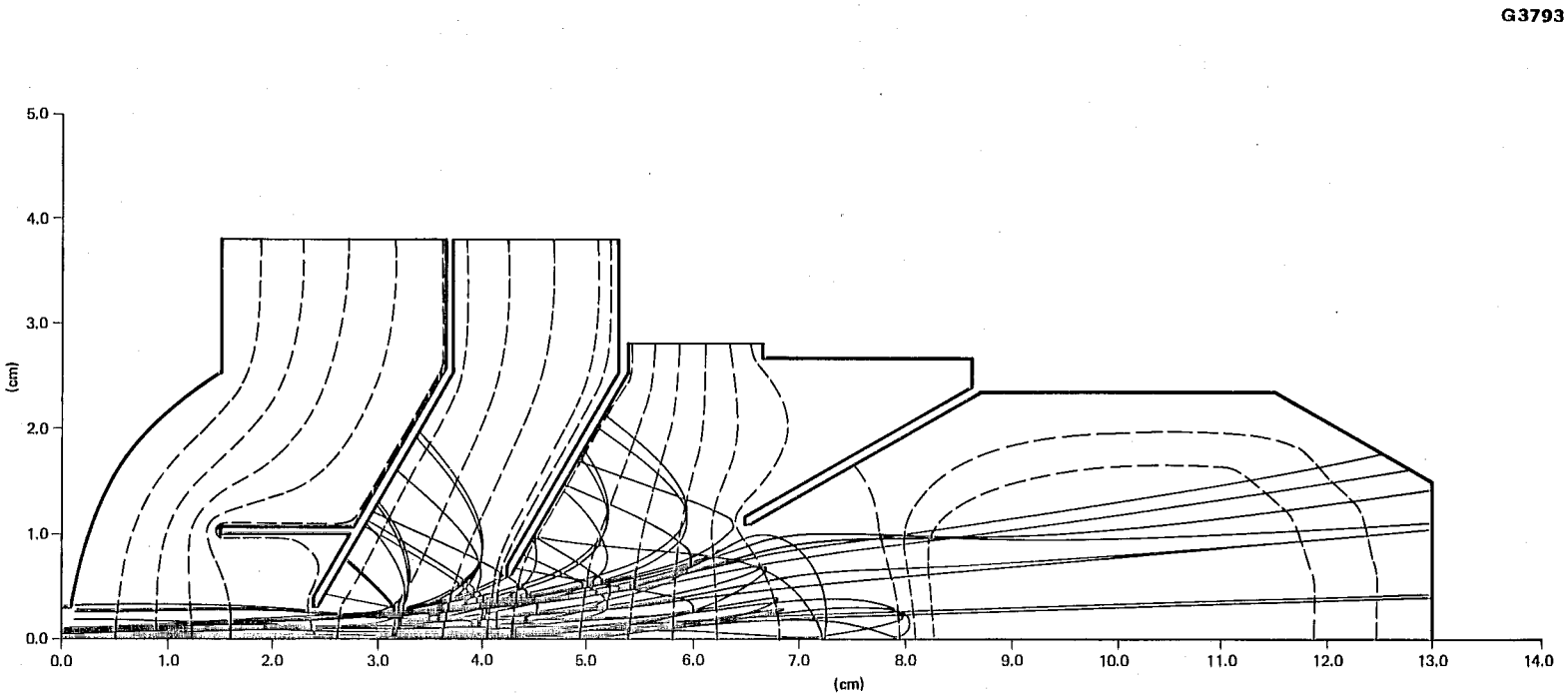

Figure 3-38 Electron trajectories and equipotentials in the collector design for the 985H.

The potential gradient between the first stage and ground is in this case even larger compared to the gradient between the later stages than was the case in the collectors for the 42 GHz tubes. Consequently, the cylindrical shield on the first stage is longer. The strongly-depressed operating voltage of the last stage results in a high space charge density inside the bucket because of the slowly moving electrons. A smaller bucket diameter will then still provide significant potential depression due to space charge.

The operation of the 985H collector was also checked with a DC beam, for which maximum current enters the bucket and a maximum space charge depression is produced. The computer-generated plot for this case is reproduced in Figure 3-39. It indicates good performance despite a depression voltage on the bucket of 96 percent.

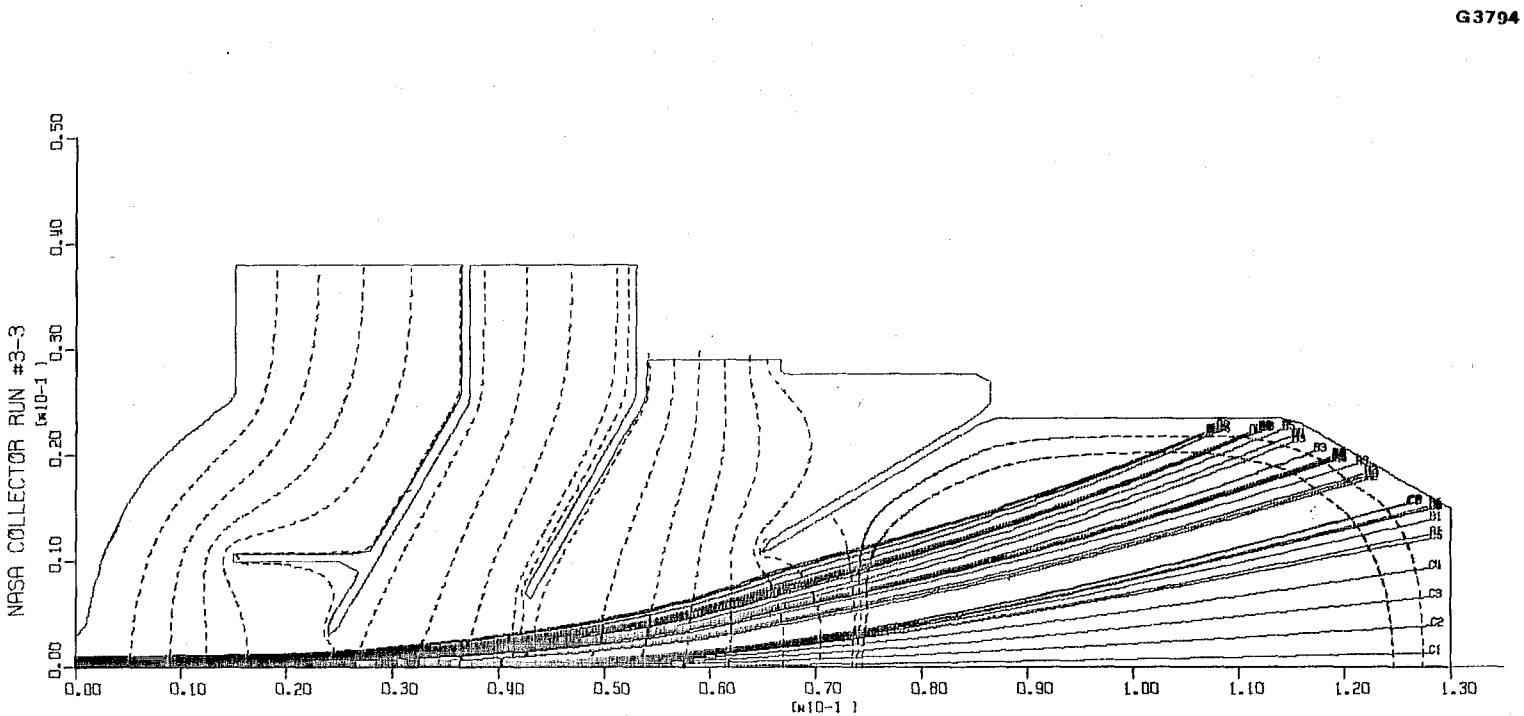

Figure 3-39 Electron trajectories and equipotentials in the 985H collector with no RF drive.

3.6 RF WINDOWS

RF windows were designed for the three frequency bands required to accommodate the four TWT types. Each window is comprised of a ceramic block with compensating irises. Similar windows have been employed successfully on many Hughes millimeter wavelenth TWTs.

Figure 3-40 is a photograph of a typical window assembly and its component parts. These rugged assemblies use a one half wavelength thick beryllia ceramic block conforming to the inside dimensions of the waveguide. The edges of the beryllia block are metalized using the conventional molybdenum-manganese technique. It is then brazed into a short "Elkonite" waveguide section. Elkonite is a readily available material of Mallory Inc., principally employed in the manufacture of electrodes for use in electric discharge machining (EDM). This material consists of a copper filled tungsten matrix. Tungsten has a coefficient of thermal expansion less than that of beryllia while the thermal expansion coefficient of copper is greater than that of beryllia. By employing the proper proportions of these two metals (i.e., tungsten and copper), a composite material with a coefficient of thermal expansion exactly matching that of beryllia can be produced. Thus, any tendancy toward ceramic fracture due to differential thermal expansion during brazing is eliminated. The Elkonite waveguide section and beryllia block comprise a subassembly which resides between the compensating irises. The subassembly is subsequently brazed to properly flanged adjoining waveguide sections with the irises simultaneously installed at the junctions.

E1101

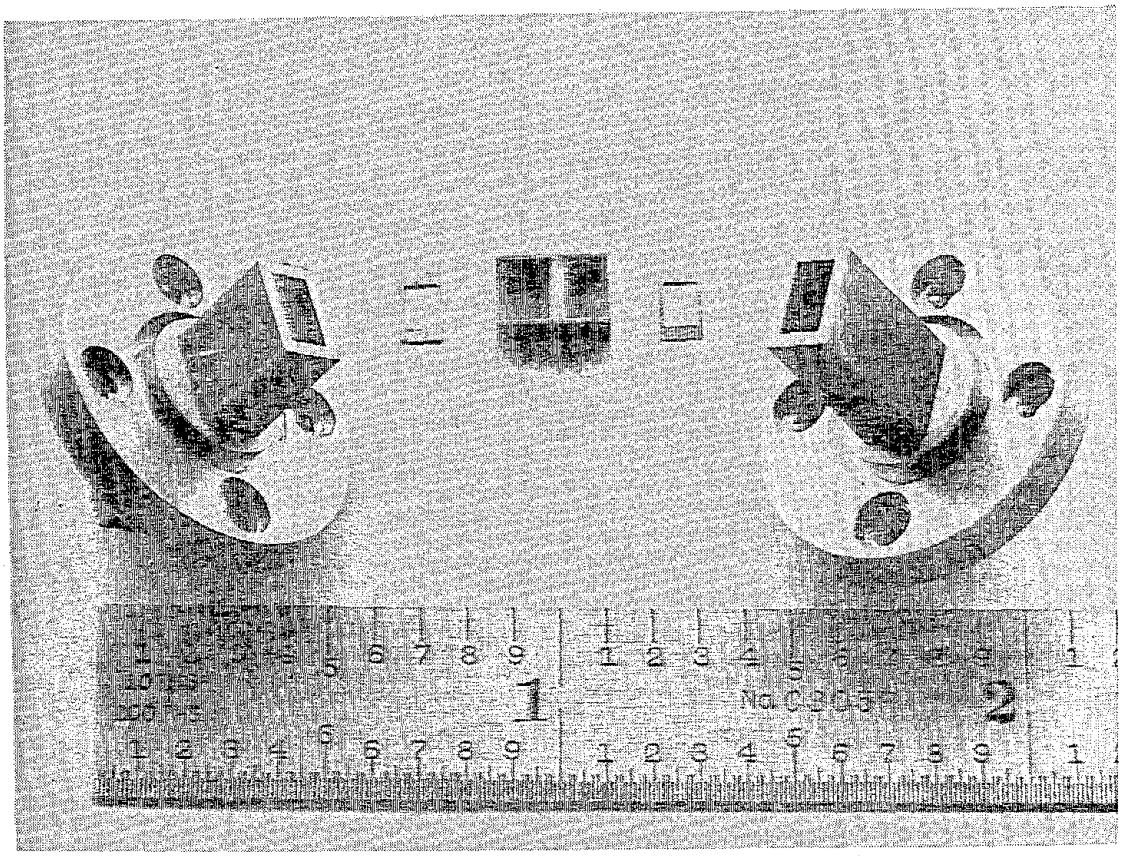

Figure 3-40 Millimeter wavelength RF window of metal-ceramic construction.

Figure 3-41 shows an improved and simplified version of the block window. Circular geometry on the outside surfaces of the waveguide and iris portion of the window is employed. This has resulted in greatly simplified component fabrication with no deterioration in the quality of the assembled window.

Figures 3-42, 3-43 and 3-44 show the computed reflectance properties of the windows. The window of 3-42 was designed for the input and output RF ports of the 942H and 943H. Figure 3-43 and 3-44 are for the 944H and 985H respectively. Table 3-14 summarizes window dimensions.

3.7 WAVEGUIDE TO CIRCUIT TRANSITION

Figure 3-45 shows a waveguide to circuit transition. It consists of two components, a stepped transformer and a hybrid cavity.

The stepped transformer provides a smooth transition from full height waveguide to a narrower height which is compatible with cavity dimensions. To achieve this transition, four steps are employed in the well-known Chebyshev configuration. An available computer program provides a rapid solution to the problem of step design. The transformer design provided by the computer does not generally require empirical adjustment after fabrication. Critical stepped transformer dimensions are indicated on Figure 3-45 with letter designations. These dimensions are summarized in Table 3-15 for all tube types.

The stepped transformer is attached at its narrow height extremity to a hybrid cavity. The purpose of this cavity is to effect a mode transition from waveguide TE_{10} mode to the coupled-cavity TM_{01} interaction mode. Design of the hybrid cavity is largely an experimental exercise. It is convenient to perform the experimental procedures at a scaled frequency (C-band). Three different geometries of the hybrid cavity

E1279

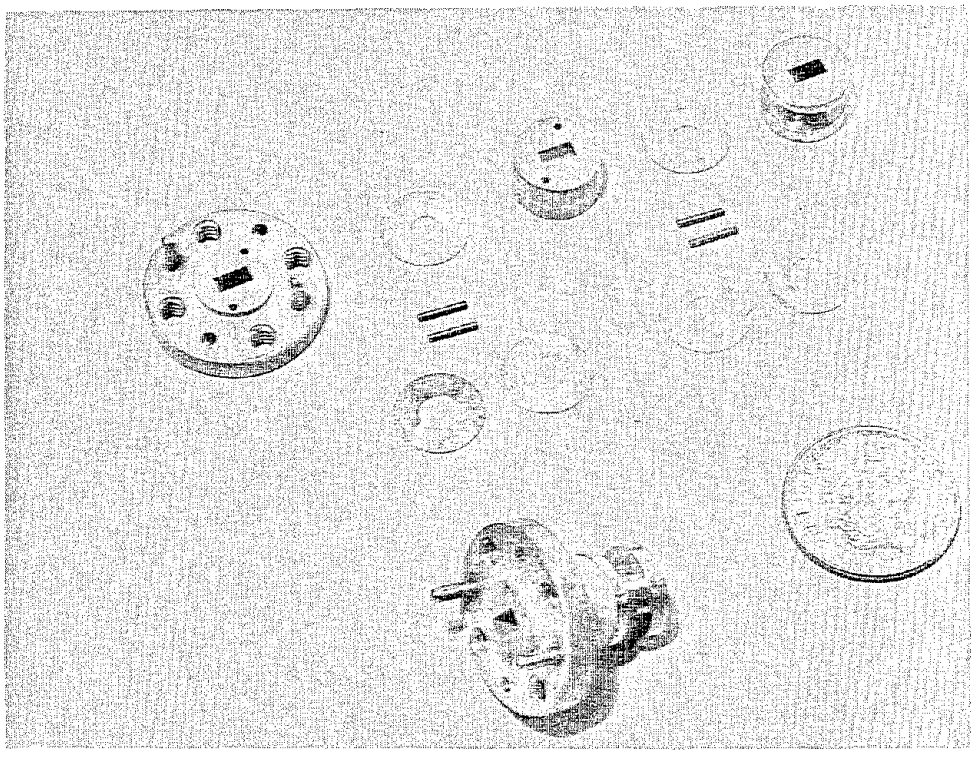

Figure 3-41 Improved, simplified version of the RF block window.

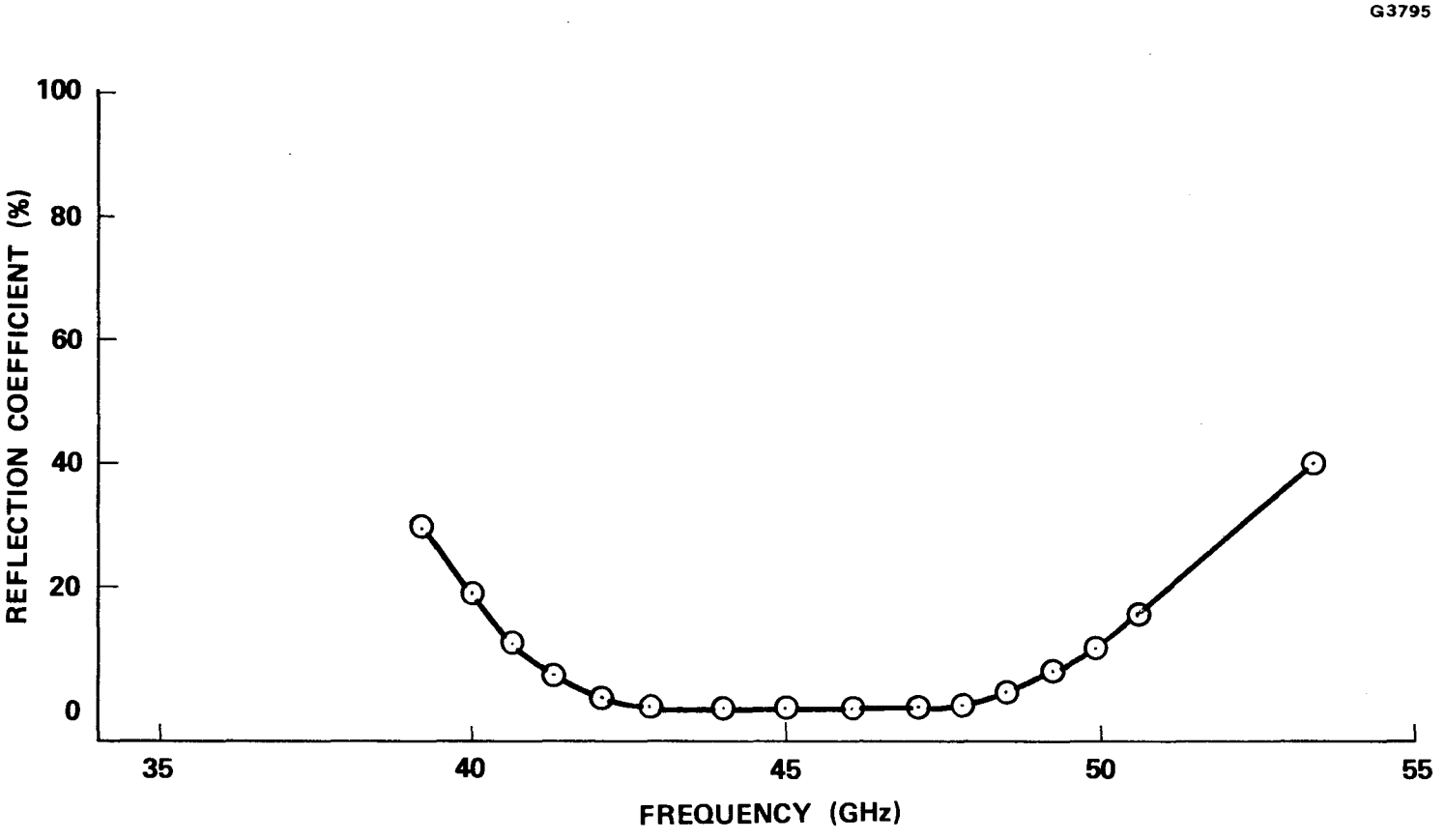

Figure 3-42 Reflection coefficient vs frequency (calculated) for 942H, 943H RF window.

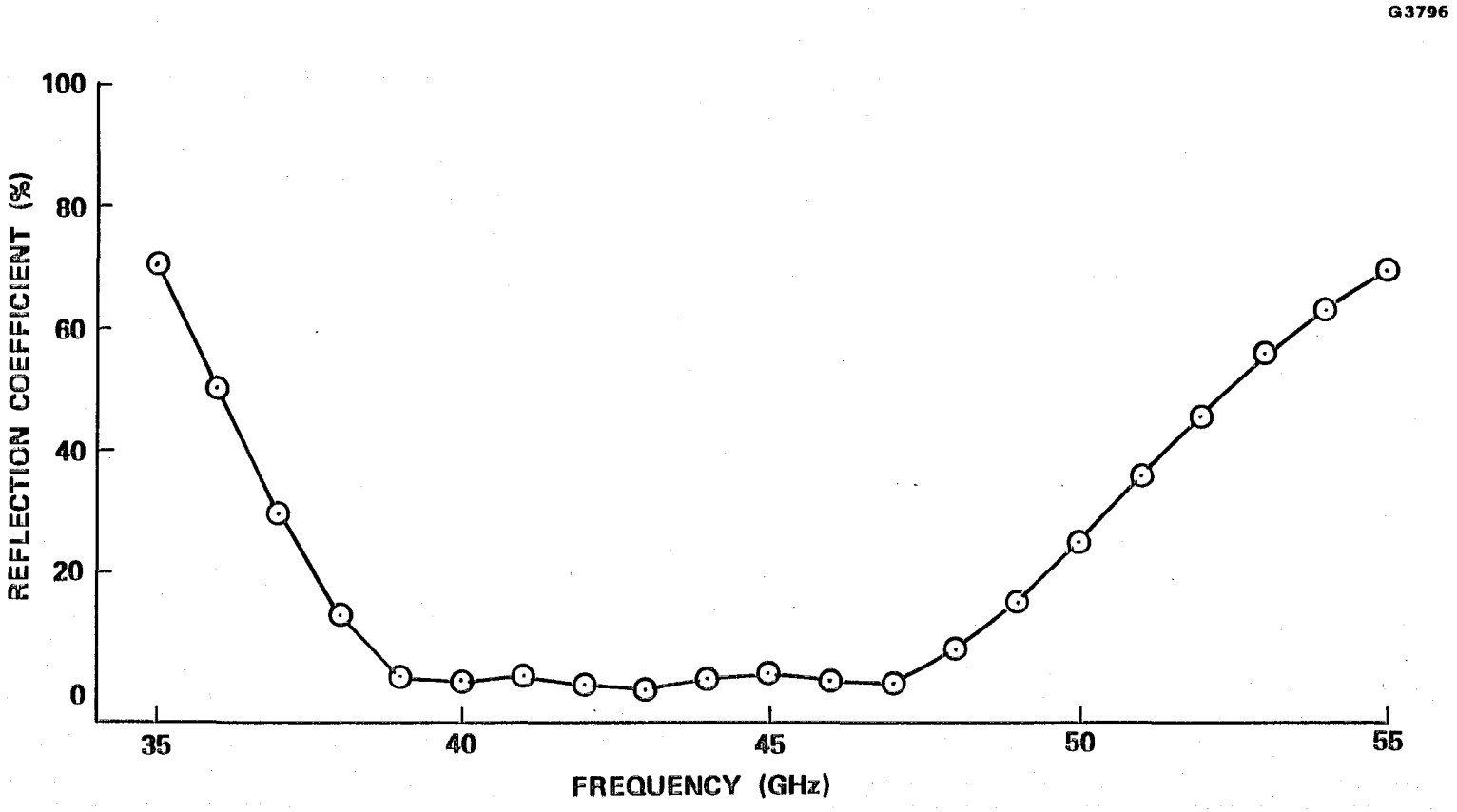

Figure 3-43 Reflection coefficient vs frequency (calculated) for 944H RF window.

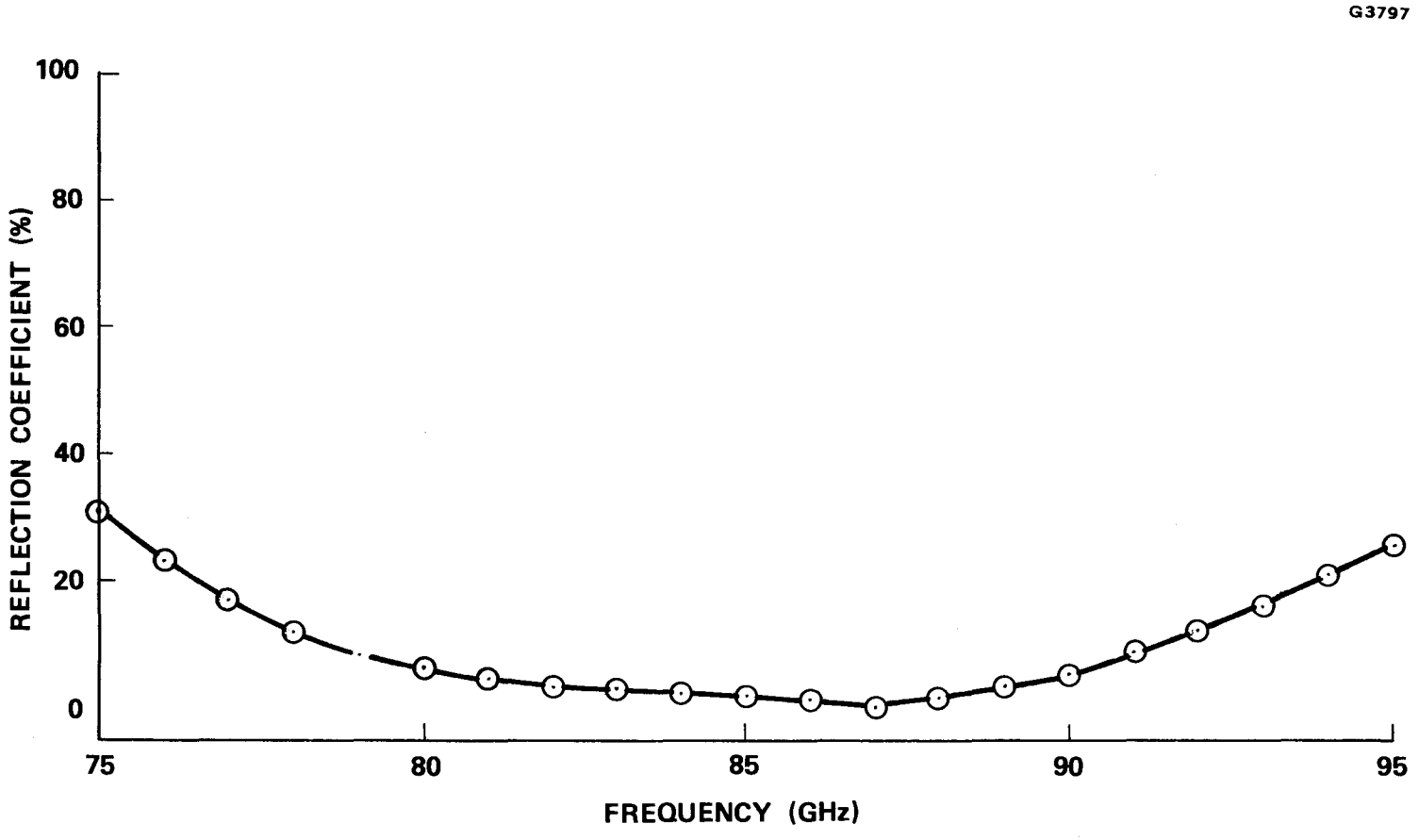

Figure 3-44 Reflection coefficient vs frequency (calculated) for 985H RF window.

TABLE 3-14

SUMMARY OF BLOCK WINDOW DIMENSIONS (cm)

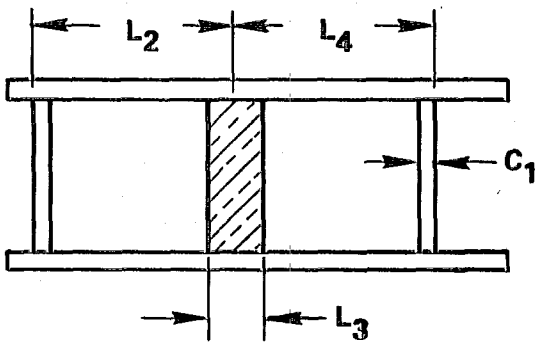

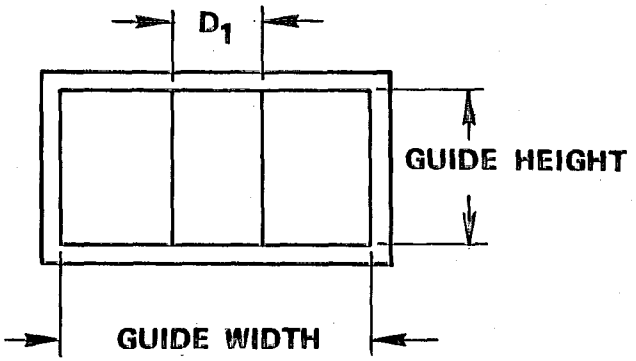

DIMENSION DESCRIPTION	TWT 942H 943H	TWT 944H	TWT 985H
GUIDE (CERAMIC) WIDTH	.478	.569	.254
GUIDE (CERAMIC) HEIGHT	.239	.284	.127
IRIS THICKNESS C_1	.0127	.0127	.0127
IRIS WIDTH D_1	.386	.399	.203
CERAMIC THICKNESS L_3	.1280	.1346	.0699
IRIS LOCATION L_2	.330	.338	.0699
IRIS LOCATION L_4	.330	.338	.185
IRIS THICKNESS C_2	.013	.013	.013
IRIS WIDTH D_2	.386	.399	.203

G1114

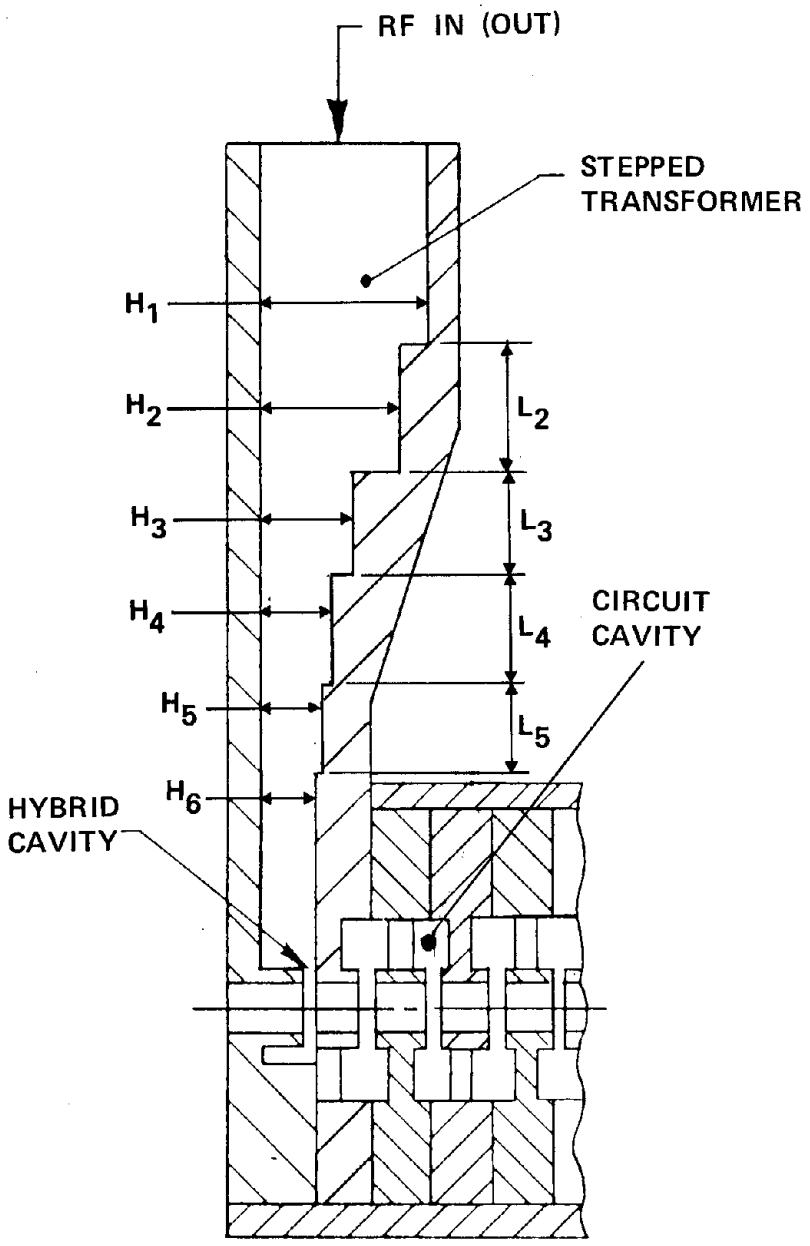

Figure 3-45 Waveguide to circuit transition.

TABLE 3-15

SUMMARY OF STEPPED TRANSFORMER DIMENSIONS (cm)

TWT	H_1	H_2	H_3	H_4	H_5	H_6	L_2	L_3	L_4	L_5
942H & 943H	0.2388	0.2068	0.1425	0.1031	0.0930	-	0.1890	0.1707	0.1778	-
944H	.2845	.2578	.1844	.1144	.0818	.0741	.2016	.1767	.1765	1848
985H	.1270	.1110	.0792	.0594	.0544	-	.1006	.0909	.0945	-

are adjusted to achieve an optimum impedance transition. These are: the post (ferrule) height, distance from post to back wall and coupling aperture angle.

3.8 COLD TEST RESULTS

Two "cold" test sequences were completed during the study program. One of these sequences occurred during the circuit design effort and was conducted on an array of coupled cavities scaled to a low frequency (C- and X-band). This sequence, described in Appendix A, consisted of:

- A determination of the circuits ω vs β characteristic achieved by measuring the multiple resonant frequencies of the coupled cavity array.

- A determination of the interaction impedance by a technique of perturbing the axial electric field of the coupled cavity circuit with a ceramic rod.

Another sequence of tests was conducted to insure a smooth, nearly reflectionless, transition from RF input (or output) port through stepped transition, hybrid cavity, coupled cavity circuit section and into the lossy circuit termination (load). The test vehicle consisted of scaled components (stepped transformers, hybrid cavities, an array of circuit cavities and TWT loads). The required smooth transition was achieved by empirical methods and is described in detail in the present section.

3.8.1 Test Sequence for Achieving Low Reflection Circuit Transition

As cited, the stepped transformer dimensions are determined by computer program. Experimental proof of design is achieved by measuring

the reflection coefficient vs frequency characteristics of two transformers scaled to a convenient low frequency and connected back to back with one extremity RF driven and the other extremity attached to a waveguide (resistive) load.

Typically, reflectance less than 5% was achieved over a frequency band which substantially exceeds the operating bandwidth of the TWT. After satisfactory transformer behavior was demonstrated, two subassemblies were fabricated, each consisting of a stepped transformer and hybrid cavity. These assemblies were fixed to the extremities of a series (typically ten) of circuit cavities. A waveguide load was affixed to one transformer, and an RF source to the other. In this configuration hybrid cavity ferrule (post) length, backwall position and coupling aperture angle was adjusted for minimum reflectance. Figure 3-46 shows the reflection coefficient achieved for the scaled input section of the 942H TWT. The loaded extremity of the assembly was then modified by replacing hybrid cavity, transformer and waveguide load with a scaled TWT termination. In this configuration some further minor adjustment of ferrule lengths, backwall positions and coupling aperture angles are usually required. Figures 3-47, 3-48, 3-49 and 3-50 are reflection coefficient vs frequency for the 942H, 943H, 944H and 985H. Each test assembly consisted of: stepped transformer hybrid cavity, coupled cavity array, and TWT termination.

A similar experimental method was followed in developing an output circuit transition of minimal reflectance. However, the presence of the two step velocity taper in the output provides an additional complication. Initially the same (as input) method was followed; an assembly consisting of a stepped transformer, hybrid cavity, coupled cavity circuit array (uniform), hybrid cavity, stepped transformer and waveguide load, was experimentally adjusted in the same manner as the input circuit, for minimum reflection-coefficient vs frequency. The assembly was then

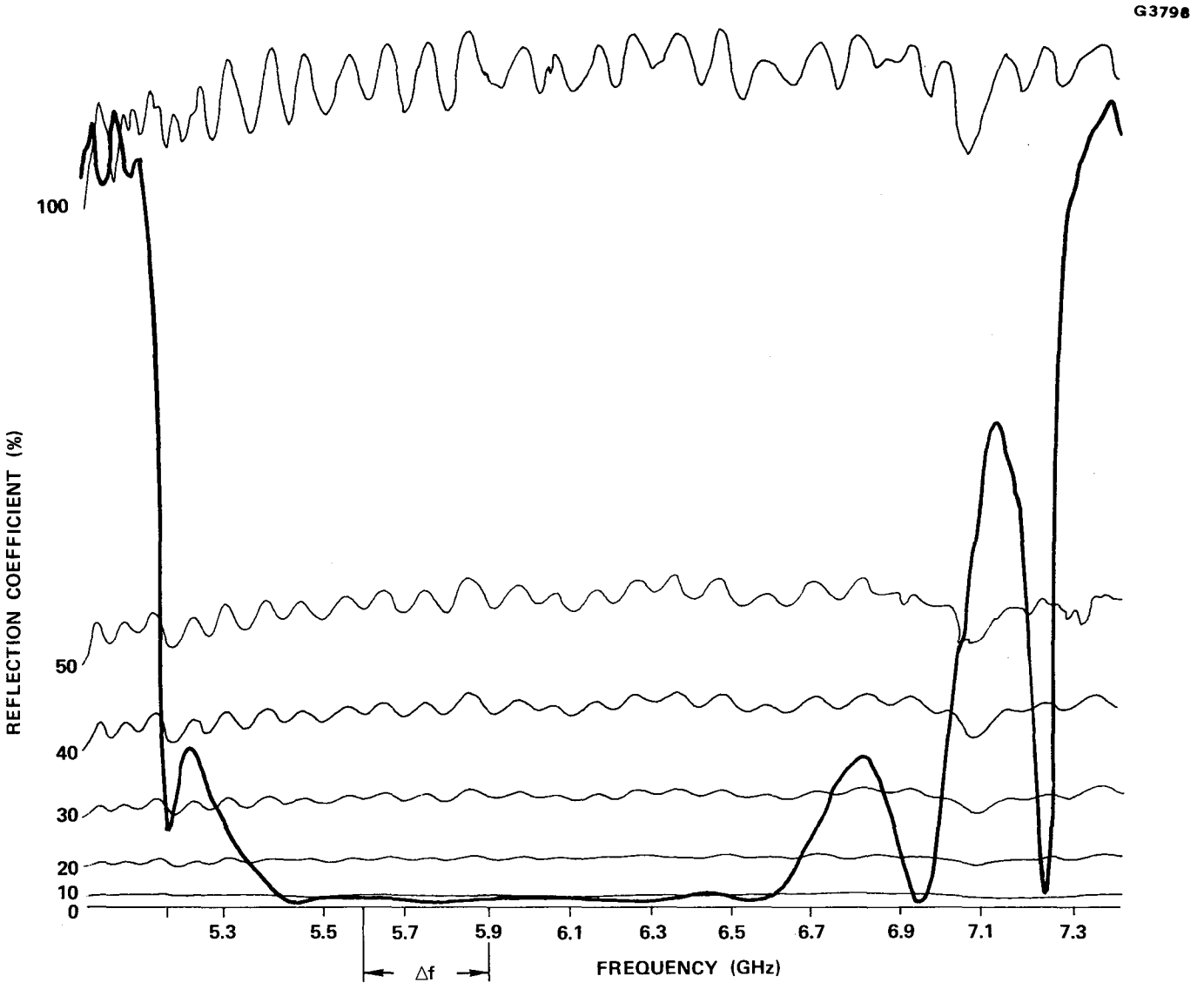

Figure 3-46 Reflectance vs frequency for the (scaled) 942H input test assembly consisting of: stepped transformer, hybrid cavity, coupled cavity array, hybrid cavity, stepped transformer and waveguide load.

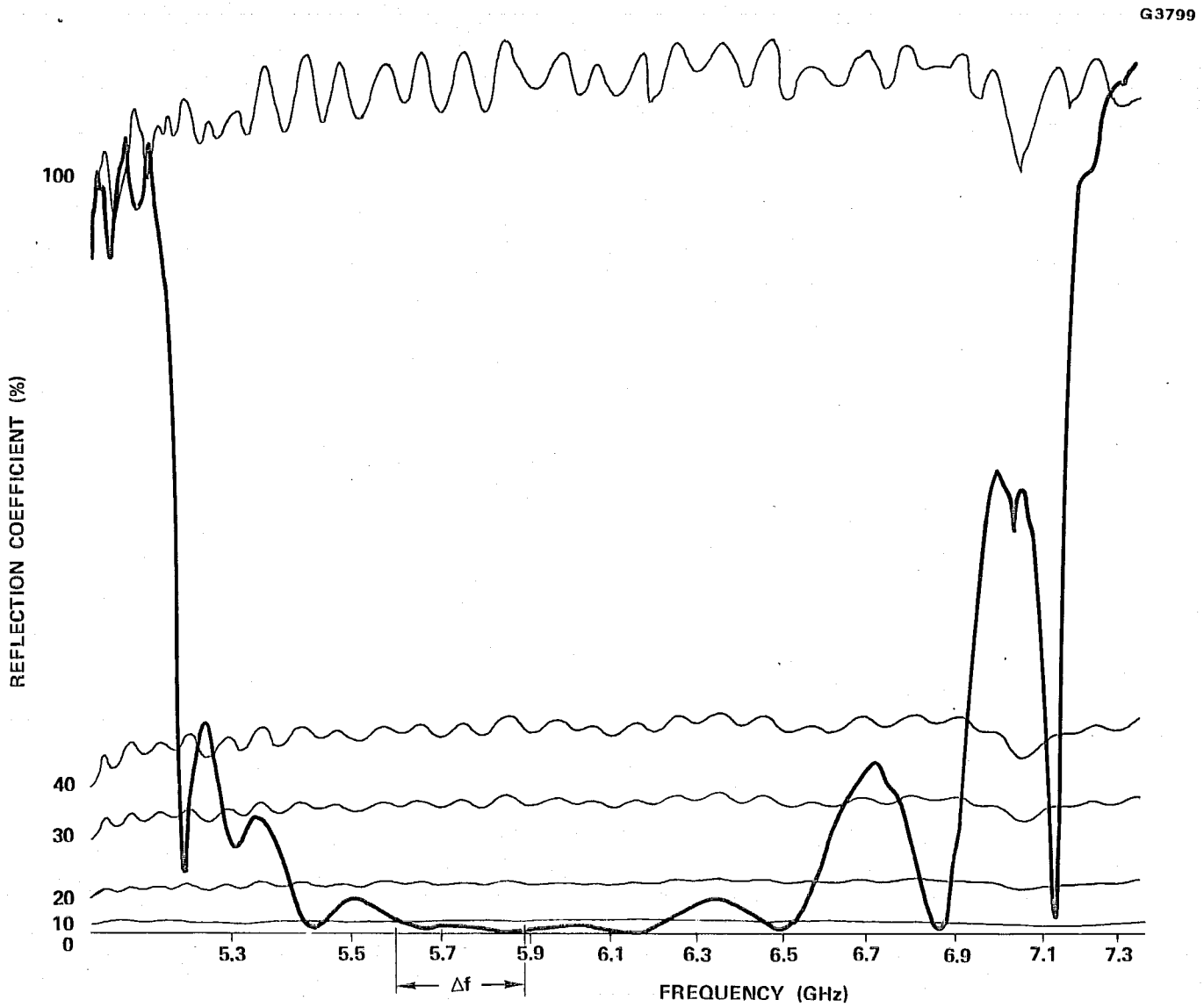

Figure 3-47 Reflectance vs frequency for the (scaled) 942H input test assembly consisting of: stepped transformer, hybrid cavity, coupled cavity array, hybrid cavity, stepped transformer and waveguide load.

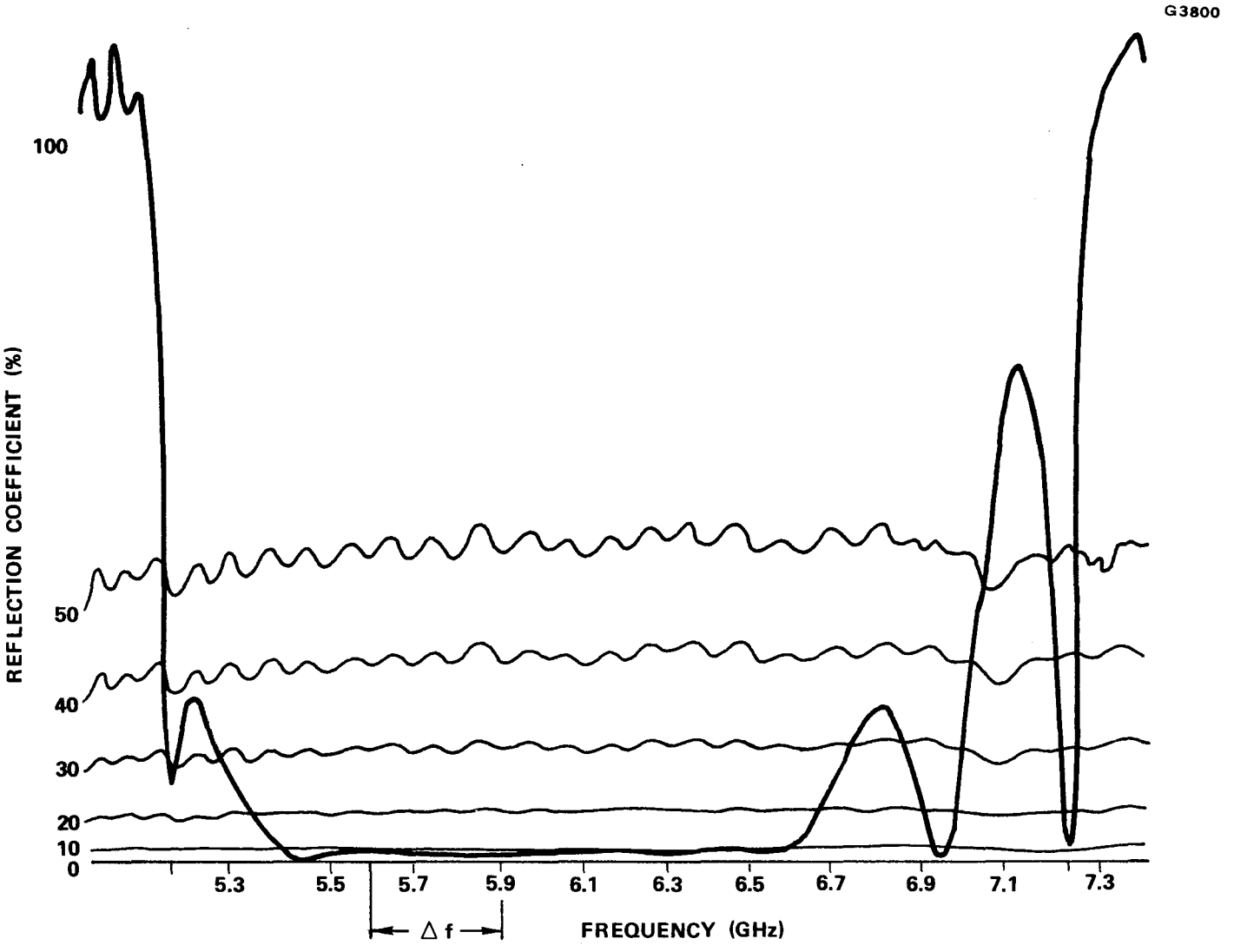

Figure 3-48 Reflectance vs frequency for the (scaled) 943H input test assembly consisting of: stepped transformer, hybrid cavity, coupled cavity array, hybrid cavity, and TWT load.

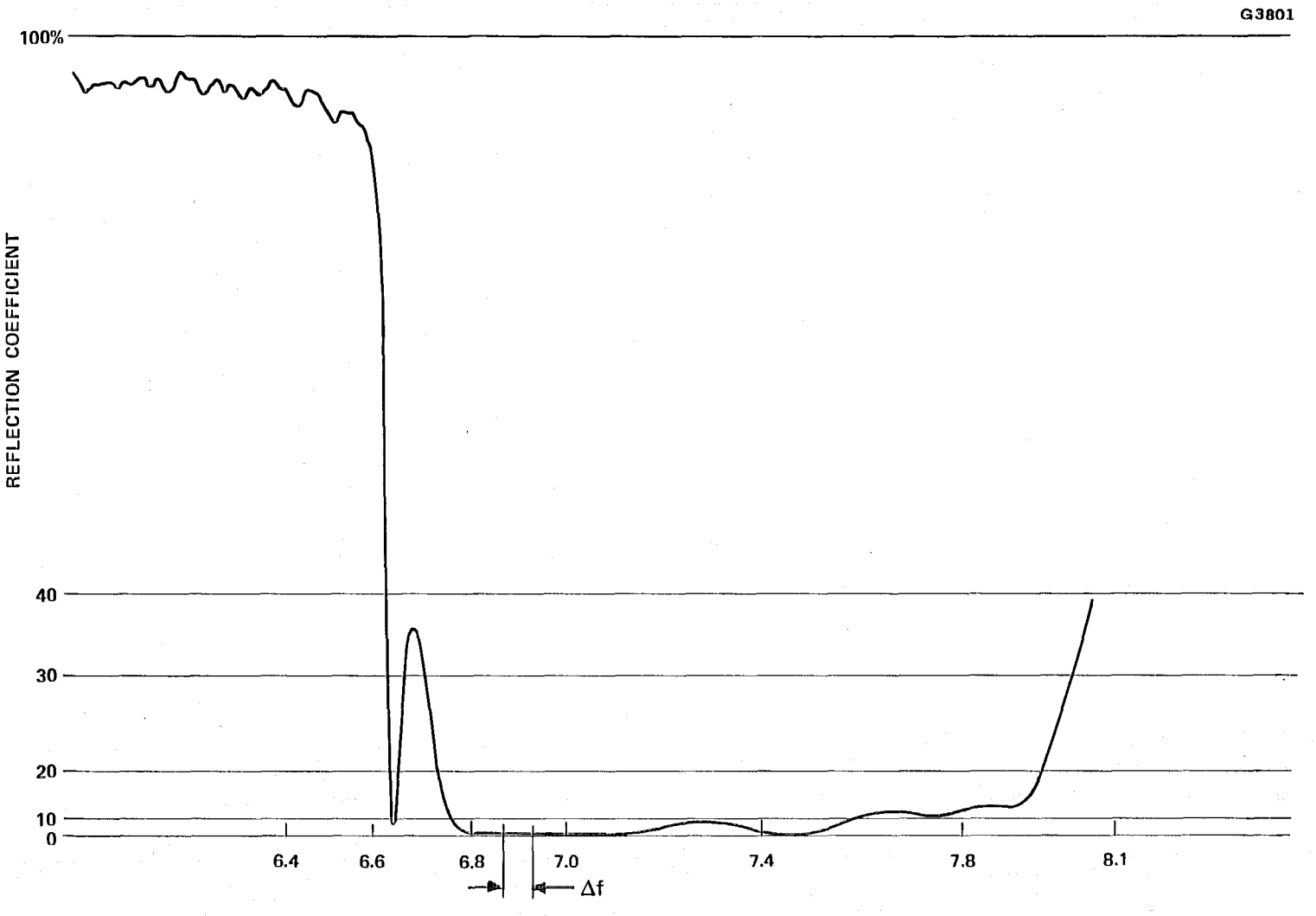

Figure 3-49 Reflectance vs frequency for the (scaled) 944H input test assembly consisting of: stepped transformer, hybrid cavity, coupled cavity array, hybrid cavity and TWT load.

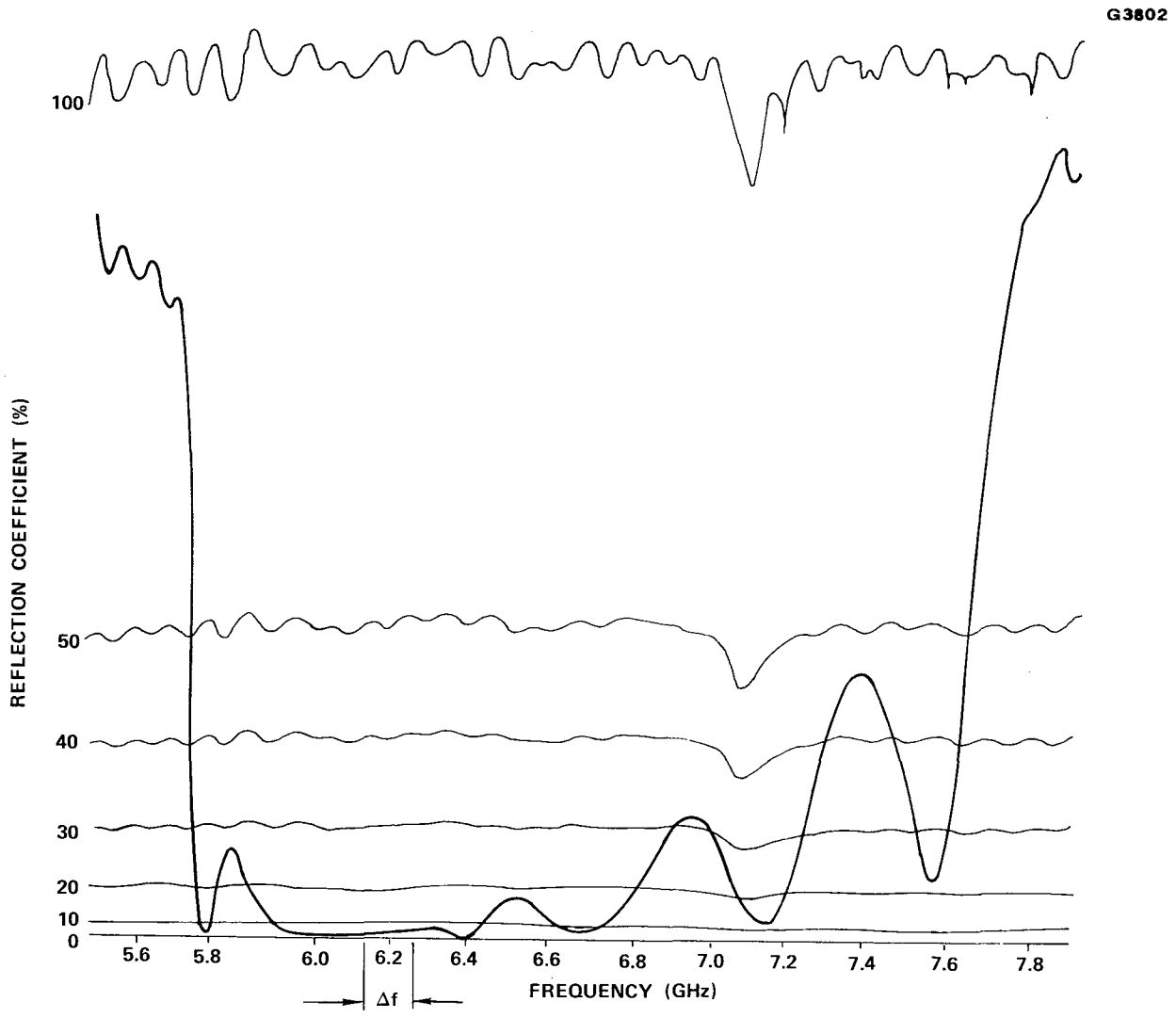

Figure 3-50 Reflectance vs frequency for the (scaled) 985H input test assembly consisting of: stepped transformer, hybrid cavity, coupled cavity array, hybrid cavity and TWT load.

modified to consist of: stepped transformer, hybrid cavity, coupled cavity circuit array (uniform), and TWT termination; the assembly was fine tuned to yield minimum reflectance. Finally, the test assembly was again modified to include the two step velocity taper cavities. The assembly then consisted of: stepped transformer, hybrid cavity, uniform coupled cavity circuit array, two step velocity taper (cavities), and TWT termination. Again, the assembly was adjusted to yield minimum reflectance. This adjustment consists of minor modification of coupling aperture angle and ferrule length in the transition regions between uniform cavity array and first velocity step, between first velocity step and second velocity step and between second velocity step and termination. Figures 3-51 and 3-52 show reflectance vs. frequency for the 943H and 985H output circuit sections respectively. Each assembly consisted of: stepped transformer, hybrid cavity, uniform coupled cavity array, two step velocity taper and TWT termination.

Circuit design is not complete until full scale components (i.e., components dimensioned to operate at the specified millimeter wavelength) are fabricated, assembled and tested. Although adjustment of the circuit during this stage is limited, one powerful (although tedious) technique remains. This consists of methodically shifting the axial position of the cavity components of the uniform portion of the circuit section until the most advantageous reflectance (minimum in the operating frequency pass band) pattern is achieved.

No full scale parts were fabricated during the study program described in this report.

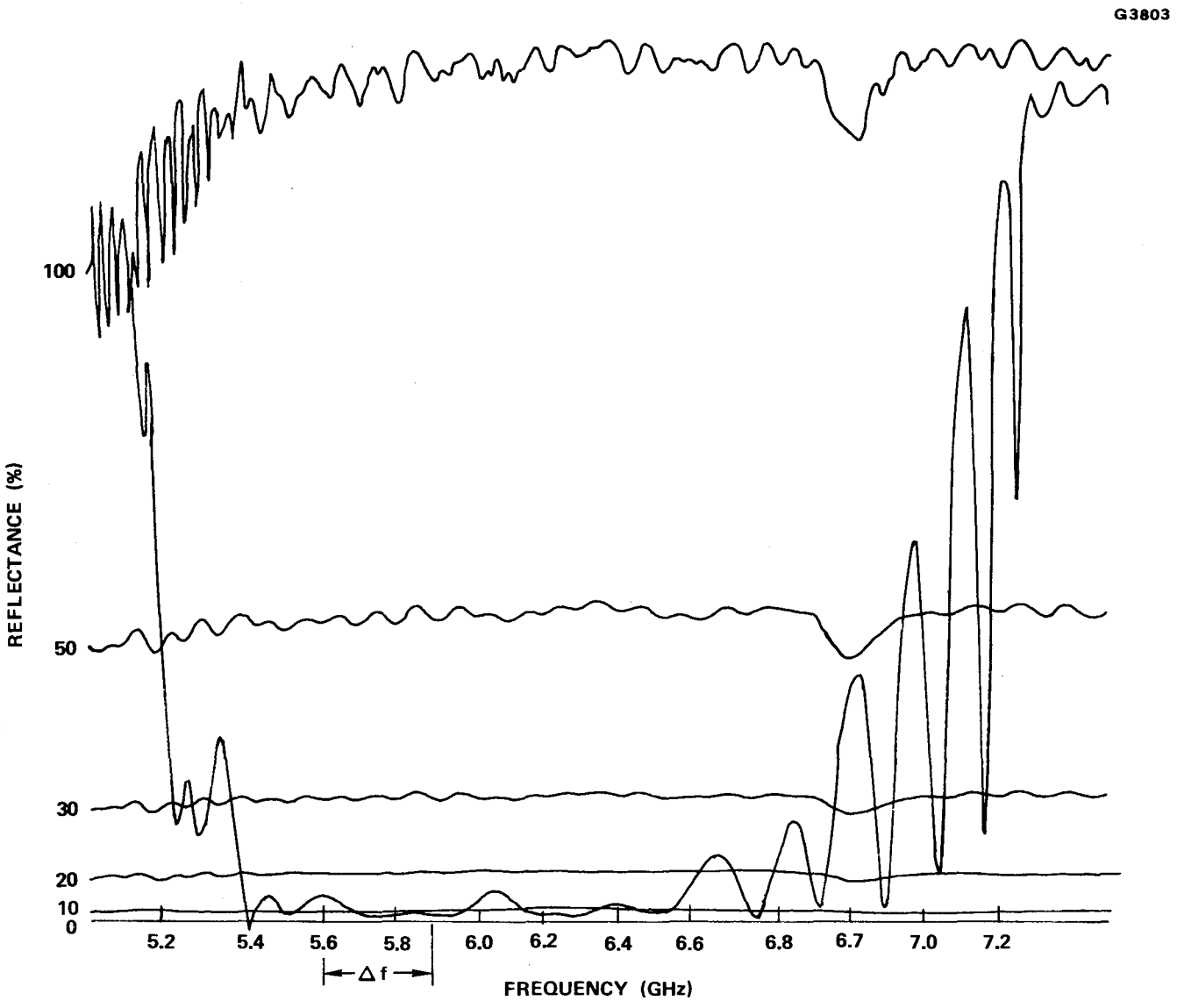

Figure 3-51 Reflectance vs frequency for the (scaled) 943H output test assembly consisting of: stepped transformer, hybrid cavity, coupled cavity array, hybrid cavity and TWT load.

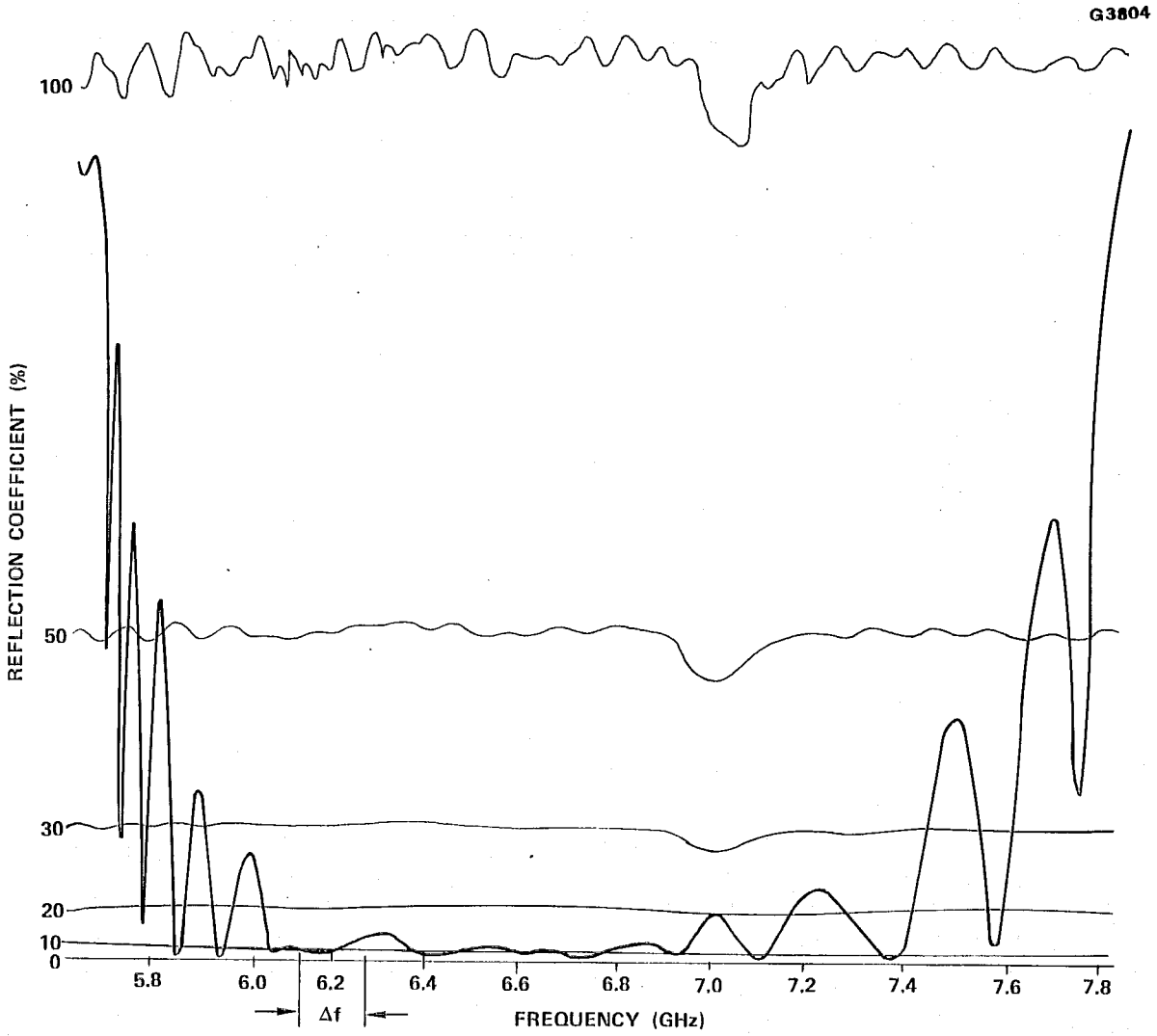

Figure 3-52 Reflectance vs frequency for the (scaled) 985H output test assembly consisting of: stepped transformer, hybrid cavity, coupled cavity array, hybrid cavity and TWT load.

Page Intentionally Left Blank

4.0 MECHANICAL DESIGN

The four TWTs of this study program are similar in many ways to millimeter wavelength TWTs recently developed and produced at Hughes. Areas of similarity are:

- Electron gun and ion pump as an integral structure
- Rugged metal ceramic "block" RF input and output windows
- A sintered coupled cavity circuit which includes internal terminations and a two step velocity taper
- A spent beam refocusing section
- A multi-stage depressed collector
- A precision aligned PPM focusing array

The electron gun and coupled cavity circuit are conduction cooled to the TWT mounting plate. The three stage depressed collector is radiation cooled.

4.1 VACUUM ENVELOPE

Figure 4-1 is the vacuum envelope of the 944H TWT and is similar to the other three TWTs of this study program. The vacuum envelope consists of four major subassemblies. These are: the electron gun and ion pump assembly; the window and transformer assembly; the coupled cavity circuit assembly; the collector plate assembly and the multi-stage collector assembly. Also illustrated in Figure 4-1 is the precision PPM focusing structure.

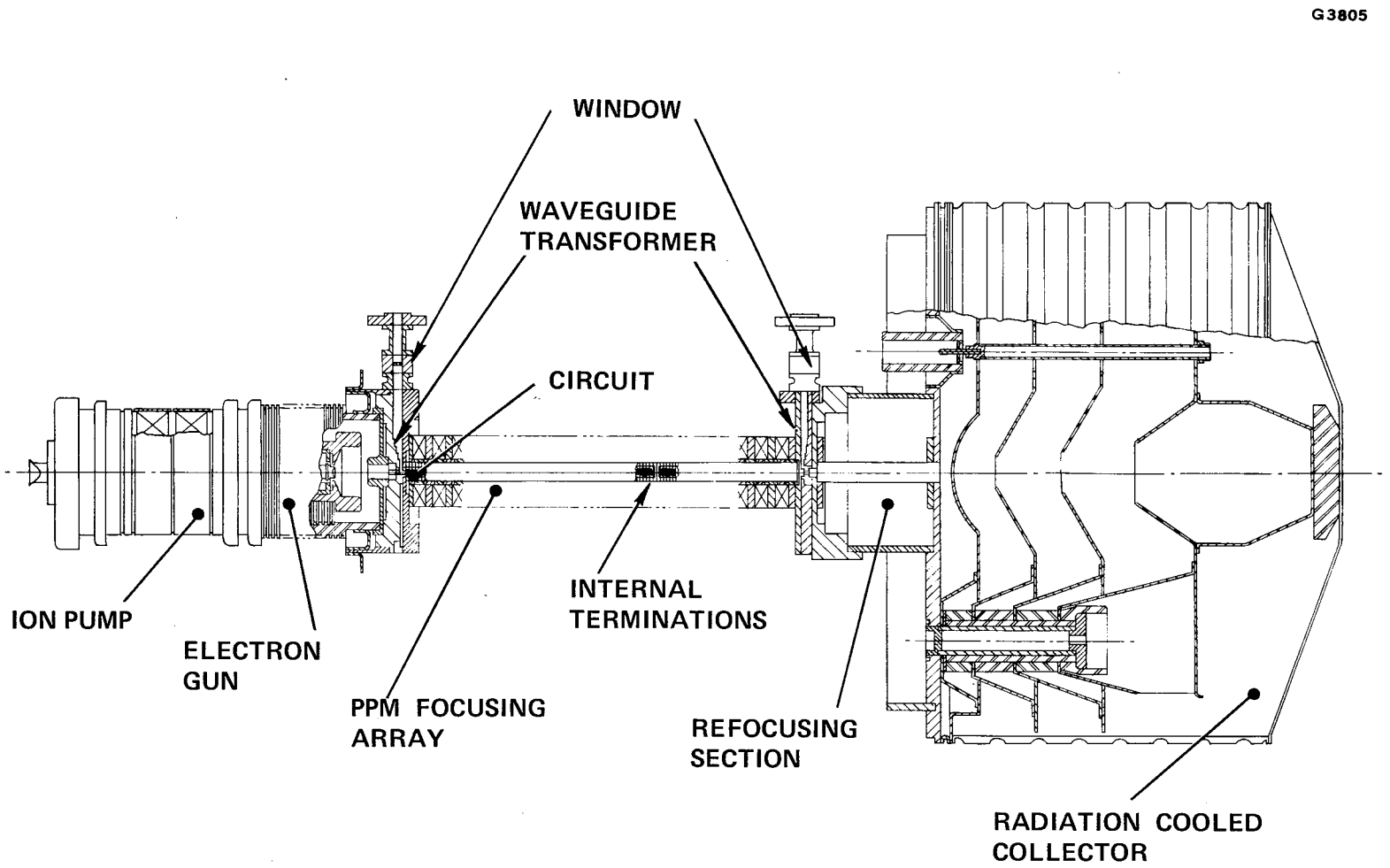

Figure 4-1 944H TWT vacuum envelope (PPM focusing array included).

4.1.1 Electron Gun and Ion Pump Assembly

The principal support member of the electron gun is a heavy cylindrical ceramic insulator metallized on each (flat) end surface by the molybdenum-manganese process and butt brazed to stainless steel flanges. This ceramic insulator provides, from end to end, cathode voltage standoff (e.g., 25 kV for the 985H). The cathode-focus electrode subassembly is supported at one extremity of the ceramic cylinder and the anode is supported at the other. A cylindrical ion pump of metal-ceramic construction is heliarc welded to the flange at the cathode-focus electrode extremity of the electron gun ceramic support cylinder. The ion pump is always energized during TWT operation. It is needed because of the high power density and low volume inherent in millimeter wavelength TWTs. The exhaust tubulation (shown in Figure 4-1 after "pinch-off") protrudes from the unattached end of the ion pump opposite the electron gun. The anode is captured at the extremity of the electron gun ceramic support insulator opposite to the cathode-focus electrode assembly. The flange at the anode end of the ceramic support cylinder is heliarc welded to a mating flange on the stepped transformer support cylinder.

4.1.2 Body and Window Assembly

A vacuum sheath of stainless steel encloses the TWT coupled cavity circuit over its entire length and is brazed to the transformer subassemblies at either end. The window subassemblies are then brazed to each transformer. The RF circuit parts, including the transformers, are fabricated of oxygen free high conductivity copper (OFHC), machined to final dimensions by electric discharge machining (EDM) techniques. Components which form the vacuum wall are either brazed or heliarc welded. The coupled cavity circuit components (not a part of the

vacuum wall) are sintered together. A typical millimeter wavelength TWT termination developed at Hughes is shown in Figure 4-2. Similar terminations are planned for the TWTs of this report. The termination consists of a "doughnut" shaped lossy ceramic member brazed in a special termination cavity. For a three section TWT, four terminations are required. During the study program scaled terminations were fabricated and tested as a component of the scaled RF circuit test assemblies.

4.1.3 Drift Tube and Collector Plate Assembly

This assembly is fabricated of stainless steel. The drift tube portion, when accompanied by permanent magnets, forms the spent beam refocusing section and resides between the coupled cavity circuit and collector. The drift tube, together with its outer support cylinder, is brazed to the collector plate comprising one of the principal structural elements of the finished TWT. This assembly is brazed to the body and window assembly (Figure 4-1).

4.1.4 Multi-Stage Collector Assembly

Figures 4-6 and 4-7 show two three-stage collector designs. Figure 4-6 is suitable for the 942H, 943H, 944H and 985H. Figure 4-7 is an alternate design for the 985H. Both collectors consists of a series of stacked, molybdenum, dish-shaped electrodes. Each electrode of Figure 4-6 includes three hollow conical legs. The legs are mated with ceramic sheathed, molybdenum posts. The legs of successive electrodes are separated by ceramic washers. The final collectors stage is attached to the outer (stainless steel) shroud by an insulating beryllia ceramic disk. The joints between the collector, ceramic disk and shroud are brazed. High voltage connection is accomplished by means of feed-through insulators.

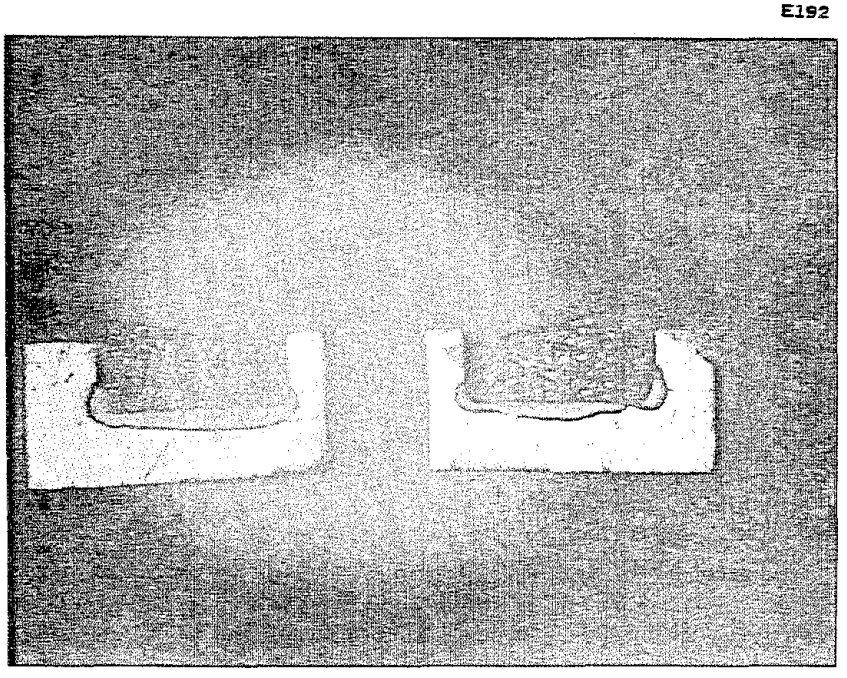

Figure 4-2 Section view of a brazed millimeter wavelength TWT termination.

This multi-stage collector subassembly is heliarc welded to the collector plate along its periphery, at the support tubes, and at the electrical feed-through insulator structures. Special provisions were included to accommodate the differential thermal expansions encountered in the collector electrode support members. Shims and "bellville" washers (not shown) accommodate the length differentials of insulators stacked on molybdenum support tubes. Similarly, elongated holes in the collector electrode support cones at the capture regions of the support posts permit radial differential expansion of the collector electrodes to occur relative to the support plate.

4.1.5 Periodic Permanent Magnet Focusing Structure

A unique PPM focusing structure was devised at Hughes, has been used extensively on millimeter wavelength tubes, and is suitable for the TWTs of this study program. Figure 4-3 illustrates the PPM structure. Soft iron (magnetic) ferrules and stainless steel (nonmagnetic) spacers are fabricated as continuous ring elements, with their outer diameter substantially oversized. These components are assembled on a mandrel, brazed together, then removed from the mandrel. The ferrule-spacer assembly is split axially into two sections by means of a slotting saw. The edges of the split are lapped smooth. The two halves of the ferrule-spacer assembly are mated and precisely aligned by means of dowel pins. The cross-section of the assembled unit is elliptical but is now machined (round) on the outside surface and precision honed on the inside surface. The following advantages accrue from this kind of focusing array:

- Pole pieces are not attached to TWT until after assembly and vacuum processing is completed.

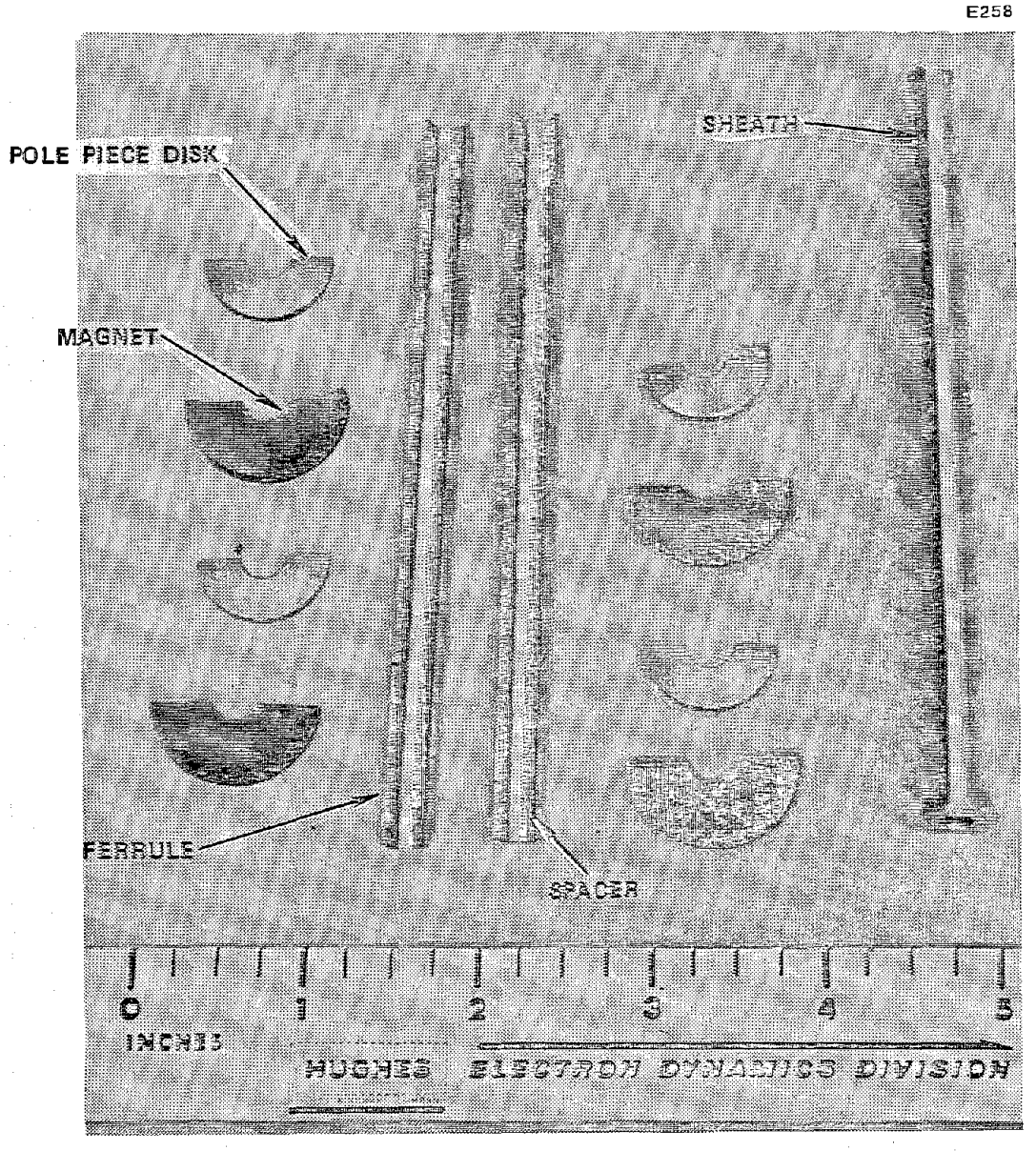

Figure 4-3 Components of the periodic permanent magnet focusing array.

- Superior alignment and focusing is achieved, a result of the precisely fabricated ferrule assembly.

The pole piece disks and magnets are assembled on the ferrule-spacer assembly and secured by means of tie wires to complete the PPM array.

4.2 PACKAGE

The package design for the 942H, 943H, 944H and 985H TWTs is similar to a package configuration developed at Hughes and used successfully on several millimeter wavelength TWTs. The package is in two separate parts, the inner package assembly and the final package assembly.

4.2.1 Inner Package

Figure 4-4 shows the inner package of the 985H TWT. The purpose of the inner package is to provide high voltage standoff and enhanced structural integrity of the vacuum envelope. The high voltage area of the gun and ion pump is surrounded by an evacuated metal envelope which is backfilled with a degassed dielectric (freon) fluid. In addition, the ion pump is supported within the envelope at the tubulation end by the epoxy-glass ion pump support member (Figure 4-4).

The coupled cavity circuit and PPM focusing array of the TWT is strengthened by means of the inner support assembly which is a split cylindrical shell extending from the input transformer block to the output drift tube support cylinder. The inner support assembly is rigidly attached at each end and strengthens the potted magnet stack. It is the principal mechanical support of the inner package structure. It isolates the TWT circuit from bending stresses and includes a built in expansion capability which can accommodate the longitudinal differential expansions encountered in a changing thermal environment. Thus, the inner package

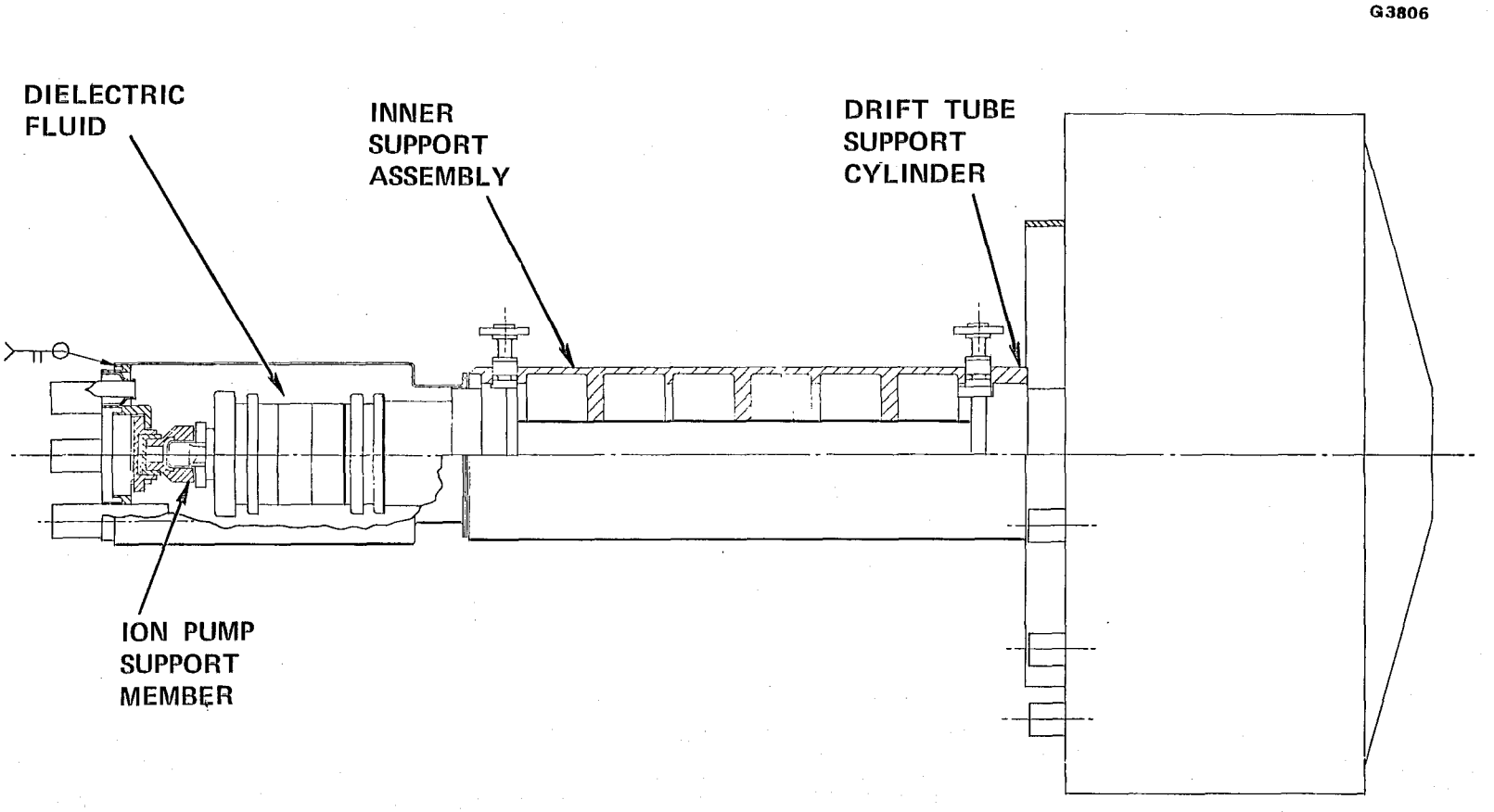

Figure 4-4 985H inner package.

comprises an insulated, structurally rigid assembly with all surfaces at electrical ground potential.

4.2.2 Final Package Assembly

Figure 4-5 shows the 985H TWT in its final package configuration. The principal component of the final package assembly is the base plate (see Figure 4-5).

The inner package is mounted on the baseplate by means of bearing block assemblies (Figure 4-5) with the collector and plate cantilevered from one end. Thus, the mounting baseplate does not extend beyond the collector plate. The bearing blocks are clamps which capture several circular copper bearings coated with dry lubricant. The degree of clamping is controlled by shims. The bearings accommodate the differential expansion of the inner package assembly relative to the baseplate. The collector support plate is cantilevered from the adjacent bearing block assembly. The bearing block is secured to the baseplate with bolts while the brackets attached to the collector plate are secured with spot heliarc welds.

The final package assembly is summarized. The baseplate is the rigid mounting member which includes an appropriate hole pattern for system mounting. Two bearing block assemblies are bolted directly to the baseplate, one at the gun end and the other at the drift region adjacent the collector. The collector support plate is secured to the latter (bearing block assembly) by heliarc welds and to the baseplate by brackets secured by bolts. Thus, at the collector plate drift tube region, the vacuum envelope is rigidly attached to the baseplate. At the electron gun end of the TWT however, the bearing block prevents motion of vacuum assembly transverse to the baseplate but accommodates relative longitudinal motion, thus allowing differential expansions as encountered during operation.

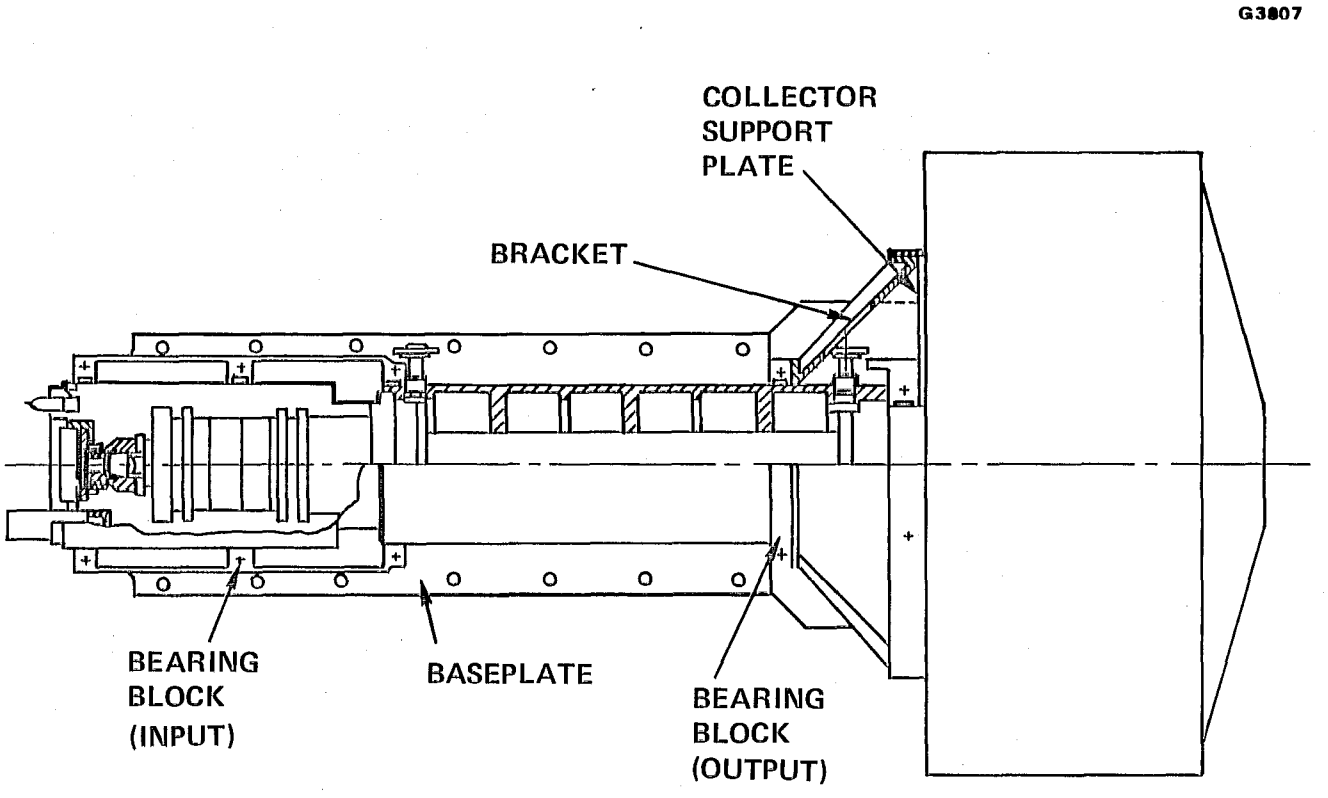

Figure 4-5 985H final package assembly.

4.3 MECHANICAL ANALYSIS

As cited, Hughes has developed several TWTs of a design similar to that of the 942H, 943H, 944H and 985H. Analysis and, more importantly, extensive test under environmental conditions compatible with the TWTs of this program have been accomplished successfully in the past. The conduction cooled collectors of Hughes previous millimeter wavelength TWTs, however, differ substantially from the radiation cooled, multi-stage collectors of the 942H, 943H, 944H and 985H. Therefore, as a part of this study program Hughes undertook a mechanical analysis of the radiation cooled collectors.

Figure 4-6 shows the post supported multi-stage depressed collector design. A collector design of this type was formulated for each of the four TWTs of this study program. Because of the high collector temperature encountered with the 985H TWT, a consequence of its relatively low efficiency, an alternate collector was designed. This collector, which employs a cage support structure, is shown in Figure 4-7. Its advantage is an improved internal view factor compared to the post supported structure.

Two kinds of stresses were considered: dynamic vibration stresses and thermal stresses.

4.3.1 Dynamic Vibration Stresses

Several important structural areas were considered.

- Collector electrodes

The natural resonant frequency was calculated for typical disk electrodes for each of the two collector designs. These frequencies were

G3832

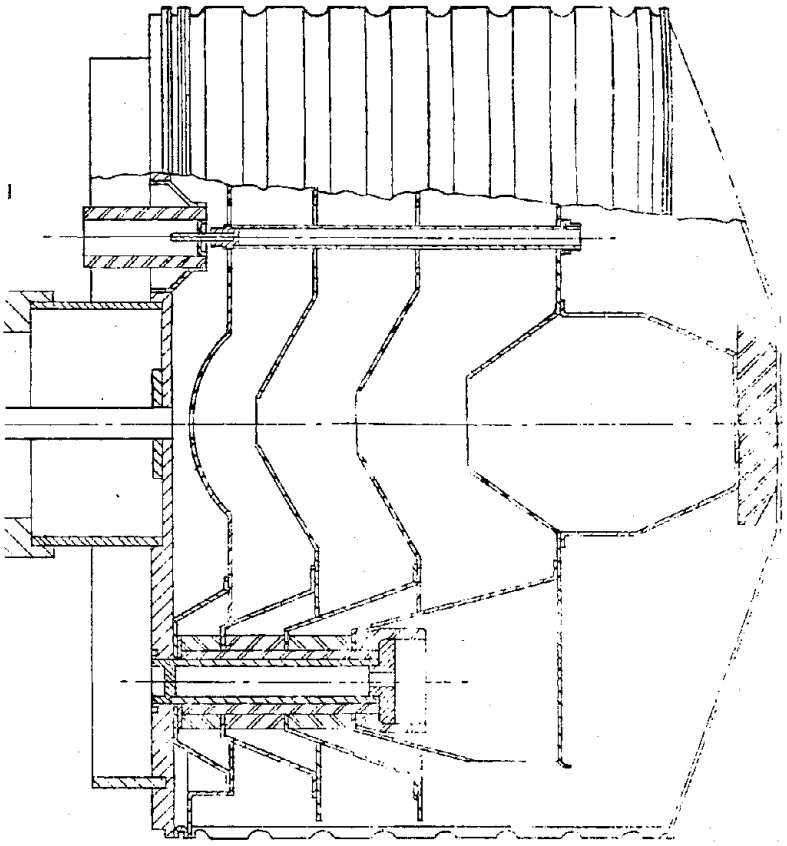

Figure 4-6 Post supported multi-stage depressed collector.

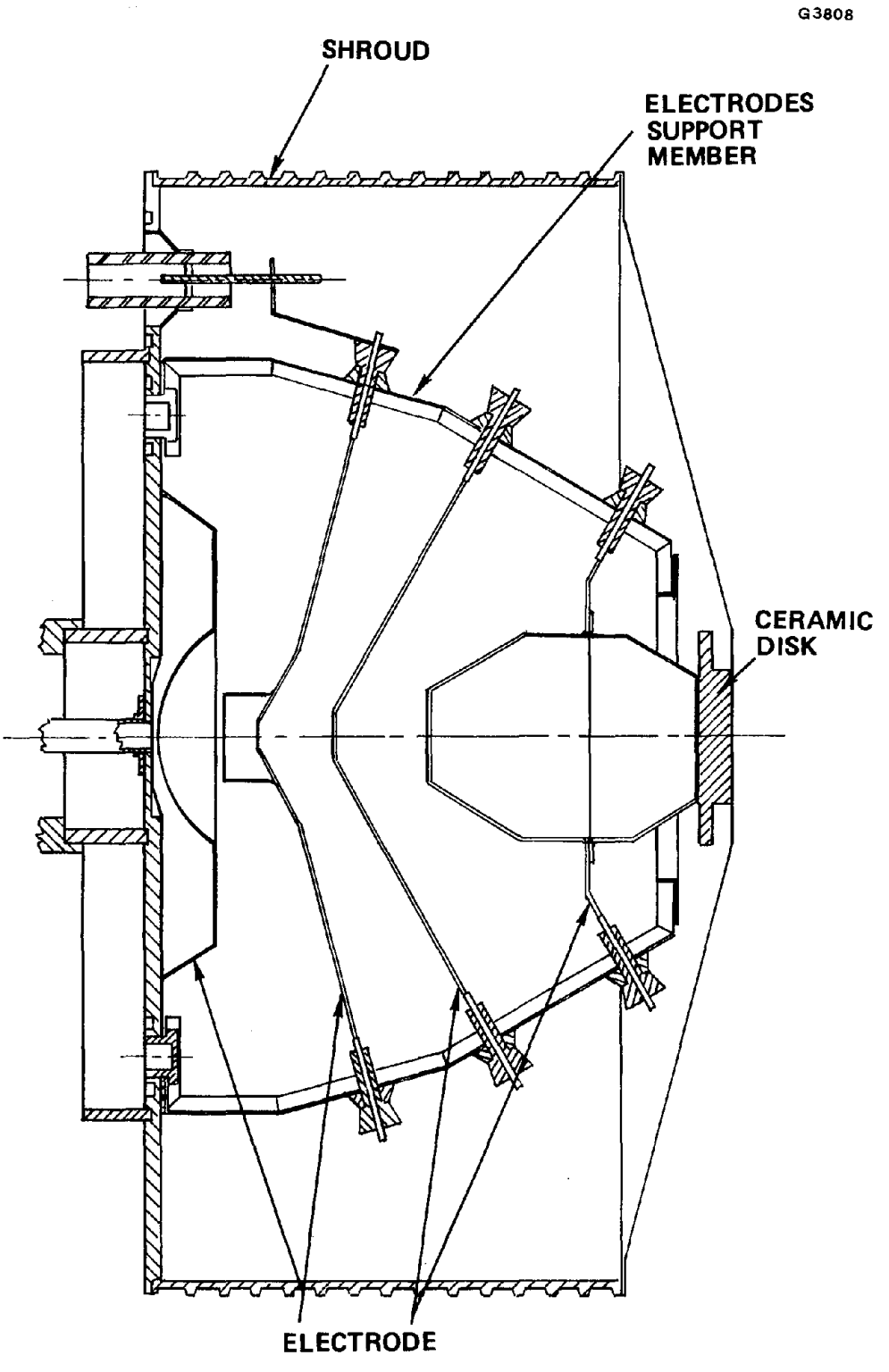

Figure 4-7 985H cage supported multi-stage depressed collector.

approximately 200 Hz for the post supported design (Figure 4-6), and 100 Hz for the cage design (Figure 4-7). The bending stresses induced under these conditions were calculated and determined to be near, but below, the material yield point. The nature of the assumptions is known to produce a pessimistic result; thus the integrity of the design is considered adequate. Safety factors are easily enhanced, however, by minor modification of part dimensions.

- Collector shroud

The resonant frequency of the collector shroud for either the post design or the cage design was computed and found to be 3059 Hz. Since this is considerably higher than the specified environmental vibration frequency band, no input vibration energy is expected to couple.

- Restraining screws

The dynamic stresses encountered through vibration will load the restraining screws which secure the collector and the adjacent bearing block assembly to each other and to the TWT baseplate. These restraining screws have a safety factor of 21.7 below the material yield point; however, because of the materials elasticity, a small reversible extension will occur under peak vibration loading.

- Electrode Support Structure

This evaluation was made for the cage design only, since the post design has been sucessfully employed on a Hughes space TWT. A natural resonant frequency of approximately 250 Hz for the cage design was calculated. The accompanying bending stresses show a safety factor of 3 below the yield point of the material.

- Composite collector structure

The foregoing discussion treats various collector components and subassemblies separately. The entire composite structure presents a considerable more complicated analysis task. Precise computations for the composite structure were not attempted. It is unlikely that individual resonances will be sufficiently correlated in frequency to cause amplitude enhancement and it is concluded that the structures strength is more than adequate to carry the resulting loads.

There is, however, a concern for the collector's mechanical relationship to the remainder of the TWT vacuum envelope structure. In the event that the composite collector structure is resonant in the environmental vibration band, it could transmit adverse bending stresses to the body (coupled cavity circuit) of the TWT and result in a vacuum leak or impaired electron beam focusing. To overcome this kind of difficulty, the collector assembly could readily be decoupled mechanically from the coupled cavity circuit and drift tube structure by means of a metal bellows welded in the collector support plate. This kind of modification would leave the structure otherwise unchanged.

4.3.2 Thermal Stresses

This subject is divided into several important structural areas.

- Collector electrodes

Different kinds of thermal stresses occur in the operation and processing of the TWT. Stress which accompanies a large, though uniform change in temperature is encountered during processing "bakeout" of the TWT. The molybdenum electrodes expand somewhat less than the stainless steel collector plate. This applies side loads on the support posts and

induces a bending stress in them. This is counteracted by elongating the electrode holes which surround two of the posts to permit relative motion between post and electrode. For an extreme condition (e.g., 650°C bakeout), radial thermal stress during normal TWT operation will occur. The highest temperature region of this radial thermal gradient is towards the center of the collector electrode. This hot center portion tends to expand, but is constrained by the cooler outside portion. Under extreme conditions these differential forces induce a maximum stress of approximately 22000 pounds per square inch (psi), a value well below the yield point of molybdenum.

- Support posts

A longitudinal differential expansion between the metal electrode support posts and the ceramic spacer insulators accompany a temperature change. An extreme dimensional difference of .014 inch is anticipated. Several bellville washers (not shown in Figure 4-6) stacked on each post will readily compensate for this axial expansion differential. The bellville washer (used extensively at Hughes) is a spring washer formed in a slightly conical shape. These washers are stacked apex to apex and base to base thus forming a stiff axial spring. The number of washers in the stack determines its maximum compensation capability.

- Ceramic disk

The beryllia ceramic disk which attaches the final collector stage electrode to the shroud undergoes both compressive and tensile stresses. A maximum stress value of only 21 psi was calculated.

- Composite collector structure

The thermal stress conditions encountered in collector assemblies are due to differential expansion of dissimilar materials, to temperature gradients encountered in a single part, or to a combination of the two. Stresses due to gradients are well below yield values. This is also true of differential expansion stresses. Side loads on the posts are an exception and this difficulty is avoided by elongating electrode holes.

Another important consideration is the avoidance of stress concentrations. For this reason, all abrupt mechanical discontinuities are avoided and parts are dimensioned to preclude assymmetrical loading.

5.0 THERMAL ANALYSIS

A thermal analysis of the collector designs for the 942H, 943H, 944H and 985H was conducted. Figure 4-6 depicts a collector configuration which was analyzed for all four TWT types. Figure 4-7 is an alternate collector design for the 985H. These analyses were for six different modes of operation and included the effects of:

- RF drive
- Solar radiation
- Space view factors of 1.0, 0.5
- Radiating surface condition

For each combination of conditions, the temperature distribution throughout the collector was computed together with its related thermal power flow pattern. The results of this study are summarized in this section of the report.

Areas of special interest are the maximum temperature reached in the TWT collector and the amount of power conducted to the spacecraft mounting surface. The power level of the TWT and the mode of operation was the strongest effect on these parameters. The difference in the designs of the post supported collector of Figure 4-6 and cage supported collector of Figure 4-7 causes a minor effect on these parameters.

Each collector has four electrodes. These electrodes are identified, in this report, as number one, through number four, the electrode nearest the coupled cavity circuit is number one. Figure 5-1 shows the 944H TWT operated in the RF on, sun on mode. Note that the collector achieves a maximum temperature of 307°C at the aperture of electrode number three. Electrodes one and two are at temperatures of 247°C and 270°C respectively. Electrode four temperature is substantially less. This occurs

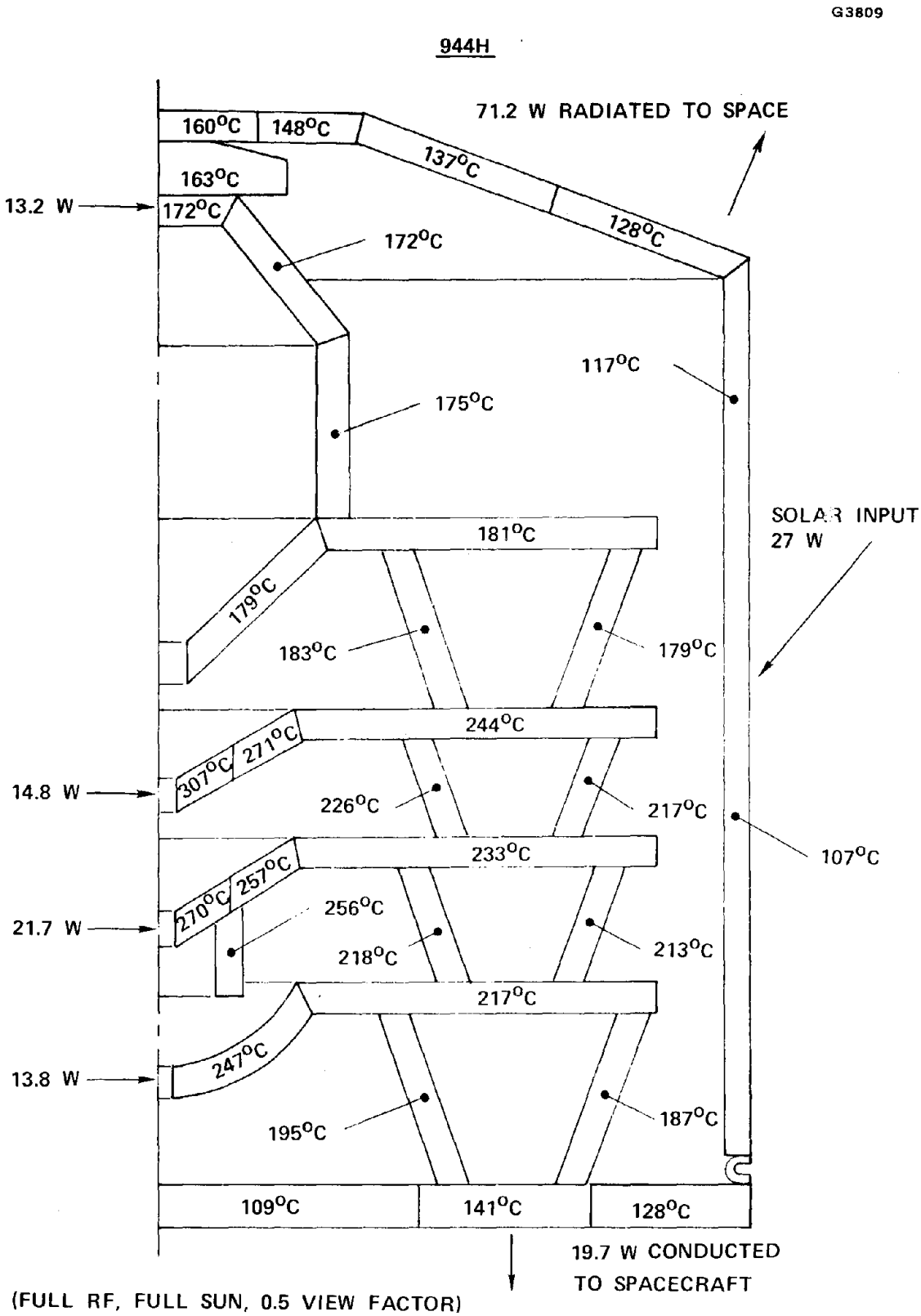

Figure 5-1 944H thermal anlysis of post supported collector configuration, space view factor 0.5, RF on, sun on.

because electrode number four is cooled via a low impedance conduction path through the brazed beryllia ceramic insulator to the shroud, while the cooling path of electrodes one, two, and three is of substantially higher impedance. Figure 5-2 shows the 944H collector operated in the no RF, sun on mode. Under these conditions electrode number four achieves the highest temperature (278°C). This follows because without the effect of RF defocusing most of the electron beam impinges on collector electrode four. Thus, the total beam power dissipated in the collector is nearly the same with or without RF drive.

The 985H, with RF power output of 200 W at 85 GHz, exhibited the lowest efficiency hence greatest collector dissipation of the TWTs of this study program. Figure 5-3 shows the thermal characteristics of the 985H post supported collector (RF on, sun on). Collector electrode number one achieves a temperature of 670°C. As cited, in an effort to reduce collector temperature, an alternate design, called the cage collector, was formulated. Figure 5-4 is the thermal profile for the cage collector with RF on and sun on. Comparison with Figure 5-3 shows a reduction in temperature of about 6.5%. This results from an improved internal view factor.

Table 5-1 includes the hot spot temperature of the 944H with various operating modes. Table 5-2 gives the hot spot temperatures for the 942H, 943H and 985H for different operating conditions. Thermal power conducted to the spacecraft is included in the thermal diagrams of Figures 5-1 through 5-4 and is summarized for all TWTs in Tables 5-1 and 5-2. Conducted thermal power is seen to be maximum with RF on and sun on. The former causes increased collector interception power on the forward, higher potential, collector electrodes.

Since collector electrode temperatures are quite high, especially for the 200 watt RF power output TWTs, special care must be exercised in

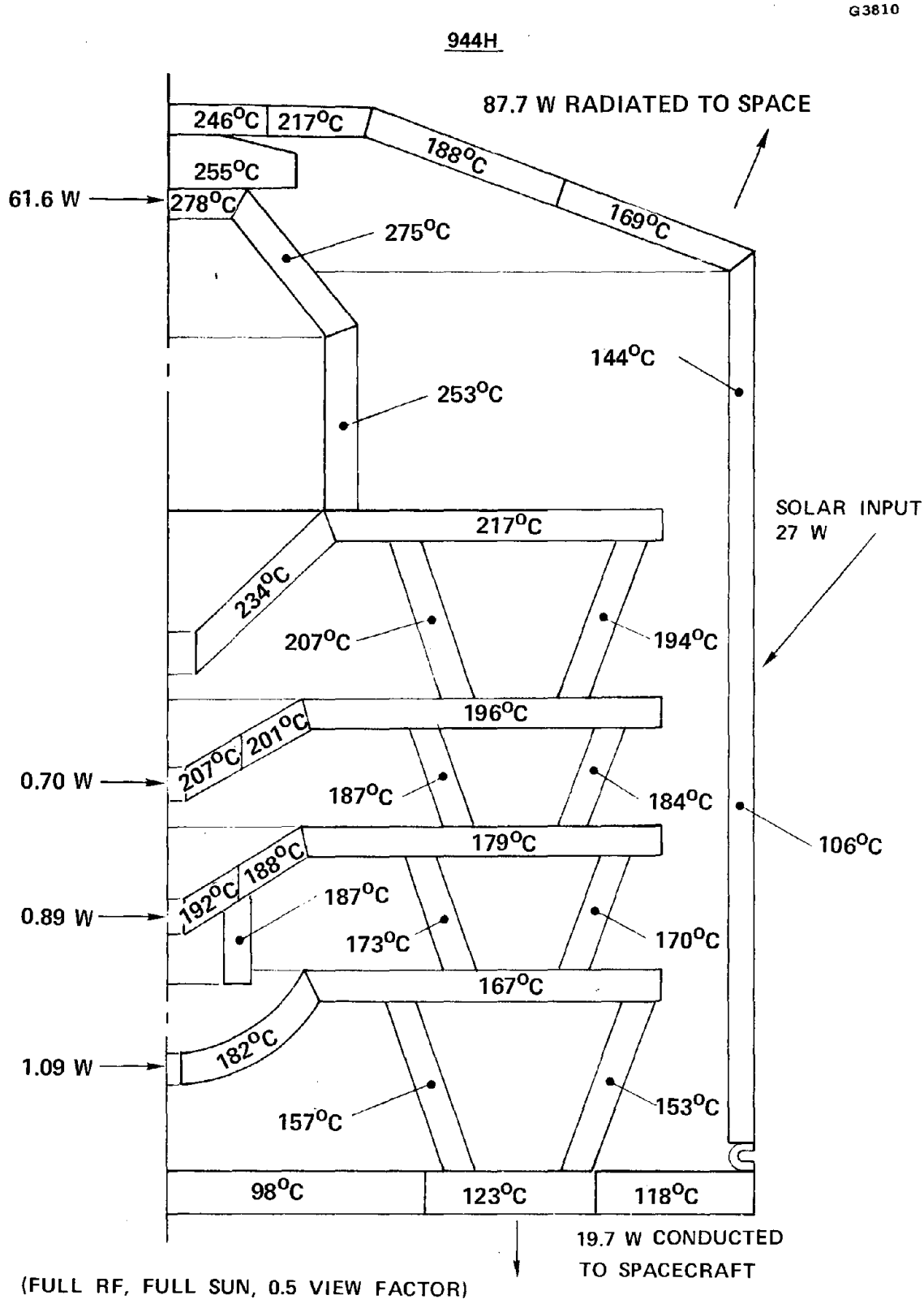

Figure 5-2 944H thermal analysis of collector post supported configuration space view factor 0.5, no rf, sun on.

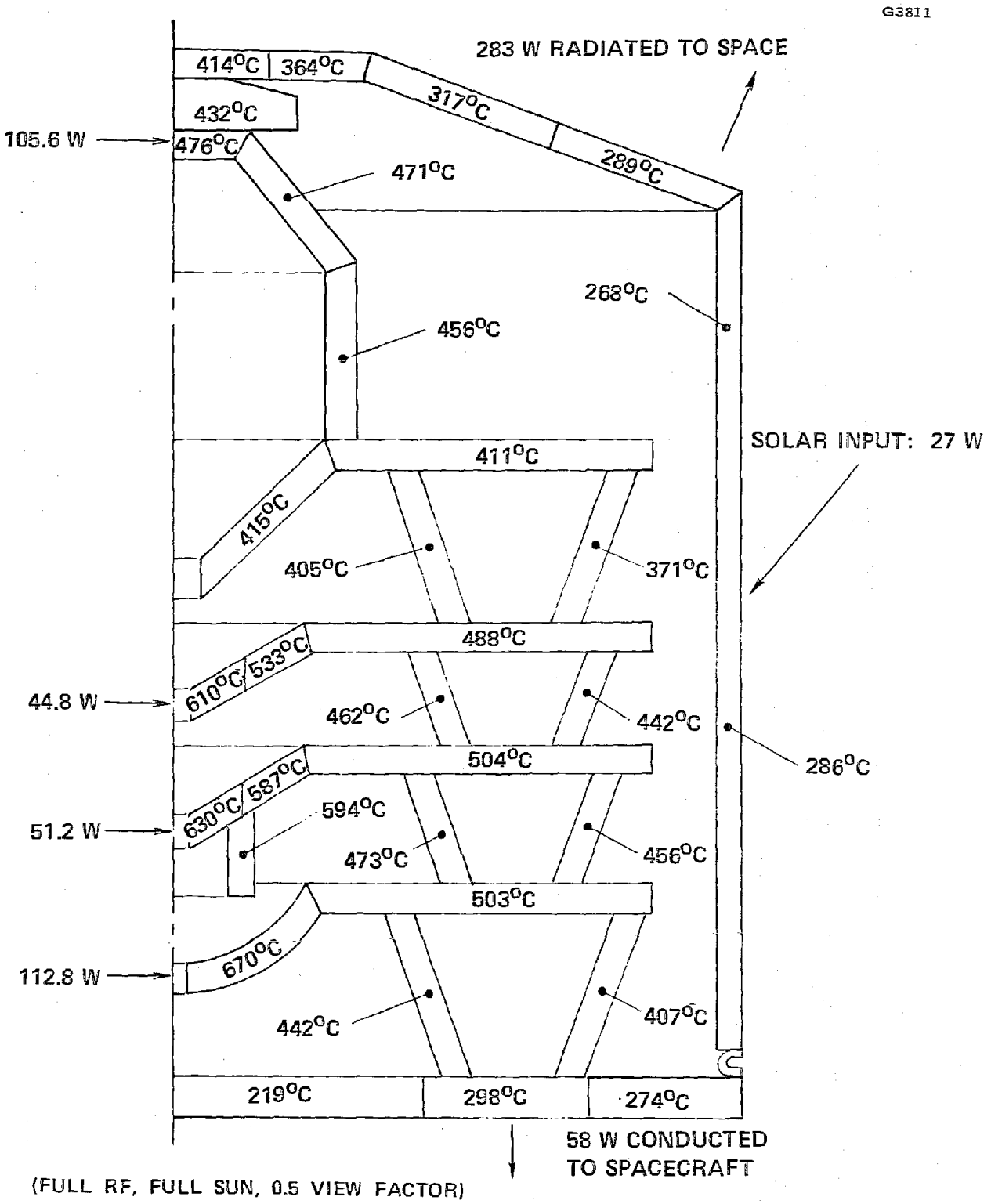

Figure 5-3 985H post supported cotlector thermal analyses. Spare view factor 0.5, RF on, sun on.

TABLE 5-1

944H COLLECTOR THERMAL ANALYSIS SUMMARY

Radiated to Space (W)	Conducted to Spacecraft (W)	Hot Spot (°C)	Full RF	Sun	View Factor
55.2	8.8	269	Yes	No	1.0
78.3	12.6	283	Yes	Yes	1.0
71.2	19.7	307	Yes	Yes	0.5
73.0	5.0	211	No	No	1.0
96.3	8.6	232	No	Yes	1.0
87.7	16.4	278	No	Yes	0.5

TABLE 5-2

942H, 943H AND 985H COLLECTOR THERMAL ANALYSIS SUMMARY

TWT	Radiated to Space (W)	Conducted to Spacecraft (W)	Hot Spot (°C)	Full RF	Sun	View Factor
942H (42.0 GHz, 100 W)	117	23	440	Yes	Yes	1.0
	109	31	463	Yes	Yes	0.5
	113	22	341	No	Yes	0.5
943H (42.0 GHz, 200 W)	184	35	588	Yes	Yes	1.0
	174	44	611	Yes	Yes	0.5
	224	37	560	No	Yes	0.5
985H* (85.0 GHz, 200 W)	296	45	607	Yes	Yes	1.0
	285	56	631	Yes	Yes	0.5
	206	38	485	No	Yes	0.5

*Cage collector configuration

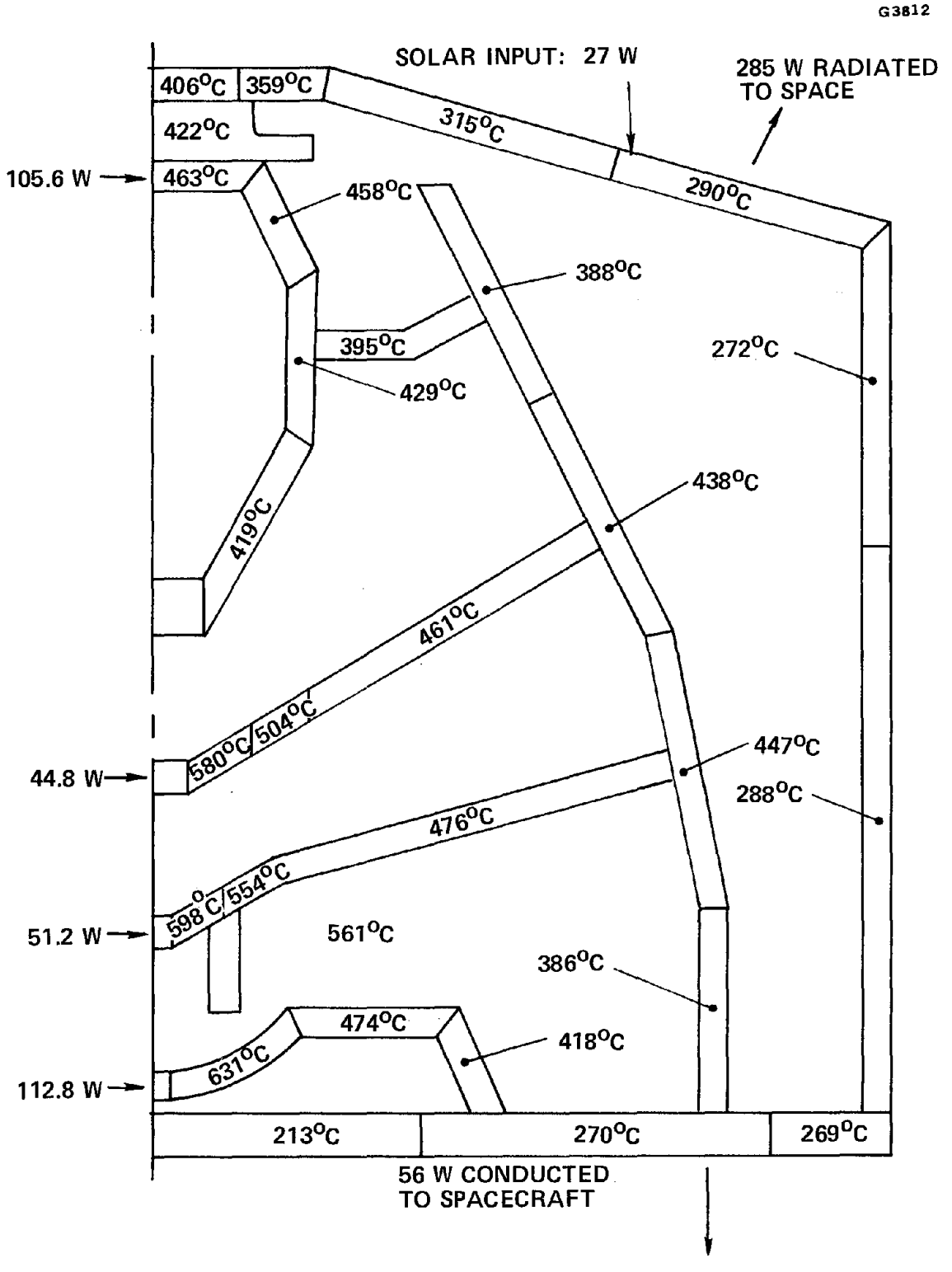

Figure 5-4 985H cage supported collector thermal analyses. Space view factor 0.5, RF on, sun on.

electrode material selection and processing. Molybdenum is proposed as the electrode material. These electrodes will be subjected to a high temperature (750°C) vacuum firing prior to assembly. During TWT processing, the highest feasible "bakeout" temperature will be employed, (500-550°C). In addition a substantial period of electron beam processing, both with dc only, and with RF drive will be employed. All TWTs will include vacuum-ion pumps which will always be operating when the TWT is on.

Page Intentionally Left Blank

6.0 DISCUSSION OF RESULTS

The present design study of the four TWTs at 42 and 85 GHz relied both on detailed analytical work that has been empirically corroborated and on design and construction techniques that have been successfully demonstrated with practical devices at the Electron Dynamics Division of Hughes Aircraft Company. A high degree of confidence is therefore ascribed to the performance predictions and on the manufacturability of these tubes.

The RF designs were established by a rather extensive optimization of beam and circuit parameters, as outlined in Section 3.1.3. All the major performance objectives were met, although the calculated values of output power for the 942H and 943H were 50 percent higher than specified (the initial estimate of the basic efficiency turned out to be too low). A design modification to reduce the output power would have involved changes in the gun parameters, if the same degree of optimization was to be maintained. This was not carried through because the program schedule and effort could only accommodate one complete gun design per tube. Based on the RF designs that were developed, however, the following features would be expected for lower-power versions of the 942H and 943H respectively (having a minimum output power of about 100 W and 200 W over the band 41-43 GHz): beam voltages of 16 KV and 18.5 kV; minimum basic efficiencies of 13.3 and 14.3 percent; and minimum overall efficiencies of 41 and 43 percent.

Further refinements of the RF design of all four TWTs could be made, particularly concerning the selection of the center frequency phase shift value and the cold circuit bandwidth. It is unlikely that any significant performance improvement would be obtained in this way for the 42 GHz tubes. For the 85 GHz device, however, additional design work is definitely warranted before such a tube is committed to full development. This

would involve experimental circuit studies, which are particularly needed because of the near-merging of the fundamental and slot modes. The studies should explore the effect of changes in the basic circuit design (phase shift per cavity and cold bandwidth) on the hot bandwidth, interaction efficiency, and RF dissipation. Also, depending on the system and mission requirements, an investigation with a different operating voltage and cathode loading may be even more fruitful, as is indicated by the results presented in Appendix B. Detailed thermal analysis of the design of the internal termination in the 85 GHz circuit should also be performed.

The efficiency improvement due to the multi-stage depressed collector is substantial. This is primarily a result of the favorable spent beam energy distribution that is produced in a TWT with weak RF interaction and low perveance beam. An increase from the basic efficiency by a factor of approximately three was estimated for the 42 GHz tubes and a factor of five for the 85 GHz tube. These estimates are quite compatible with a demonstrated improvement factor of four in a closely related W-band TWT that has been developed at Hughes, but the estimates are generally believed to be conservative. No attempt was made to take into account the effect of the special shield on the first depressed stage. The shield makes it possible to depress this stage somewhat more, without increasing the body current, compared to the operation of the collectors that have been experimentally evaluated.

The thermal and mechanical designs are generally similar to the approaches used in existing devices. An exception is the cage-type support of the collector elements on the 85 GHz tube, which was adopted to eliminate the extra thermal impedance that would otherwise have been present due to the shadow effect of more conventional support posts.

7.0 SUMMARY OF RESULTS

A design study of four traveling-wave tubes for use in space was completed. Tube performance objectives included CW output powers of 100 to 200 W minimum at 42 and 85 GHz over a bandwidth of 0.5 or 2 GHz. Characteristics of primary interest were high efficiency, low weight, and long life.

The designs featured coupled cavity RF circuits with phase velocity tapered output sections for high interaction efficiency; multi-stage collectors with three depressed elements for high overall efficiency; periodic permanent magnet (PPM) focusing for low weight; and a low cathode current density of $1 A/cm^2$ for a minimum life of two years. The program effort encompassed: 1) detailed electron gun design; 2) complete RF circuit design including matching development at scaled frequencies; 3) design of PPM focusing stack and spent beam refocusing section; 4) detailed design of radiation cooled collector including mechanical and thermal analysis; and 5) conceptual tube package design with conduction cooled tube body. The intended tube manufacturing approach follows established procedures used in the construction of millimeter wavelength TWTs at Hughes.

The principal performance features of the four derived designs are summarized in the following table:

Design	Nominal Frequency Range	Minimum Output Power	Operating Voltage	Minimum Overall Efficiency
1	41-43 GHz	150 W	17 kV	42%
2	41-43 GHz	300 W	21 kV	45%
3	42-42.5 GHz	100 W	14.5 kV	45%
4	84-86 GHz	200 W	25 kV	25%

Page Intentionally Left Blank

APPENDIX A

FREQUENCY VS PHASE AND IMPEDANCE MEASUREMENTS

The experimental circuit development work in this study was performed at C-band frequencies with scaled circuit parts. It included establishing the frequency vs phase ($\omega\beta$) characteristics of the cavity circuits, to be discussed in this Appendix. It also included the development of RF windows and impedance matches to RF waveguides and terminations; this effort is described in Sections 3.6 - 3.8.

Although resonant $\omega\beta$ measurements may be made with any suitable frequency scale factor, the match development is most conveniently done using a standard waveguide size. The waveguide height can be changed by a step transformer, for which reliable analytical design techniques are available. By choosing a scale factor that is the ratio of the widths of two standard waveguides, a match design developed for one waveguide can thus be immediately adapted to the second waveguide for the correspondingly scaled frequency range.

In the present study the $\omega\beta$ experiments were performed with scale factors appropriate to the matching development. The same cavity parts could therefore be used for both efforts. Table A-1 lists the standard waveguides that were relevant and the scale factors involved.

In the theoretical analysis the cold bandwidth and the phase shift per cavity at midband were established for each design by small signal gain calculations (Section 3.2.1). Cold test cavities were then designed to determine, by iteration experiments, the final cavity configuration that would provide the desired bandpass characteristics.

TABLE A-1

WAVEGUIDES AND SCALE FACTORS USED IN THE DESIGN STUDY

Waveguide	Nominal Freq. Range, GHz	Inside Width cm (in.)	Scale Factor	Tube Design
WR-137	5.4-8.2	3.485 (1.372)	-	-
WR-22	33-50	0.569 (0.224)	6.125	944H
WR-19	40-60	0.478 (0.188)	7.30	942H, 943H
WR-10	75-110	0.254 (0.100)	13.72	985H

Table A-2 summarizes all the basic $\omega\beta$ circuits that were measured, while Figure A-1 is a plot of the cold bandwidth, B_c*, as a function of the coupling hole angle, θ, for the same circuits. It may be noted that the slope of B_c versus θ is virtually identical for all the 42 GHz tubes. Similar experience in the past made it possible to reduce the number of angle variations to two for these tube designs. The 85 GHz circuit deviated from the general trend; this was related to the proximity of the slot mode to the fundamental cavity mode.

*The fractional cold bandwidth B_c is defined by

$$B_c = 2(f_u - f_e)/(f_u + f_e)$$

where f_u and f_e are the upper and lower cutoff of the passband.

TABLE A-2

SUMMARY OF $\omega\beta$ MEASUREMENTS

Tube	Design Objective		Circuit Number	Coupling Hole Angle, θ (°)	Gap to Period Ratio g/ℓ_c	Cold Bandwidth, B_c (%)	Measured at Phase ϕ_o	
	Scaled Freq. (GHz)	Phase, ϕ_o (rad)					Frequency (GHz)	Impedance, K (Ω)
942H	5.75	1.40π	1	120	0.250	21.0	6.10	22.3
			2	150	0.288	35.6	5.72	13.2
943H	5.75	1.37π	1	120	0.250	19.9	6.11	27.1
			2	153	0.298	36.2	5.67	15.6
			3	153	0.312	36.5	5.76	15.0
944H	6.90	1.25π	1	120	0.242	22.5	6.89	30.6
			2	130	0.275	27.3	6.85	25.7
			3	130	0.282	27.3	6.88	26.6
			4	130	0.284	27.3	6.89	26.3
985H	6.20	1.42π	1	120	0.300	26.7	5.86	4.26
			2	135	0.399	36.7	5.89	3.22
			3	135	0.429	37.6	6.00	3.20
			4	120	0.358	28.0	6.16	4.20
			5	125	0.393	31.4	6.17	3.78
			6	125	0.398	31.6	6.19	3.79

The iteration pattern is illustrated for the 943H circuit by the curves in Figure A-2. The object here was to achieve a cold bandwith of 35 percent with the $\omega\beta$ curve passing through the design phase shift of 1.37π at the scaled operating midband frequency of 5.75 GHz, indicated by a cross in the figure. The first circuit was designed with small coupling hole angle (120°) and undersize gap. This established one point on the B_c versus θ diagram. Anticipating the slope, it was expected that a 35 percent bandwidth would be achieved with an angle of 153°. The gap was also increased at the same time to make the second iteration closer to the final design. The measured $\omega\beta$ had a cold bandwidth of 36.2 percent and was still a little low in frequency. The third circuit was raised in frequency by opening up the gap some more. This increased the cold bandwidth slightly, while the frequency centering was now close enough so that the final design, given in Figure 3-17, could be determined from these results.

A similar procedure was carried out for the 942H and 944H circuits. One useful property that was utilized is the near-constancy of the fractional bandwidth with gap dimension. Thus in Figure A-1 one data point represents more than one measured circuit in some instances. This made it possible to establish the angle first, independently of the gap. Another useful property is that Pierce's interaction impedance, at a given phase shift per cavity, is also approximately independent of the gap. Calculations of tube performance based on measured data could therefore be started before the final tuning of the gap dimension had been completed. Both these general properties are apparent in Table A-2. The variations of interaction impedance with gap that occur reflect measurement uncertainties more than actual systematic trends.

The $\omega\beta$ properties of the 985H circuit were less predictable in advance because of the unusually large beam hole in relation to the cavity

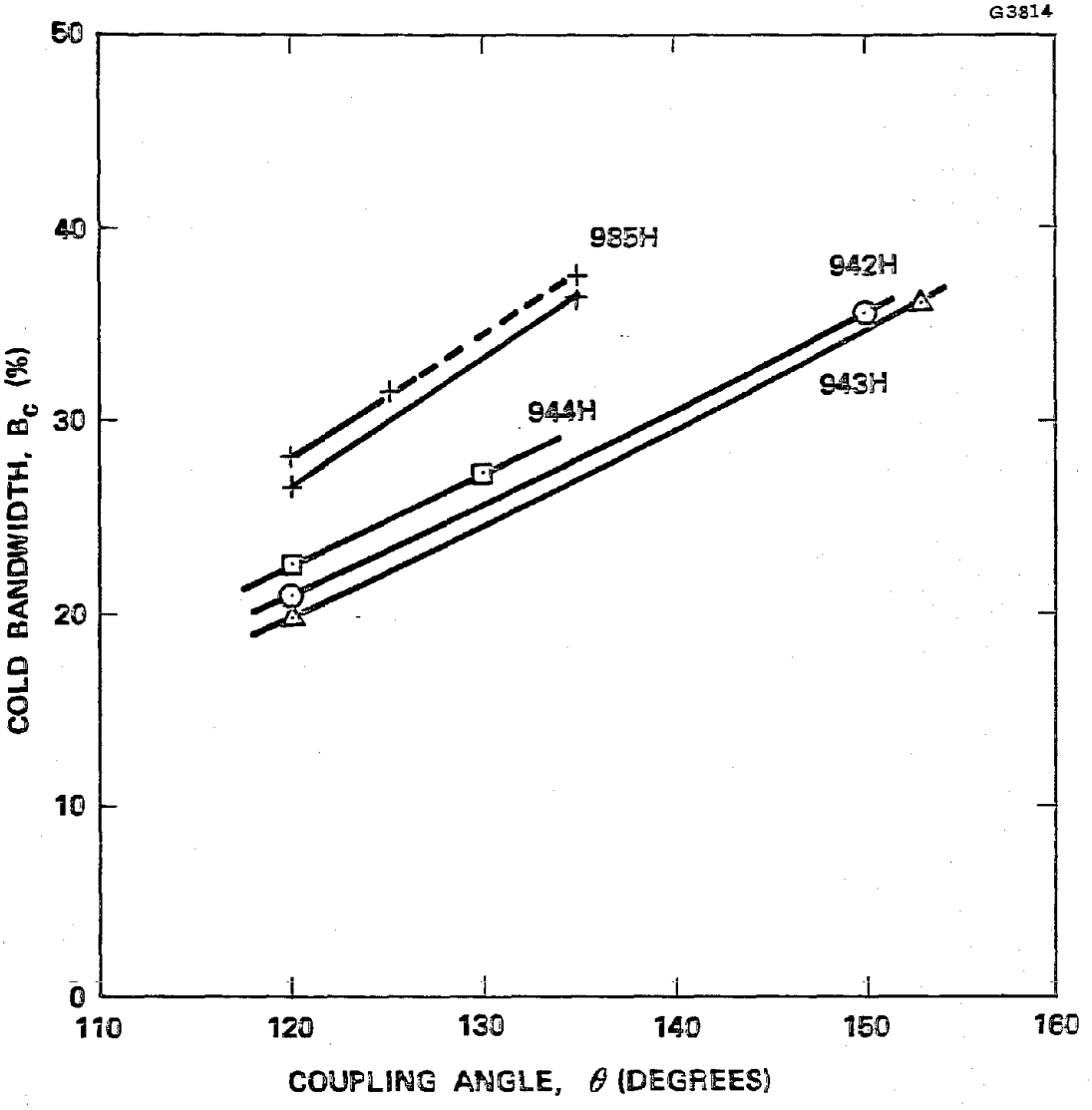

Figure A-1 Measured cold bandwidth vs coupling hole angle.

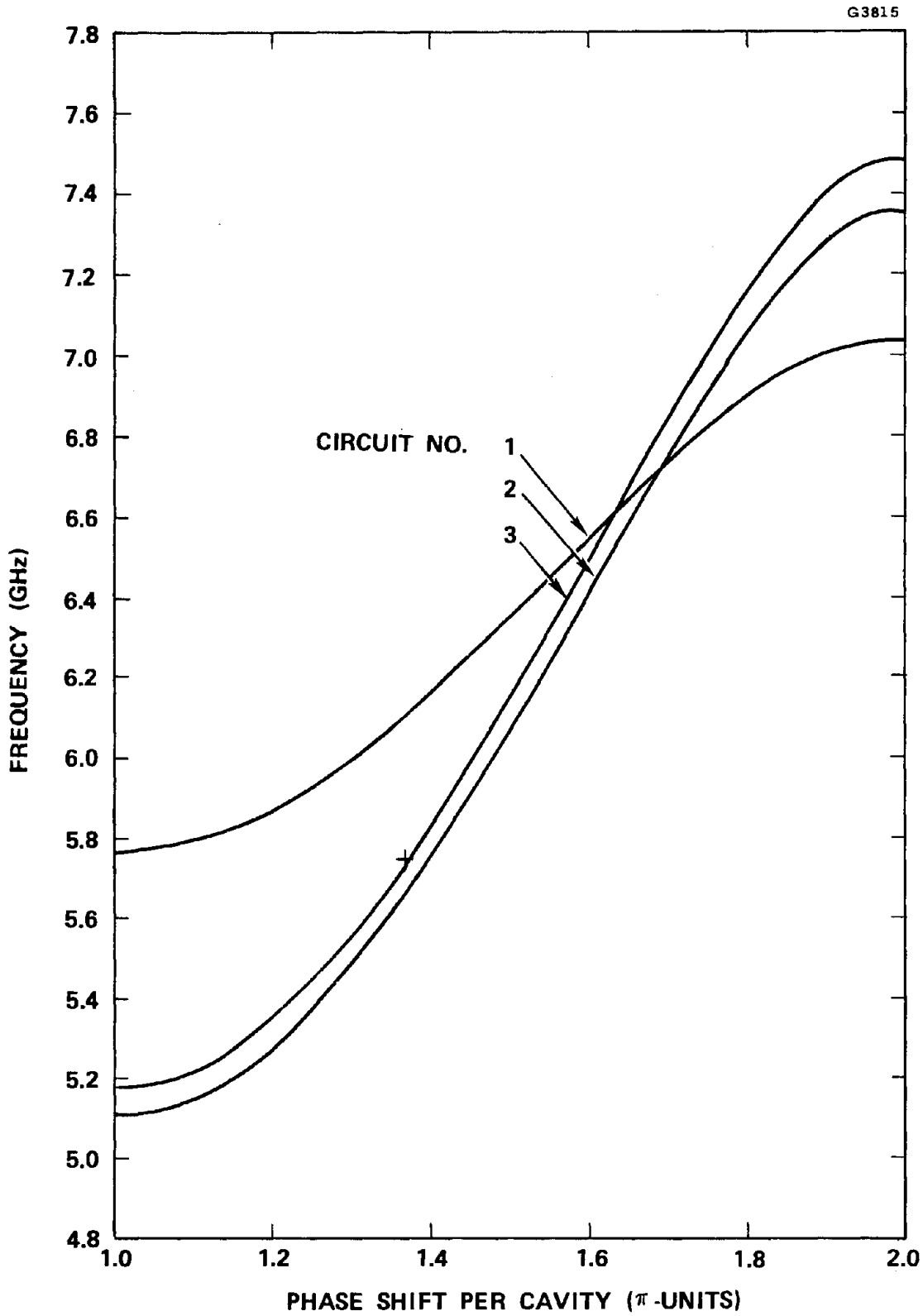

Figure A-2 Frequency vs phase curves measured during development of the 943H circuit. The cross indicates the design point.

diameter and the more stringent limitation on the cold bandwidth that resulted. Figure A-3 exhibits the relative cavity aspects of the 944H and the 985H, with the dimensions normalized to the same cavity diameter. The 942H and 943H cavity configurations fall in between these two. From the trend in the cavity configuration, the data points for the 985H in Figure A-1 might be expected to lie below the 943H level, but actually they did not.

A total of six circuit configurations were measured for the 985H. The frequency response of three of these is displayed in Figure A-4. The initial attempt was to achieve 35 percent cold bandwidth with the scaled operating midband of 6.20 GHz at a phase shift of 1.42π. In the second circuit configuration, with a coupling aperture angle of 135°, the bandwidth was 36.7 percent, but the frequency was too low. The slot mode was already so close that it was realized that the circuit could not be raised to its design frequency without going into mode cross-over. This is a condition in which the TM_{01} cavity resonance becomes the low frequency cutoff of the next higher mode (which is now the cavity mode), while a stopband again develops between it and the lowest mode (which is now primarily associated with the slot). There are two reasons why such a condition is undesirable. First, the bandwidth of the lowest passband is reduced, since it is maximum when the modes merge. Second, the phase velocity at the cavity resonance frequency, which is associated with a high impedance, moves close to the electron velocity, and an instability might easily develop.

Consequently a second set of 985H cavity parts were acquired, circuit number 4, which had an initial angle of 120° but a gap that achieved better frequency centering than circuit number 1. The first set of parts was used to define the merged mode condition with the 135° angle (circuit number 3), as seen in Figure A-5. From these data it was

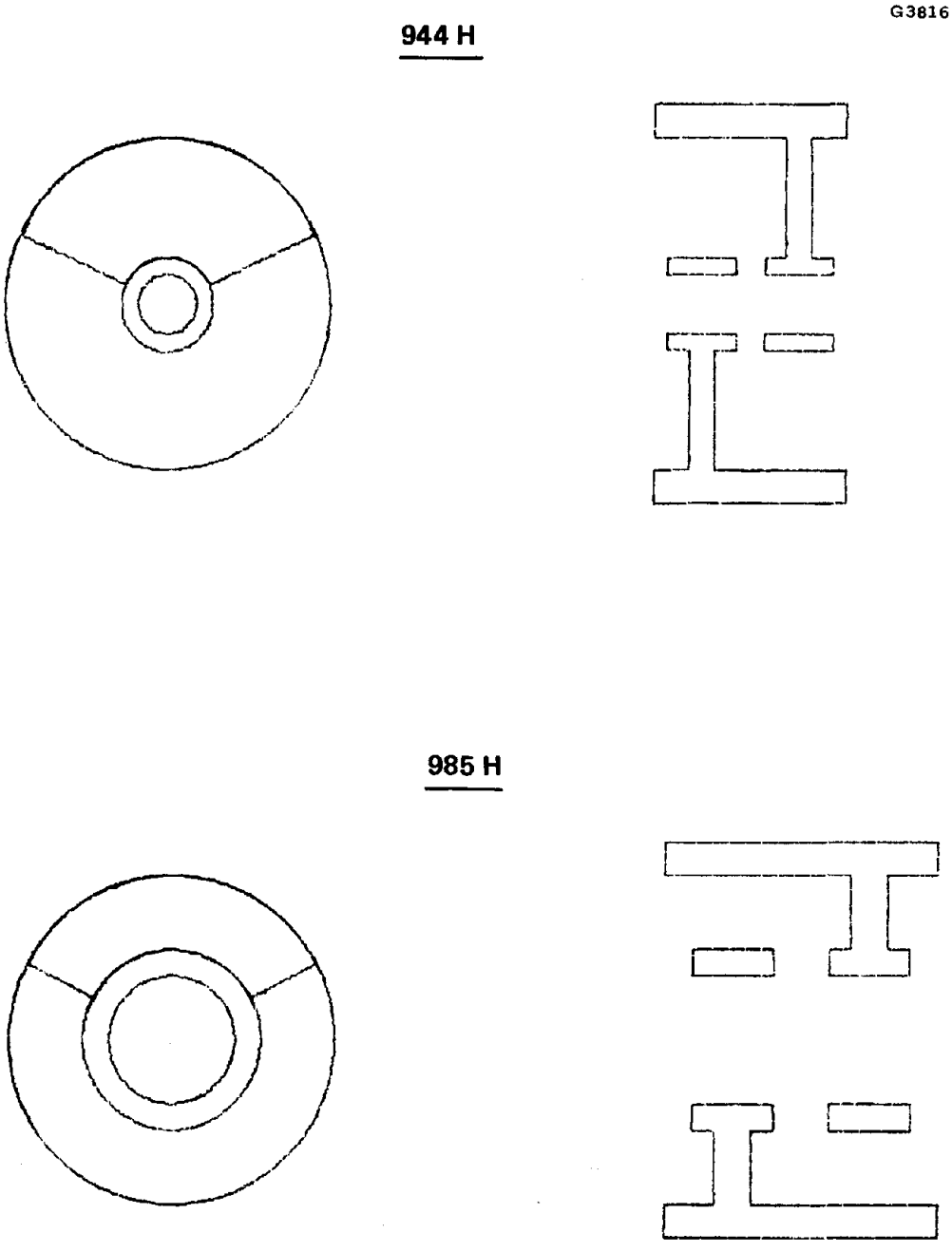

Figure A-3 Cavity aspects of the 944H and 985H with normalized cavity diameter.

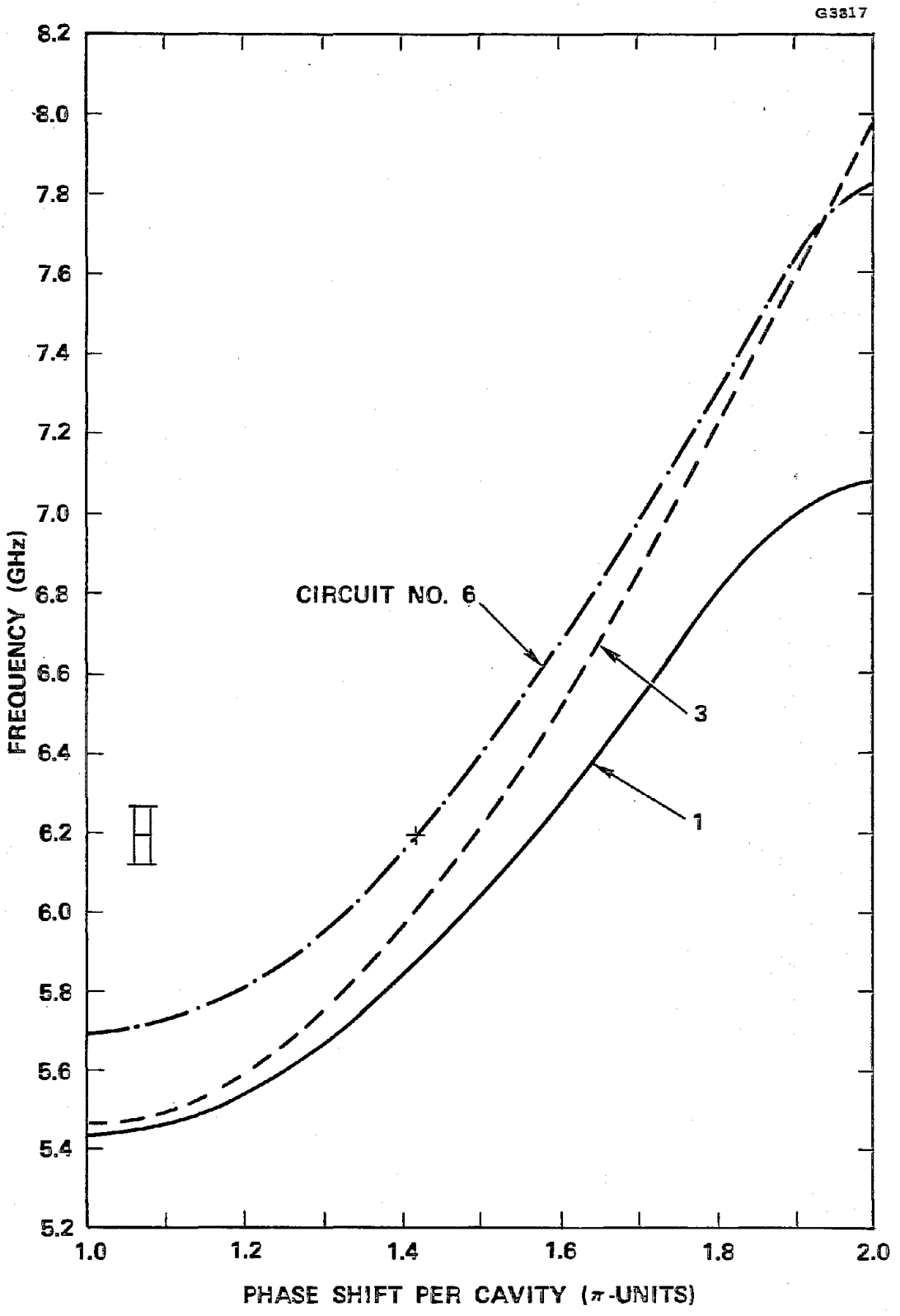

Figure A-4 Some frequency vs phase curves measured during development of the 985H circuit.

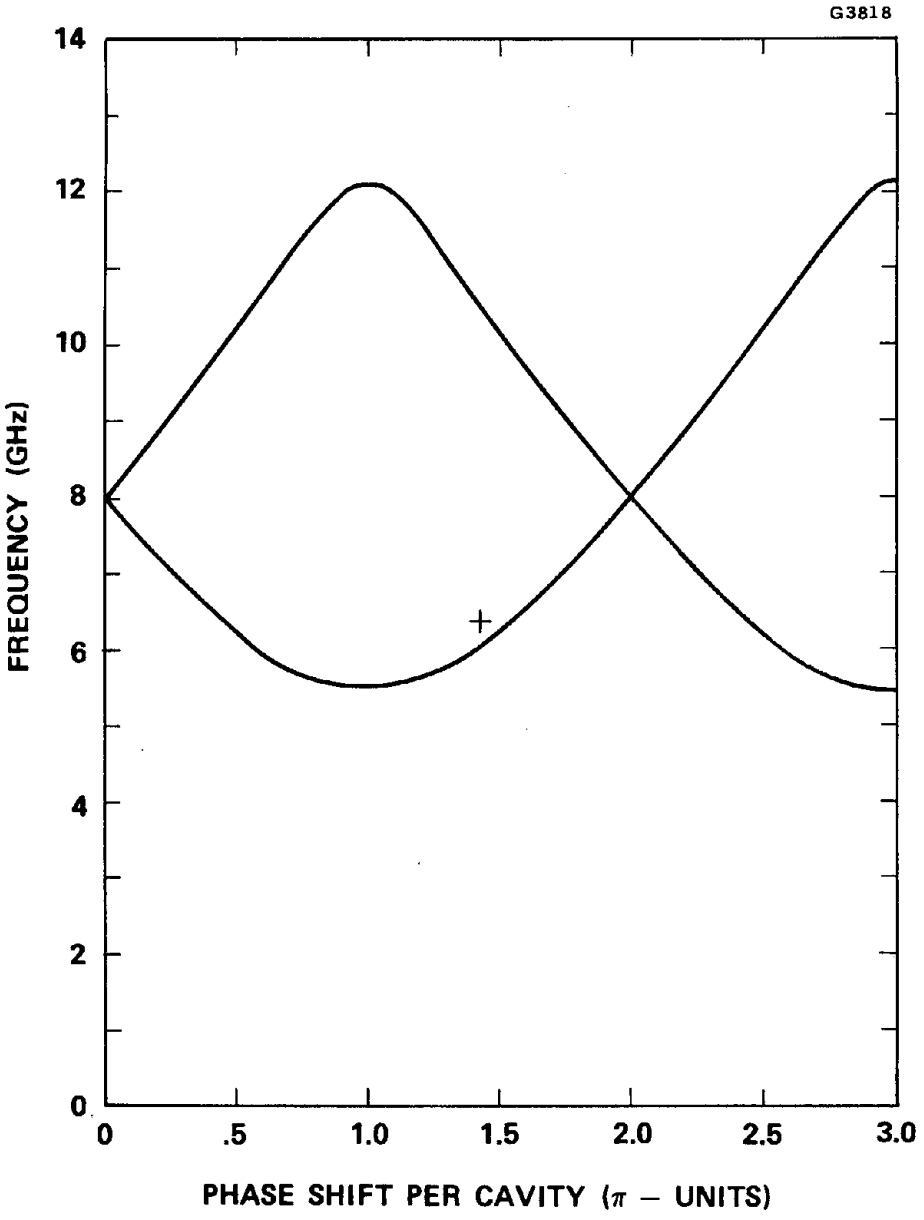

Figure A-5 The two lowest modes at the merged mode condition of a 985H circuit with 135° coupling hole angle (circuit number 3).

determined that the maximum cold bandwidth, with merged modes and proper placement in frequency, was about 34 percent. By small signal gain calculations it was thereafter found that the maximum performance bandwidth occurred with a cold bandwidth of approximately 31 percent (Section 3.2.1). In the final design, with an angle of 125°, the measured cold bandwidth was 31.6 percent.

Figures A-6 and A-7 present samples of measured resonance frequency data taken on a 943H circuit and a 985H circuit respectively. The Pierce interaction impedance, calculated from dielectric rod perturbation measurements assuming a beam filling factor of 0.42, is plotted in Figure A-8 for the 943H and in Figure A-9 for the 985H. The depicted results were actually obtained for the next-to-the-last circuit iteration in each case. As was mentioned, however, the Pierce impedance of the final circuits, which differ only by a small change in the gap dimension, is the same within measurement uncertainties.

The taper cavities for all these tubes had the same coupling aperture angle and web thickness as the corresponding standard cavities. To reduce the phase velocity the cavity height was made smaller such that the change in cavity period was in proportion to the desired change in velocity. This assumed that the frequency versus phase characteristics of the taper cavities were identical to those of the standard cavities. The actual $\omega\beta$ characteristics of the tapers had somewhat larger bandwidths, but when the curves were matched up at the center operating frequency the deviation from the standard curve over the operating band was negligible.

The $\omega\beta$ measurements for the taper circuits were made with a minimum number of parts. A resonating structure consisting of either two full cavities and two half cavities at either end were used or, in the case

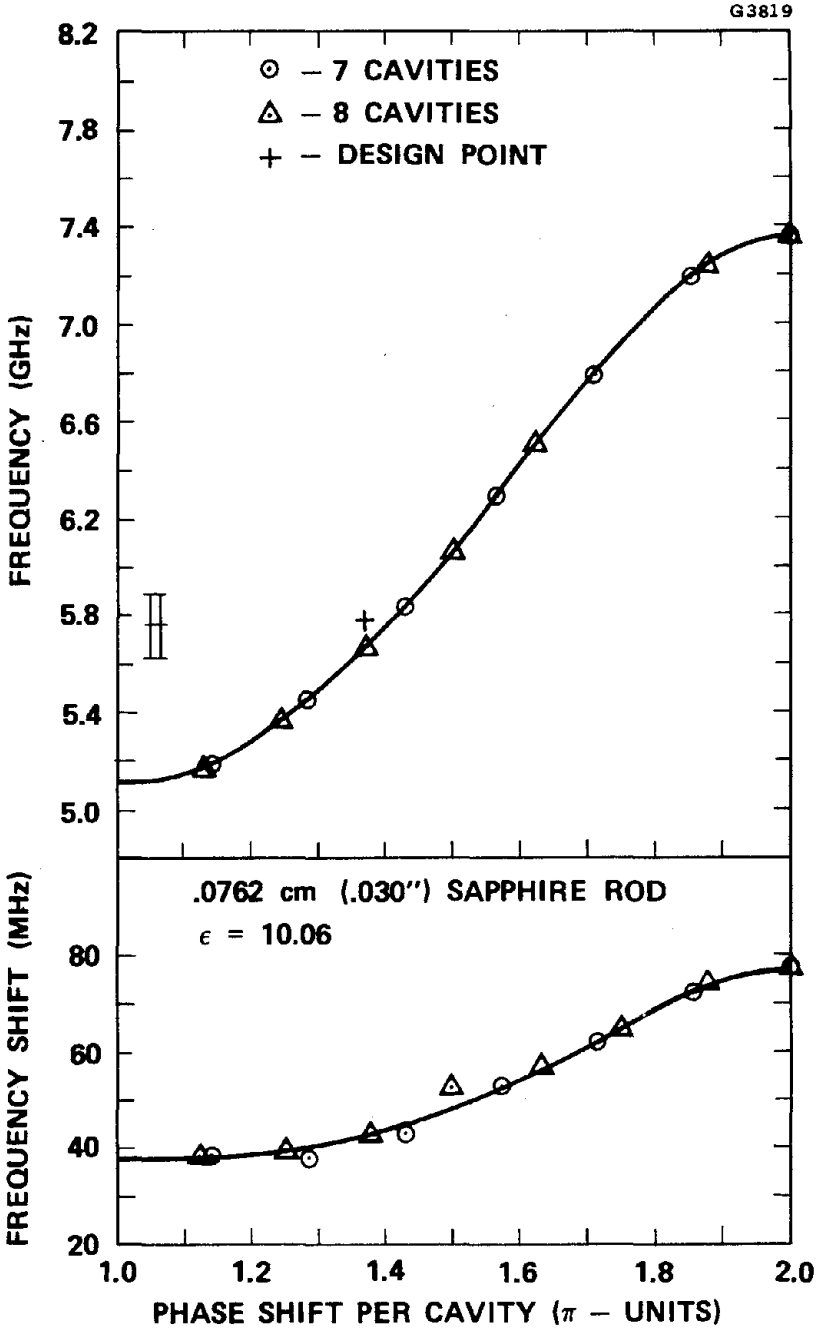

Figure A-6 Data of resonance frequencies and frequency shifts with dielectric rod perturbation taken on the second 943H circuit.

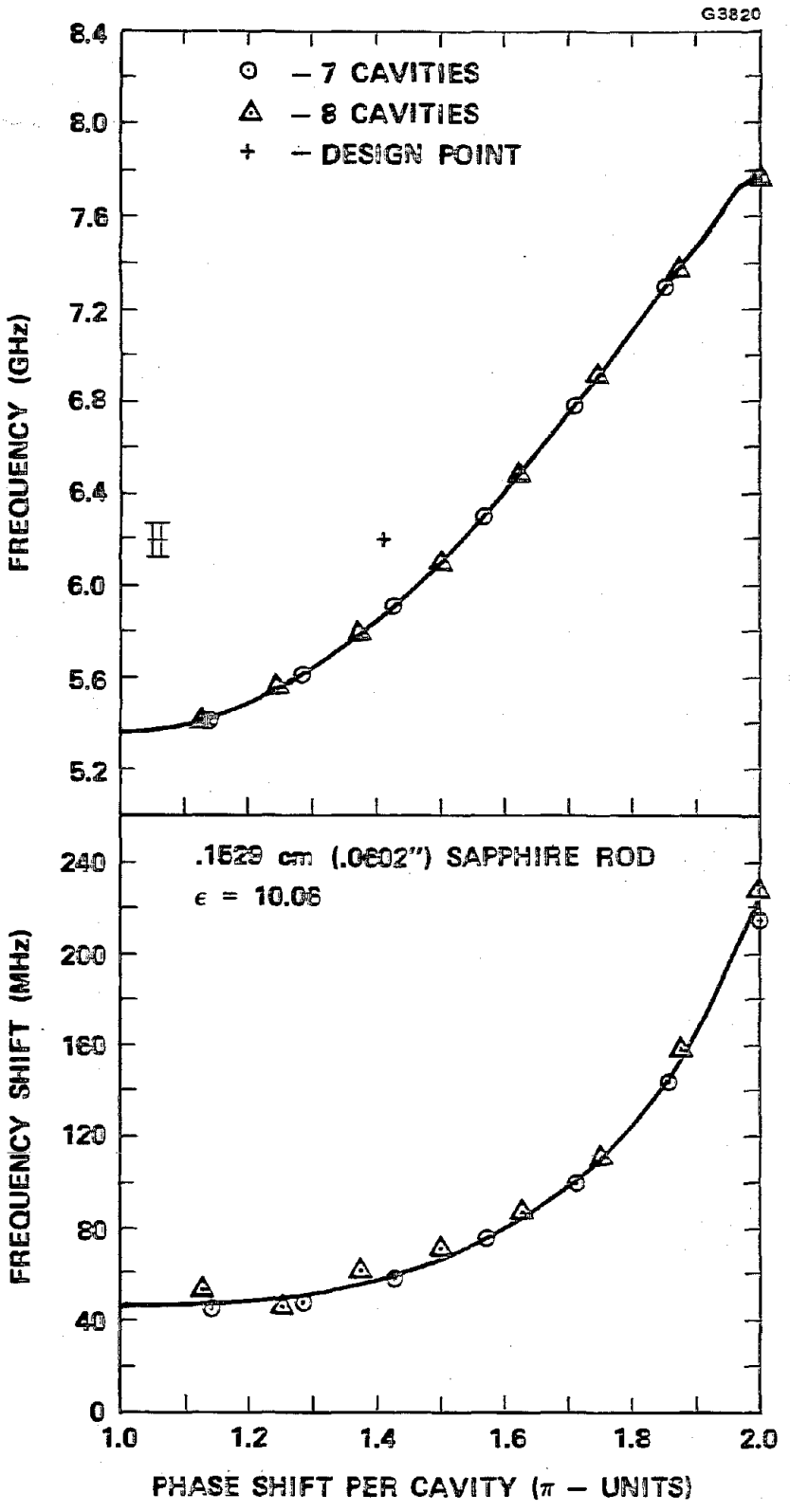

Figure A-7 Data of resonance frequencies and frequency shifts with dielectric rod perturbation taken on the second 985H circuit.

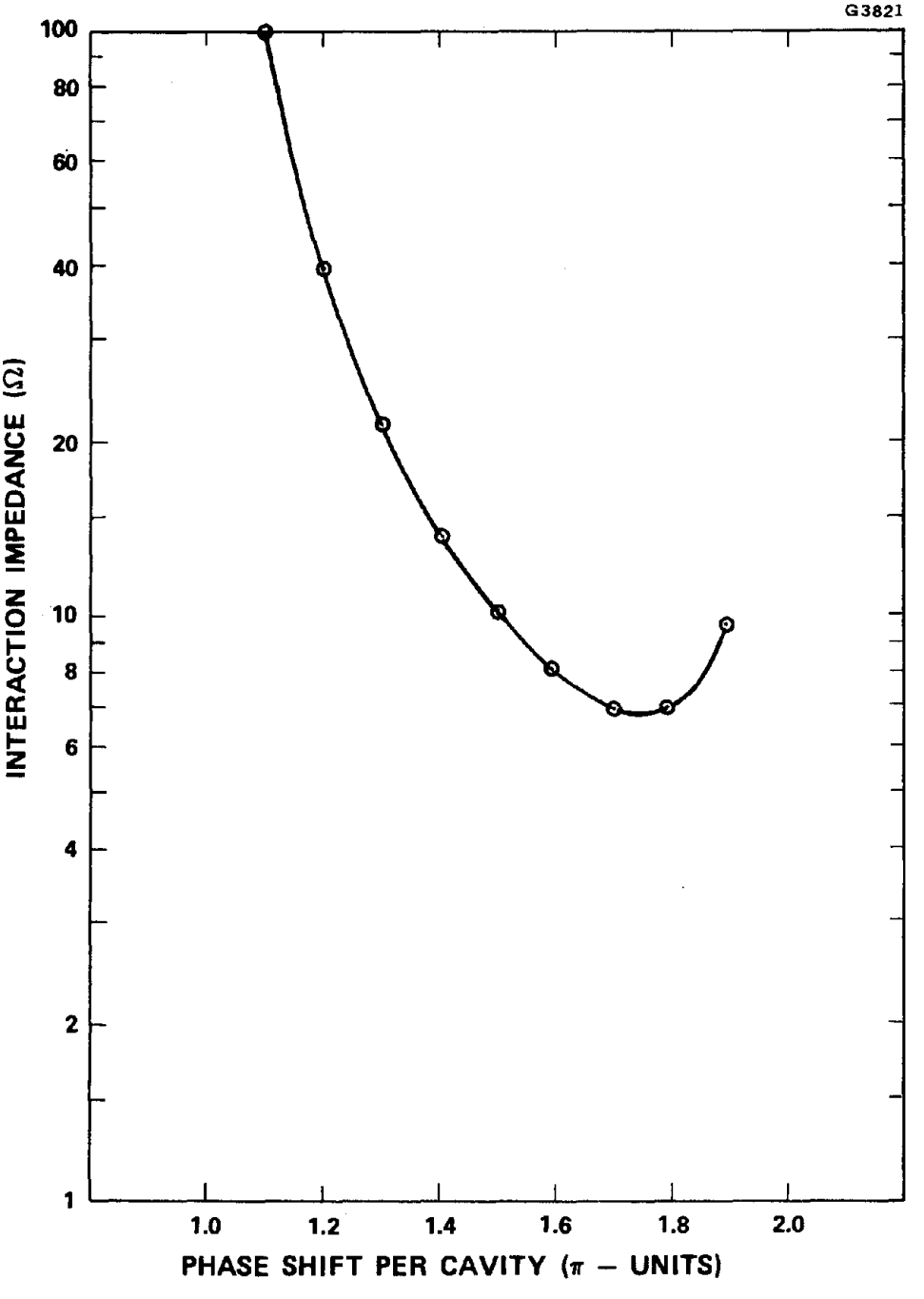

Figure A-8 Measured Pierce's interaction impedance of the 943H (circuit number 3).

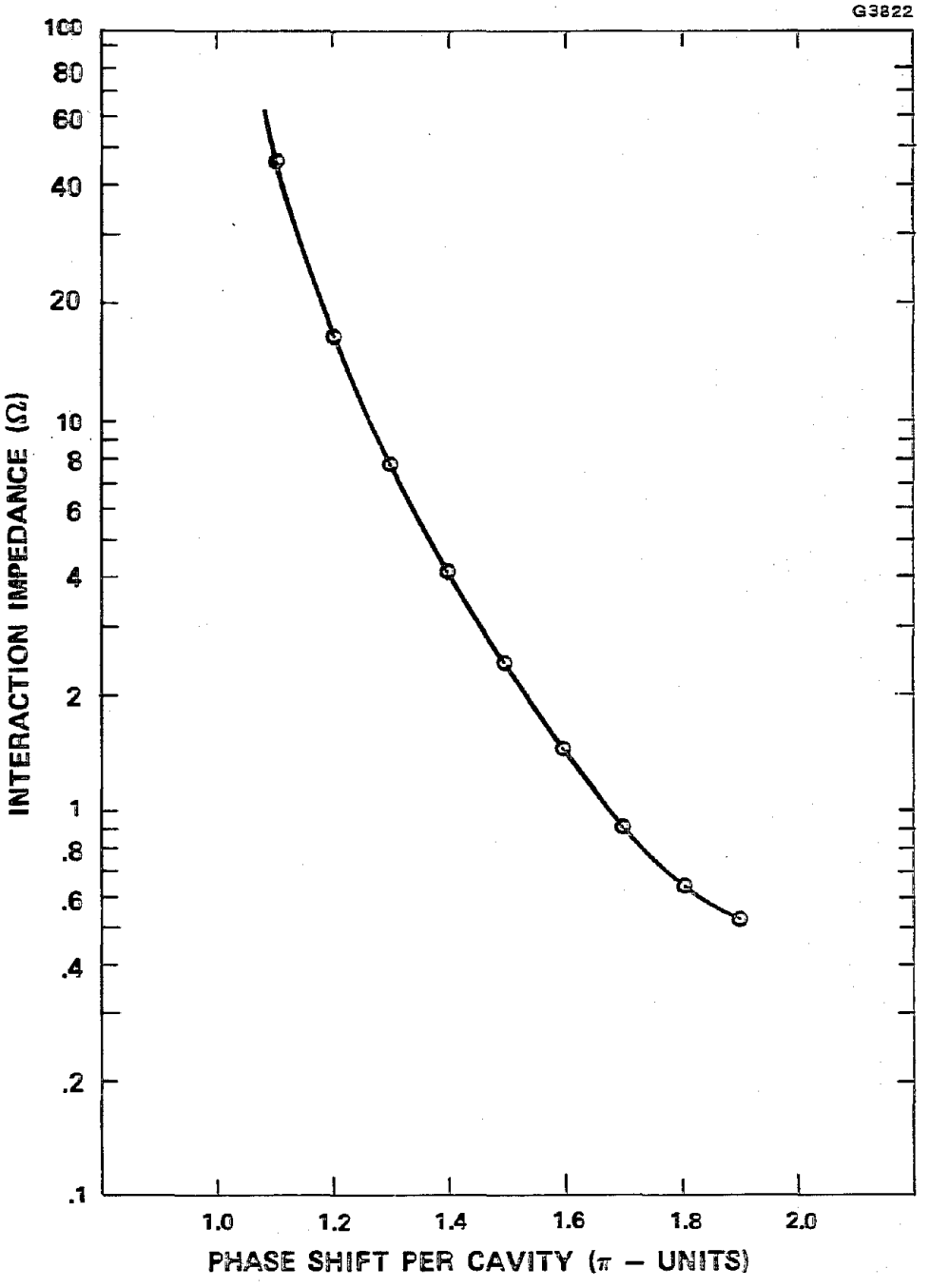

Figure A-9 Measured Pierce's interaction impedance of the 985H (circuit number 5).

of the 944H, a stack with four full cavities. One reason for the last choice was that the operating center frequency for the 944H was located at a phase shift of 1.25π which was directly measured with four full cavities. Since the main effort here was to match up the ωβ curves of the taper and standard circuits at the center frequency, the data from the taper cavities were compared to data taken on a similar short resonating structure of standard cavities. Errors due to miscellaneous end effects were thereby minimized.

The dimensions of the last cavity configuration in the ωβ development of each tube are listed in Figure A-10. No measurements were made on taper cavities for the 942H. The dimensions given in Figure 3-17 for these cavities were best estimates based on experience with the 943H taper development.

G3823

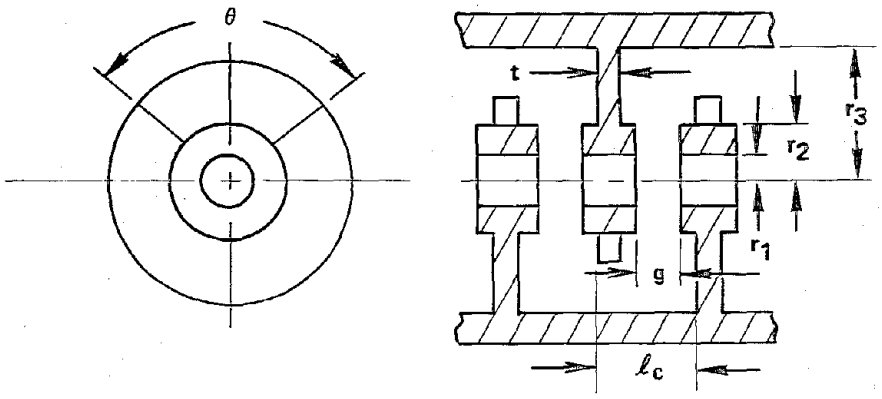

TUBE	942H	943H	944H	985H
SCALE FACTOR	7.30	7.30	6.125	13.72
$2r_1$ – cm (in.)	.4597 (.1810)	.4821 (.1898)	.3673 (.1446)	.9271 (.3650)
$2r_2$ – cm (in.)	.7564 (.2978)	.7788 (.3066)	.5850 (.2303	1.310 (.5159)
$2r_3$ – cm (in.)	2.303 (.9067)	2.251 (.8862)	2.060 (.8110)	2.398 (.9438)
θ – rad (°)	2.618 (150)	2.670 (153)	2.269 (130)	2.182 (125)
t – cm (in.)	.2040 (.0803)	.2225 (.0876)	.1554 (.0612)	.2614 (.1029)
STANDARD CIRCUIT				
ℓ_c – cm (in.)	.8827 (.3475)	.9550 (.3760)	.6096 (.2400)	1.007 (.3965)
g – cm (in.)	.2540 (.1000)	.2977 (.1172)	.1732 (.0682)	.4013 (.1580)
FIRST TAPER:				
ℓ_c – cm (in.)	———	.9027 (.3554)	.5725 (.2254)	.9820 (.3866)
g – cm (in.)	———	.2725 (.1073)	.1575 (.0620)	.3861 (.1520)
SECOND TAPER:				
ℓ_c – cm (in.)	———	.8499 (3348)	.5370 (.2114)	.9568 (.3767)
g – cm (in.)	———	.2474 (.0974)	.1422 (.0560)	.3703 (.1458)

Figure A-10 Cavity dimensions of the final iteration of ωβ measurements.

Page Intentionally Left Blank

APPENDIX B
85 GHZ DESIGN WITH 2A/CM^2 CATHODE LOADING

The severe focusing constraint at 85 GHz resulted in a beam hole parameter of γa of 1.96 (Table 3-1). This large value of γa was the chief cause for the low interaction impedance and the low intrinsic interaction strength in the 985H. It directly affected the interaction efficiency and the performance bandwidth.

It was noted in Section 3.1.1 that the focusing field requirement is reduced with cathode size, or equivalently, with increased cathode loading. A variation of the 85 GHz design was evaluated in which the cathode loading was raised from 1 to 2 A/cm^2. This permitted a reduction of the γa parameter from 1.96 to 1.70. Assuming that the bandpass characteristics of the circuit remained unchanged, the resulting interaction impedance would be 50 percent larger. A small signal gain calculation for such a circuit showed that the performance bandwidth increased by 27 percent, while the output power was estimated to rise by 15 percent with a corresponding improvement in efficiency. If the circuit were redesigned with a smaller cold bandwidth to provide the original hot bandwidth, the efficiency would improve even more. Alternatively, a wider bandwidth performance could be achieved by increasing the cold bandwidth of the circuit. It should be noted that the maximum obtainable cold bandwidth, occurring at the merged mode condition, becomes larger as the beam tunnel is made smaller.

The performance improvement with a cathode loading of 2A/cm^2, compared to 1 A/cm^2, is substantial, although tube life would be impaired. The results illustrate the important role that the constraint of beam focusing plays in the design of PPM focused TWTs at high frequencies.

Page Intentionally Left Blank

REFERENCES

1. G. Herrmann, "Optical Theory of Thermal Velocity Effects in Cylindrical Electron Beams," J. Appl. Phys., vol. 29, p. 127 (1958).

2. C. C. Cutler and M. E. Hines, "Thermal Velocity Effects in Electron Guns," Proc. IRE, vol. 43, p. 307 (1955).

3. J. A. Christensen and I. Tammaru, "Development of a 200W CW High Efficiency Traveling-Wave Tube at 12 GHz," NASA Final Report CR-134734, Contract No. NAS 3-15831, October 1974

4. L. E. Brown, J. A. Christensen, R. H. LeBorgne, D. Radovich and I. Tammaru, "A High Efficiency, 100 Watt Space TWT for the Seasat 'A' Scatterometer," Proceedings of SOUTHEASTCON '77 (IEEE), p. 488, April 1977.

5. G. Herrmann, "Transverse Scaling of Electron Beams," J. Appl. Phys., vol. 28, p. 474 (1957).

6. I. Langmuir and K. B. Blodgett, "Currents Limited by Space Charge between Concentric Spheres," Phys. Rev., vol. 24, p. 49 (1924).

7. J. R. Pierce, "Rectilinear Electron Flow in Beams," J. Appl. Phys., vol. 11, p. 548 (1940).

8. W. B. Herrmannsfeldt, "Electron Trajectory Program," Stanford Linear Accelerator Center Report SLAC-166, September 1973.

9. H. K. Detweiler, "Characteristics of Magnetically Focused Large-Signal Traveling-Wave Amplifiers," RADC Technical Report TR-68-433, Contract No. AF 30 (602)-3569, October 1968.

10. H. K. Detweiler, "Calculation of Space-Charge Forces in the Analysis of Traveling-Wave Tubes," JPL Quarterly-Technical Review, vol. 1, p. 106, April 1971.

11. H. G. Kosmahl, "A Novel, Axisymmetric, Electrostatic Collector for Linear Beam Microwave Tubes," NASA Technical Note D-6093, February 1971.

12. I. Tammaru, "Refocusing of the Spent Axisymmetric Beam in Coupled Cavity Traveling-Wave Tubes," NASA Final Report CR-120893, Contract No. NAS 3-11539, July 1971.

13. J. R. Molnar and C. R. Moster, "Some Calcuations of the Magnetic Field Requirements for Obtaining Brillouin Flow in Cylindrical Electron Beams," Bell Telephone Lab Report 51-2940-1, January 1951.

14. N. Stankiewicz, "Analysis of Spent Beam Refocusing to Achieve Optimum Collector Efficiency," IEEE Trans. on Electron Devices, vol. ED-24, p. 32, January 1977.

15. R. H. LeBorgne, L. E. Brown, J. A. Christensen and I. Tammaru, "A 120 Watt, 12 GHz Space Tube with 54% Efficiency," presented at the 1976 Power Tube Specialist Conference, Monterey, California, April 1976 (unpublished).